



Analysis of Sub-Synchronous Oscillations in Wind Power Plants

MUHAMMAD TAHA ALI

Doctoral Thesis in Electrical Engineering
Stockholm, Sweden 2020

KTH School of Electrical Engineering and Computer Science
TRITA-EECS-AVL-2020:19
ISBN 978-91-7873-485-6

SE-100 44 Stockholm
SWEDEN

Akademisk avhandling som med tillstånd av Kungl Tekniska högskolan framlägges
till offentlig granskning för avläggande av teknologie doktoresexamen i elektriska
energisystem den 14 May 2020 klockan 10.00 i sal Kollegiesalen, Brinellvägen 8,
Kungliga Tekniska högskolan, Stockholm.

© Muhammad Taha Ali, May 2020

Tryck: Universitetsservice US AB

Abstract

The modern power system is moving towards the high integration of renewable energy sources at a fast pace. The integration of wind power in the power system raises many challenges along with the benefits. One of the recent challenges is the sub-synchronous oscillation (SSO) that occurs in doubly-fed induction generator (DFIG) based wind farms. This oscillation is caused by sub-synchronous control interaction (SSCI). The SSCI condition occurs when the DFIG-based wind farm is radially connected to a series compensated transmission line. The aim of this thesis is to investigate and study the circumstances and causes of SSCI, and to develop the techniques that could mitigate this condition from the system. A mathematical model of DFIG-based power system is designed and an eigenvalue analysis is performed. The eigenvalue analysis shows that out of many factors, the level of series compensation play major role in inflicting SSCI in the system. The eigenvalue sensitivity analysis is performed on all the controller parameters of DFIG converters. It is shown that the proportional parameter of the rotor-side converter (RSC) is the most sensitive parameters and the stability of the system is highly dependent on its value. Moreover, the participation factors of the system are also computed to understand the phenomenon better. SSCI is also explained through the internal impedance of induction generator, as seen from the stator terminal. It is shown that the presence of RSC controller enables the occurrence of SSCI, by increasing the negative resistance of the rotor, and its proportional parameters adds up to the negative resistance.

Two mitigation techniques are presented in this thesis. In the first technique a power oscillation damper (POD) is designed and tuned. The proper placement of a tuned POD in the DFIG converter can eliminate the SSCI from the system using a local signal. In the second technique, the boomerang effect of the most sensitive control parameter is presented and it is proposed that the proper selection of control parameters can eliminate the risk of SSCI from the system, even for higher series compensation levels. Along with linearized and non-linear simulations, the sensitivity analysis and the mitigation of SSCI through proper selection of control parameters is validated experimentally using an actual 7.5 kW DFIG system. The analysis of SSCI is also carried out in a multi-machine two-area system and the mitigation techniques are successfully implemented. The influence of synchronous generator on SSCI is also studied, and the mitigation of SSCI using PSS in the synchronous generator is presented. It is shown that by implementing all the mitigation techniques simultaneously, the multi-machine systems can be made immune to SSCI for any realistic level of series compensation.

Sammanfattning

Det moderna kraftsystemet går i snabb takt mot en hög integration av förnybara energikällor. Integration av mer vindkraft i kraftsystemet skapar nya utmaningar vid sidan av fördelarna. En av de senaste utmaningarna är subsynkrona oscillationerna (SSO) som uppstår i en dubbeltmatad induktionsgenerator baserad (DFIG) vindkraftspark. Dessa oscillationer orsakas av subsynkron regulatorinteraktion (SSCI). SSCI-tillståndet inträffar när den DFIG-baserade vindkraftsparken är radiellt ansluten till en seriekompenserad transmissionsledning. Syftet med denna avhandling är att studera omständigheterna och orsakerna till SSCI samt att utveckla tekniker som kan mildra detta tillstånd. En matematisk modell av ett DFIG-baserat kraftsystem konstrueras och en egenvärdesanalys utförs. Egenvärdesanalysen visar att bland många faktorer spelar seriekompenstationen en viktig roll för att skapa SSCI i systemet. Känslighetsanalysen utförs på alla styrparametrar för DFIG-omvandlaren. Det visas att proportionalitetsparametern för rotorsidonomvandlaren (RSC) är den mest känsliga parametern och att systemets stabilitet är starkt beroende av dess värde. Dessutom beräknas systemets partitionsfaktorer för att förstå fenomenet bättre. SSCI förklaras också genom den interna impedansen hos induktionsgeneratorn sett från statorterminalen. Det visas att närvaren av styrsystemet för RSC möjliggör förekomsten av SSCI genom att öka rotorns negativa motstånd och dess proportionella parametrar adderas till det negativa motståndet.

Två metoder för att minska SSO presenteras i denna avhandling. Den första tekniken konstruerar och ställer in styrparametrar i en dämpatillsats (POD). En korrekt placering av en väl inställd POD i DFIG-omvandlare kan eliminera SSCI från systemet med lokal mätsignal. I den andra metoden presenteras bumerangeffekten av den mest känsliga regulatorparametern och det konstateras att korrekt val av regulatorparametrar kan eliminera risken för SSCI från systemet även för högre seriekompressionsnivåer. Tillsammans med linjäriserade och icke-linjära simuleringar valideras känslighetsanalysen och mildring av SSCI genom korrekt val av regulatorparametrar experimentellt med användning av ett verkligt 7,5 kW DFIG-system. Analysen av SSCI utförs också i ett system med flera maskiner och metoderna implementeras framgångsrikt. Påverkan av synkrongenerator på SSCI studeras också, och begränsningen av SSCI med PSS i synkrongenerator presenteras. Det visas att genom samtidigt implementering av dessa metoder är ett kraftsystem med flera maskiner immun mot SSCI för alla realistiska seriekompressionsnivåer.

Acknowledgements

This research work is carried out with the support of Energiforsk and SweGRIDS, the Swedish Center for Smart Grids and Energy Storage. I would like to wholeheartedly thank both the organizations for sponsoring and supporting our research work.

I want to put forward my profound and deepest gratitude towards my supervisor, Prof. Mehrdad Ghandhari, for his continuous guidance, motivation, and support. Thank you so much for always being there and for being a helping hand during my difficulties. I would like to thank my co-supervisor, Prof. Lennart Harnefors, for being my mentor, for his guidance and for extraordinary feedback. The presence of both my supervisors made the completion of this thesis possible. I would like to thank Prof. Lars Nordström for being a supportive and a wonderful head of the division. I would also like to thank Dr. Robert Eriksson for reviewing my thesis, and for providing me with the valuable feedback. How can I forget the continuous support from the KTH staff? Thank you Eleni, Brigit, Annica, Elvan, Viktor and Peter for always solving and addressing my issues.

Talking about the Aalborg University, the host institution during my research mobility, I would like to extend my gratitude to my supervisors there; Prof. Frede Blaabjerg, Dr. Dao Zhou, and Dr. Yipeng for their supervision and guidance, and for giving me an opportunity to benefit from the experimental facilities.

Thank you all my colleagues at KTH for shaping my last five years in a pleasant and an exquisite way. Thank you my officemates; Dimitris, Omar, and Angelica for keeping a fun environment in the office room. Thank you Marina and Danilo for your support during the courses and for bearing me as a course responsible. Thank you Ehsan for your help and assistance for my side project. Special thanks to Kaveh for guiding me towards a new path of self-improvement, it is wonderful

to have a friend who has the same life interests as yours. My sincere thanks to Stefan 'Stanko' for being my 'direction' towards every solution, and thank you Lars Herre for the nice conversations in gym (a place I used to go). Thank you Elis for always helping me with the Swedish translation, be it my thesis or a negotiation for furniture. I cordially thank you all for the wonderful moments that we cherished together.

Away from the motherland, one always need to have some moments in the day to converse in ones native language. Thank you my desi colleagues for being my reason to speak Urdu/Hindi. Thank you Khizra, Priyanka, Umbreen, Shubhangi, Imtisal, and Zakaria for the smiles and laughters that we shared. Almas, Farhan, and Afzal, accept my special thanks for being my advisers and for treating me like your younger brother. Almas, I couldn't forget those buffets, I wish to have more of those soon. My cordial thanks to you Asif Iqbal for always sharing your life lessons with me and for making me a better person. I would like to thank all my colleagues at EPE; Tin, Fabian, Evelin, Egill, Oscar, Giovanni, Abolfazl, Constantina, Ilka, Stefanie, Baris, Evan, Meng, Charlotta, Ilias, and everyone else for giving me beautiful moments of life to look back at and smile. Thank you Francisco for the Spanish jokes and for teaching me the dance steps. You will always be missed, brother.

Not forgetting my chilling-time buddies; Omar Safdar, Talal, Anna, Erfan, Arif, Zeeshan, Awais, Shoaib, and Fidai. Thank you all for the nights out, trips, and the entertainments that we had together. Thank you Yaqoob for being my support during the last year of my PhD. I would also want to show my gratitude to all my friends in Pakistan; Ahsan, Arslan, Owais, Jahanzaib, Ali Dad, Ali Anwar, Hamid, Sidra, Maryam and to my friends of NIC center, who were always there to support me in every possible way.

Last but, definitely, not the least, I would like to thank my family from the core of my heart, for their struggle, unconditional love, and endless prayers. Because of you I could become what I am today. Thank you Abbu, Ammi, Chachoo, Nano, Sari Phopo, Asghar bhai, and my siblings for your contribution towards my success and happiness. I wouldn't have reached here without all of you. I would also want to thank my wife Anam Ali, a new and a beautiful addition in my life, for her love and for her support during my strict deadlines. Thank you.

*To the One, Who is near despite of His exaltedness.
And, Who is exalted despite of His nearness.*

Contents

Contents	ii
List of Figures	4
List of Tables	7
1 Introduction	9
1.1 Background	9
1.2 Aims and Contribution of Project	12
2 Literature Review	15
2.1 Sub-Synchronous Oscillation	15
2.2 Sub-Synchronous Resonance (SSR)	16
2.2.1 Sub-Synchronous Torsional Interaction (SSTI)	17
2.2.2 Torque Amplification (TA)	18
2.2.3 Induction Generator Effect (IGE)	18
2.2.4 Sub-Synchronous Control Interaction (SSCI)	18
2.3 Types of Wind Turbines	20
2.3.1 Fixed-Speed Wind Turbine (Type-1)	20
2.3.2 Variable-Speed Wind Turbine (Type-2)	21
2.3.3 Doubly-Fed Induction Generator (Type-3)	22
2.3.4 Full-Converter Wind Turbine (Type-4)	23
2.4 Review of Previous Work	23
2.4.1 SSCI in Wind Turbines	24
2.4.2 Tools for Analysis of SSCI	25
2.4.3 Identification of Involved Parameters & Components . . .	27
2.4.4 Mitigation of SSCI	28

3 Modelling of a DFIG-based Power System	31
3.1 Modelling of DFIG	32
3.1.1 Drive Train Model	32
3.1.2 Induction Generator Model	33
3.1.3 Rotor-Side Converter (RSC) Controller Model	35
Decoupled dq axes current tracking	39
Conversion between reference frames	41
3.1.4 Grid-Side Converter (GSC) Controller Model	43
3.1.5 Converter Transformer Model	45
3.1.6 DC-Link Model	46
3.2 Modelling of External Network	47
3.2.1 Shunt Capacitor at DFIG Terminal	48
3.2.2 Transmission Network Model	50
3.3 Initialization and Finding Equilibrium Points	52
3.4 Observation of the SSCI	56
4 Eigenvalue Analysis & Infliction of SSCI in DFIG-based Power System	59
4.1 Eigenvalue Analysis of the DFIG-based Power System	59
Eigenvalues	60
4.1.1 Computed Eigenvalues of DFIG Test System	61
4.1.2 Effects of Different Compensation Levels	64
4.1.3 Effect of Different Rotor Speed and Generated Power	65
4.1.4 Sensitivity Analysis of Control Parameters	67
Type A Parameters	68
Type B Parameters	68
Type C Parameters	70
Type D Parameters	70
4.1.5 Participation Factor	73
4.2 Infliction of SSCI in DFIG-based Power System	75
4.2.1 Internal Equivalent Resistance of Generator	76
4.2.2 Effect of RSC on Internal Equivalent Resistance	80
4.2.3 Explanation of infliction of SSCI	88
5 Mitigation of SSCI in DFIG-based Power System	91
5.1 Mitigation through Control Parameters Tuning	91
5.1.1 The Boomerang Effect of K_{p3}	91
5.1.2 Results of Linearized DFIG System	93
Optimum Value of K_{p3}	95

5.1.3	Simulation of DFIG System	98
5.1.4	Experimental Validation of SSCI Analysis and Mitigation	103
Experimental Setup	103	
Experimental Results	107	
5.2	Mitigation through Supplementary Control Signal	111
5.2.1	Power Oscillation Damper (POD)	112
Residue	113	
Tuning of Phase Compensation Block	114	
Selection of POD Gain	117	
5.2.2	Analysis of POD	117
DFIG Active Power (P_{DFIG}) and Apparent Power (S_{DFIG}) as Input to POD	119	
Transmission Line Current (I) as Input to POD	123	
5.2.3	Simulation Results	124
Results of Linearized System	124	
Simulation of DFIG System	128	
5.3	Case Studies for the Mitigation Techniques	131
5.3.1	Simulation of the ERCOT incident	132
5.3.2	Analysis of SSCI in two-area system	133
Eigenvalues of System-2	134	
Participation Factors of System-2	135	
Eigenvalues Analysis of System-2	136	
5.3.3	Mitigation of SSCI in System-2	140
6	Conclusion and Future Work	145
6.1	Conclusion	145
6.2	Future Work	147
Bibliography		151

List of Acronyms

SSO	Sub-Synchronous Oscillation
DFIG	Doubly-Fed Induction Generator
SSCI	Sub-Synchronous Control Interaction
SSR	Sub-Synchronous Resonance
SSTI	Sub-Synchronous Torsional Interaction
IGE	Induction Generator Effect
TA	Torque Amplification
EMTP	Electro-Magnetic Transient Program
VSC	Voltage-Source Converter
RSC	Rotor-Side Converter
GSC	Grid-Side Converter
FACTS	Flexible Alternating Current Transmission Device
HVDC	High Voltage Direct Current
STATCOM	STATIC synchronous COMpensator
LQR	Linear Quadratic Regulator
MMF	Magnetic Motive Force
SMIB	Single Machine Infinite Bus
ERCOT	Electric Reliability Council Of Texas
SFO	Stator-Flux Oriented
TV	Terminal Voltage
PWM	Pulse Width Modulation
LTI	Linear Time Invariant
PI	Proportional-Integral
SUB	Sub-Synchronous
SUP	Super-Synchronous
POD	Power Oscillation Damper
PSS	Power System Stabilizer

List of Figures

2.1	Single line diagram of a simple radial system.	17
2.2	Measured phase voltage and line current for Ajo 311L at Zorillo [35].	20
2.3	Block diagram of fixed-speed wind turbine.	21
2.4	Block diagram of variable-speed wind turbine.	21
2.5	Block diagram of doubly-fed induction generator wind turbine.	22
2.6	Block diagram of full-converter wind turbine.	23
3.1	Block diagram of DFIG-based power system.	31
3.2	Visualization of TV reference frame.	36
3.3	Block diagram of RSC controller.	38
3.4	RSC controller with decoupling.	42
3.5	Block diagram of GSC controller.	44
3.6	Block diagram of DC-link between converters.	47
3.7	Single line diagram of external network.	48
3.8	Different reference frames.	48
3.9	Connection of shunt capacitor between DFIG and network.	49
3.10	Single line diagram of external network.	51
3.11	Response of system for increase in compensation to 40%.	57
3.12	Response of system for increase in compensation to 50%.	57
4.1	Eigenvalues of the system.	62
4.2	Eigenvalues of the system zoomed-in.	63
4.3	Effect of series compensation level.	64
4.4	Effect of series compensation level zoomed-in.	65
4.5	Effect of different rotor speed ω_r on SUB mode.	66
4.6	Effect of generated DFIG power on SUB mode.	67
4.7	Effect of integral parameters on SUB and SUP modes.	69

4.8	Effect of K_{p4} and K_{p5} on SUB and SUP modes.	69
4.9	Effect of K_{p6} on SUB and SUP modes.	70
4.10	Effect of K_{p1} and K_{p2} on SUB and SUP modes.	71
4.11	Effect of K_{p3} on SUB and SUP modes.	71
4.12	Range of parameters for different compensation levels.	72
4.13	Equivalent circuit of induction generator.	76
4.14	Equivalent resistance as seen from stator terminal.	78
4.15	Equivalent resistance for different R_s and R_r	78
4.16	Effect of R_s and R_r on SUB mode of DFIG system.	79
4.17	Equivalent circuit of generator with RSC.	80
4.18	Equivalent Γ model.	81
4.19	Inner current control loop of RSC.	82
4.20	RSC in equivalent circuit of induction generator.	83
4.21	Equivalent impedance of generator with RSC.	84
4.22	Equivalent impedance of generator with RSC using T-model.	85
4.23	Equivalent resistance of generator with RSC.	86
4.24	Influence of RSC on modes of interest.	87
5.1	Equivalent resistance of generator with different K_{p3}	93
5.2	Effect of higher K_{p3} on SUB and SUP modes.	94
5.3	Root-locus and open-loop Bode plot for change in K_{p3}	95
5.4	Range of sensitive parameters for different compensation.	96
5.5	Value of K_{p3} for highest damping.	97
5.6	Reference tracking of RSC controller for $K_{p3}=4$ p.u.	99
5.7	Simulation of DFIG system with different K_{p3}	100
5.8	The boomerang effect of K_{p3} on DFIG system.	101
5.9	Runtime effect of K_{p3} to mitigate SSCI.	102
5.10	Gain scheduling of K_{p3} after SSCI detection.	103
5.11	Flowchart of SSCI detection and gain scheduling.	104
5.12	Experimental setup of DFIG test system.	105
5.13	Power electronic converters and dc-link.	106
5.14	Resistors, inductors, and series compensation capacitors.	106
5.15	Experimental results displayed on oscilloscope.	107
5.16	SSCI in experimental setup of DFIG.	108
5.17	Undamped oscillations in experimental setup of DFIG.	109
5.18	Frequency of the undamped oscillations in dc-link voltage.	109
5.19	Aggravation of SSCI with wrong choice of RSC parameters.	110
5.20	Mitigation of SSCI from DFIG system.	110

5.21	Addition of POD in a system.	111
5.22	Block diagram of POD.	112
5.23	Closed-loop system.	114
5.24	Graphical representation of residue.	115
5.25	Different junctions of RSC controller.	118
5.26	Bode phase plot of tuned POD added in junction $Q_s - 1$.	120
5.27	Movement of eigenvalues with and without POD at $Q_s - 1$.	121
5.28	Root-Locus plot of system with POD at $Q_s - 1$ junction.	122
5.29	Root-locus plot of system with POD at $V_{dc} - 3$ and $u_{in} = P_{DFIG}$.	122
5.30	Root-locus plot of system with POD at $V_{dc} - 3$ and $u_{in} = I$.	124
5.31	3D plots for a system with and without POD at Q_{gsc} controller.	125
5.32	3D plots for a system with and without POD at V_{dc} controller.	126
5.33	Effect of POD at $V_{dc} - 3$ junction with $u_{in} = P_{DFIG}$.	127
5.34	Comparison of POD with different inputs at $V_{dc} - 3$.	127
5.35	Simulation of a P_{DFIG} at 70% compensation with POD in Q_{gsc} controller.	129
5.36	Simulation of a P_{DFIG} at 70% compensation with $u_{in} = P_{DFIG}$ in Q_{gsc} controller.	129
5.37	Simulation of a DFIG system at 65% series compensation.	130
5.38	Simulation of a DFIG system at different compensation levels.	131
5.39	Comparison of the performance of POD with tuned K_{p3} .	132
5.40	System similar to the system in ERCOT's incident.	132
5.41	Response of the DFIG with and without mitigation techniques.	133
5.42	Single-line diagram of two-area system.	134
5.43	Excitation system of synchronous generator.	134
5.44	Effect of compensation level on modes of System-2.	138
5.45	Effect of increase in K_{p3} on modes of System-2.	138
5.46	Effect of RSC and its blockage on modes of System-2.	139
5.47	Influence of SG-2 on modes of System-2.	139
5.48	Effect of mitigation techniques on System-2.	141
5.49	Simultaneous implementation of mitigation techniques in System-2.	142
5.50	Mitigation of SSCI in DFIG active power of System-2.	142
5.51	Loss of SG-2 and infliction of SSCI.	143

List of Tables

3.1	Quantities of Drive Train Model	33
3.2	Quantities of Induction Generator	35
3.3	Quantities of RSC Controller	42
3.4	Quantities of GSC Controller	45
3.5	Quantities of Converter Transformer Model	46
3.6	Quantities of DC-Link Model	47
3.7	Quantities of Shunt Capacitance Model	51
3.8	Quantities of Transmission Network Model	52
4.1	Eigenvalues of Modes of Interest	63
4.2	Classification of Control Parameters	68
4.3	Participation Factors of DFIG System	74
5.1	Eigenvalues of Modes of Interest at 65% Compensation Level	118
5.2	Residues of Modes of Interest at 65% Compensation Level	119
5.3	Residues of Modes of Interest at 65% Compensation Level	123
5.4	Eigenvalues of Modes of Interest of System-2	135
5.5	Participation Factors of System-2	135
6.1	Parameters of DFIG system	149
6.2	Parameters of the Controllers in p.u.	149
6.3	Parameters of DFIG System Used in POD Analysis	150
6.4	Parameters of the Controllers Used in POD Analysis in p.u.	150

Chapter 1

Introduction

1.1 Background

In modern electric power systems, the shift of classical power generation to renewable energy sources is growing with a fast pace. Due to environmental and economic concerns, the authorities dealing with electrical power generation are putting their main focus on increasing the integration of renewable energies, with a goal to make the electrical power generation 100% environmental friendly. A vital and prominent renewable energy source among the other sources is wind energy. Humans have been taking advantages of wind energy for ages. Before generating electrical power from wind energy, it had been used for sailing, grinding, and pumping [1]. Wind turbine generators convert the mechanical energy, extracted from the flowing air, into electrical energy.

These turbines do not produce greenhouse gas emission, are a cost effective domestic source, do not rely on fuel combustion, and use little land area. In recent years the generation and integration of wind power is witnessed to have increased rapidly, especially over the last two decades [2]. By 2020, the power generated by wind turbine generators is expected to exceed 760 GW [3]. This increase in wind power integration promises a more environmental friendly power system. However, along with this promise there are few inevitable issues which wind power brings with its integration. To name a few, problems like intermittent power generation, frequency stability issues because of low inertia, and long distance between generation and load areas are being faced by power system engineers [4], [5].

In many cases, the wind farms are situated in the areas far from the consumptions side, e.g., offshore wind farms, because of that the transfer of bulk power from generation side to load areas becomes challenging. This challenge arises because the increasing inductance of transmission line with the increase in its length limits its capacity of power transmission. The limitation of transmission line is catered by the use of series compensation capacitors, which increase the power factor by reducing the equivalent reactance. As a result, the capacity of transmission lines increases [6]. Although the series compensation technique makes it efficient to transfer power over longer distance, but it also exposes the power system to the risk of sub-synchronous oscillation (SSO) [7].

SSO is an oscillation that arises in power system as a result of exchange of energy between two or more of its components. These oscillations are in a frequency range, which is below the synchronous frequency of the system. It is seen in certain electrical networks, and studied in literature, that when a wind farm is connected radially to a series compensated transmission line then there comes a risk of the occurrence of SSO [8]. The phenomena that inflict the SSO are categorized into different types. Until 2009, it was considered that only first two types of the wind turbines, i.e., fixed speed wind turbine (Type-1) and variable speed wind turbine (Type-2), were vulnerable to SSO. This is because both the types do not contain any power electronic converter that either fully or partly isolate the wind turbine from the electrical grid. It was also considered that the other two types of wind turbines, i.e., doubly-fed induction generator (DFIG) (Type-3) and full-converter wind turbine (Type-4), were immune to SSO because of having power electronics converters in their structure [9].

However, in 2009 an incident occurred in the electrical network of Electric Reliability Council of Texas (ERCOT). There occurred a fault in the transmission system of ERCOT. In order to clear the fault, a line was tripped by a circuit breaker, forming a new topology of the network. This new topology radially connected the two wind farms of ERCOT with a series compensated transmission line, thereby changing the effective series compensation level from 50% to around 75%. As a result of the radial connection, voltage and current oscillations commenced, which grew rapidly, damaging the wind farms [10]. Contrary to the belief prevalent before this incident, the SSOs occurred in the wind farms containing DFIG wind turbines. This incident raised an alarming situation among electrical engineers and researcher to probe and ponder upon the causes of such oscillations. The events of similar nature are reported to have occurred in other electrical networks in south-

western Minnesota and in Hebei, China [11].

The repeated occurrence of this type of oscillation in DFIG wind turbines, radially connected to series compensation transmission lines, makes it significant to investigate and study its causes. Considering the structure of DFIG wind turbine, although there is the presence of a power electronics back-to-back converter, but this converter does not fully isolate the generator from electrical network. In DFIG, the rotor windings of induction generator (IG) are connected to the transmission grid via a back-to-back converter, while the stator winding are connected directly to the grid. This partial isolation of generator from grid eliminates the risk of energy exchanges between mechanical part of generator and the electrical grid. However, there still exists a risk of interaction between the generator and the external network because of the partial connection [12].

Intensive research has been and is being done to understand the reasons of this recent SSO. One finding is that these oscillations occur when there is an exchange of energy between the power electronic converter controllers and the series compensation capacitor. The phenomenon is named as sub-synchronous control interaction (SSCI), as this an interaction between the control system of converters and the series capacitor. The frequency of the inflicted oscillations, as a result of SSCI, is well below synchronous frequency and that is why these oscillations are considered as a type of SSO [8], [9], [12].

DFIG is considered to be an important type of wind turbine generator, among all other types, because of a capability of generating variable power, and having a back-to-back converter as a part of its structure, which deal with a certain percentage (normally 30%) of its rated power. This low rating of power electronics devices in DFIG makes it less costly than type-4 wind turbine generator, and also the switching losses in DFIG are lower. As far as the series compensation of transmission lines is concerned, this technique is used widely for its effectiveness of enhancing the power transfer capability of transmission lines, by improving the power factor. It has been used for the optimization of transmission corridors for the long distances and is considered to be the cost effective solution [13].

Taking in to account the significance of the two key parts of the power system, i.e. DFIG and series compensation capacitor, which trigger the condition of SSCI in an electrical network, it can be said that avoiding the use of any of the two players would not be an appropriate solution. Therefore, there is a dire need for

analyzing and investigating the reasons for the occurrence of SSCI and to design a solution which can complement the existence of both the components by mitigating SSCI in the DFIG-based power system.

1.2 Aims and Contribution of Project

Aims

As the title says, this thesis analyzes the SSO in wind power plants. Although there are many phenomena which cause SSO, as presented in Chapter 2 of this thesis, after thorough literature review, it is found that phenomena like sub-synchronous torsional interaction (SSTI) and torque amplification (TA) are under consideration of researchers since three decades and a lot of work has been done on its investigation and solutions. However, the phenomenon of SSCI is the most recent one and first came into existence in 2009. The literature review shows that there is still a need to understand this phenomenon better and more investigation must be carried out. Further, it is found in literature that the only type of wind turbine which is vulnerable to SSCI is the DFIG wind turbine. DFIG, being one of the widely used types of wind turbines, needs to have a smooth operation and integration into the power system in order to ensure the reliability of wind energy. Considering the importance and the wide application of DFIGs, it is of dire need that the recent mishaps of SSCI in DFIG-based wind farms should essentially be considered, understood, solved, and avoided in future.

The objective of this thesis is to study and understand the phenomenon of SSCI in DFIG wind turbines, to identify the causes of its occurrence, and to observe the effect of the control parameters of DFIG's converters on the infliction of SSCI. The thesis also examines the influence of the rotor speed, the magnitude of the generated power, and the level of series compensation on the stability of the system, having the DFIG in radial connection with series compensated transmission line. For this purpose, the eigenvalue analysis tool is selected. Although this tool requires a detailed mathematical model of the whole system but it gives valuable information that is very helpful in investigating SSCI.

The thesis also aims to develop a control strategy which can mitigate SSCI in cost effective and in efficient manners. The work done in this project uses mathematical techniques to design and tune the controller and to determine the placement

of controller for best operation. This thesis also intends to test the robustness of the proposed solution, to SSCI problem, under different circumstances and over different realistic levels of series compensation in single-machine infinite bus (SMIB) as well as multi-machine system.

Contributions

The main contributions of this thesis can be summarized as follows:

1. The infliction of SSCI and the actual role of rotor-side converter (RSC) controller towards SSCI are explained by connecting the dots obtained from analytical expressions and eigenvalue analysis. The difference between SSCI and induction generator effect (IGE) is also described by showing that SSCI is basically an aggravated IGE, because of the presence of RSC controllers.
2. The most sensitive control parameter of RSC controller is identified and its boomerang effect is explained mathematically and analytically. It is shown that by tuning the control parameters properly while considering this effect, the DFIG system can be made immune to SSCI even for higher compensation levels, without using any additional control strategy.
3. The results obtained from the analysis and mitigation of SSCI in point 2 are validated experimentally through a 7.5 kW scaled-down DFIG system.
4. A supplementary controller is tuned and placed optimally using only the local input signals. Therefore the need to estimate remote signal is excluded, and it also reduces the risk of the input signal being erroneous.
5. The presented mitigation techniques are tested on different systems topologies, including the two-area system. For the DFIG-based system with a synchronous generator (SG), it is shown that the SG also participates in the infliction of SSCI. And, consequently, adding the supplementary control in SG can also mitigate SSCI from the system.

List of articles

Journal paper

- **J1** M. T. Ali, D.Zhou, Y. Song, M. Ghandhari, L. Harnefors, and F. Blaabjerg, "Analysis and Mitigation of SSCI in DFIG Systems With Experimental

Validation," Accepted for publication in *IEEE Transactions on Energy Conversion*. Dao Zhou and Yipeng Song assisted in experimental procedure. Muhammad Taha Ali carried out the research work and wrote the paper under the supervision of Mehrdad Ghandhari, Lennart Harnefors, and Frede Blaabjerg.

Journal paper submitted

- **J2** M. T. Ali, S. Stankovic, M. Ghandhari and L. Harnefors, "Analysis and Mitigation of Sub-Synchronous Control Interaction in DFIG-based Multi-Machine System," *Submitted to CIGRE Journal*. Stefan Stankovic assisted in the modelling of the system. Muhammad Taha Ali carried out the research work and wrote the paper under the supervision of Mehrdad Ghandhari and Lennart Harnefors.

Peer-reviewed conference papers

- **C1** M. T. Ali, M. Ghandhari, and L. Harnefors, "Effect of control parameters on infliction of sub-synchronous control interaction in DFIGs," *2016 IEEE International Conference on Power and Renewable Energy (ICPRE)*, Shanghai, 2016, pp. 72–78. Muhammad Taha Ali carried out the research work and wrote the paper under the supervision of Mehrdad Ghandhari and Lennart Harnefors.
- **C2** M. T. Ali, M. Ghandhari, and L. Harnefors, "Mitigation of sub-synchronous control interaction in DFIGs using a power oscillation damper," *2017 IEEE Manchester PowerTech*, Manchester, United Kingdom, 2017, pp. 1–6. Muhammad Taha Ali carried out the research work and wrote the paper under the supervision of Mehrdad Ghandhari and Lennart Harnefors.
- **C3** M. T. Ali, M. Ghandhari and L. Hatnefors, "Optimal Tuning and Placement of POD for SSCI Mitigation in DFIG-based Power System," *2019 IEEE Milan PowerTech*, Milan, Italy, 2019, pp. 1–6. Muhammad Taha Ali carried out the research work and wrote the paper under the supervision of Mehrdad Ghandhari and Lennart Harnefors.

Chapter 2

Literature Review

This chapter deals with the theoretical aspects of the project based on the literature review. The brief explanation of SSO is given and different types of phenomena which lead to SSO in the power system are mentioned. The differences between these phenomena and the reasons for their infliction are also described. Moreover, all the four types of wind turbines are discussed in this chapter. A glimpse from the existing research related to the analysis and mitigation of SSCI is presented here, along with description of the tools and techniques used for the analysis.

2.1 Sub-Synchronous Oscillation

As the name suggests, sub-synchronous oscillation (SSO) is the oscillation, experienced by a power system, of frequency below the synchronous frequency. SSO basically occurs as a result of exchange of energy between two or more parts of the power system, at one or more of the system frequencies [14]. A power system is made up of many electrical and mechanical components. The electrical components can further be seen as the series or parallel combination of resistive, capacitive, or inductive elements with each combination having a particular natural frequency. The interaction between parts of the system, because of which the energy is exchanged, happens when the two parts fall into the resonant condition with each other at a specific frequency of sub-synchronous range. The exchange of energy during the resonant condition is called sub-synchronous resonance (SSR). SSR is further classified into different types depending upon the nature of interaction. The different types of SSR which inflict SSO in the electrical system are discussed in this chapter.

2.2 Sub-Synchronous Resonance (SSR)

According to the formal definition of sub-synchronous resonance (SSR), *it is a condition in electric power system when electrical network exchanges energy with turbine generator at one or more of the natural frequencies of combined system below the synchronous frequency of system [15]*.

In SSR, the electrical and mechanical parts of the turbine generator get into a resonant condition with the series compensation capacitor. Hence, SSR includes both mechanical and electrical parts of the power system. During SSR, the shaft of the turbine generator matches its mechanical resonance with the electrical resonance of series capacitor when there is a radial or nearly radial connection between the both. The electrical resonant frequency (f_e) of a simple radial system, as shown in fig. 2.1, can be calculated as [15],

$$f_e = f_r \sqrt{\frac{X_c}{X_g + X_L + X_t}} \quad (2.1)$$

where f_r is the average rotor frequency, whereas X_g , X_t , X_L , and X_c are the reactances of the generator, transformer, transmission line, and series capacitor, respectively.

The presence of resonant current of frequency f_e produces the torque and current of frequency f_{rr} in rotor winding, and this frequency can be calculated as,

$$f_{rr} = f_r \pm f_e. \quad (2.2)$$

The frequency $f_{rr} = f_r - f_e$ is called sub-synchronous frequency and the frequency $f_{rr} = f_r + f_e$ is called super-synchronous frequency. For the rotor, the network current seems to have two components, one of sub-synchronous frequency and the other one of super-synchronous frequency. The stability of the system is usually not threatened by the current components of super-synchronous frequency as such currents normally have high damping, however, the current components of sub-synchronous frequency sometimes pose threat to the stability of the system.

In literature, the first incident of SSR is reported to have occurred in 1970 in Mohave project in Nevada [17]. A 750 MVA cross-compound turbine generator was radially connected to a series compensated transmission line after a fault was cleared. As a consequence of this radial connection, the shaft of the generating unit experienced damages. After analyzing the problem, it was found that the damages

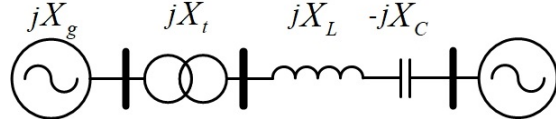


Figure 2.1: Single line diagram of a simple radial system.

occurred because of the exchange of an energy between the mechanical part of the generator and the series compensation capacitor.

According to [16], there are three types of SSR which are sub-synchronous torsional interaction (SSTI), induction generator effect (IGE), and torque amplification (TA). However, by the time the research work [16] was published, the phenomenon of SSCI had not yet occurred. Yet, the nature of SSCI shows that it can be considered as another type of SSR. Different types of SSR are described in the sequel.

2.2.1 Sub-Synchronous Torsional Interaction (SSTI)

The infliction of SSTI involves mechanical as well as electrical parts of a power system. The interaction inflicts when sub-synchronous torque pulsations occur at a frequency which is close to one of the natural frequencies of the shaft of the generator. During such condition, torsional oscillations in the rotor appear, resulting in the induction of voltage component in stator windings, having both sub-synchronous and super-synchronous components. This results in a feedback, which in cases of low inherent damping may result in instability and growing oscillations. SSTI usually occurs in the generator units where the inertia of the turbine and the generator is of same order. In the generation units where the inertia of generator is higher than the inertia of turbine, such as hydro generator unit, SSTI does not jeopardize the system because the speed variations are encountered on hydro turbine while the generator's speed remains unaffected [18].

The occurrence of SSTI can also be experienced in systems where the turbine generators are connected to power electronic converters. An example of such case is converter stations of HVDC. Typically exhibiting negative resistance in a sub-synchronous frequency range while operating as a rectifier [19], the HVDC converter station becomes vulnerable to SSTI. When this range matches any existing resonant frequency of the system, detrimental interaction may occur [35].

2.2.2 Torque Amplification (TA)

A system is vulnerable to TA when the resonant frequency of the electrical part is close to one or more torsional frequencies of the turbine shaft. During such condition there can be peak torques with large magnitude [7]. If there is any disturbance in the system during the resonant condition, then a torque pulsation is enforced on the rotor of the generator. After the disturbance, a high level current having frequency equals to natural frequency of the system, flows in the network. This current charges the series compensation capacitor, which is then discharged to the generator. This enforces the torque on rotor that oscillates at a sub-synchronous frequency. If this frequency is close to the natural frequency of any section of the mechanical system then undamped oscillations build up. The oscillations because of TA can damage the mechanical system in short time [20].

2.2.3 Induction Generator Effect (IGE)

IGE can simply be described as the self excitation of electrical system, which is series capacitor compensated, while assuming that the speed of the rotor is constant [16]. IGE is a purely electrical phenomenon and does not involve any mechanical part. The frequency of its occurrence is very close to the synchronous frequency of the system. The electrical systems having high level of series compensation are more susceptible to IGE. IGE comes into existence when the magneto-motive force (MMF), created by the sub-synchronous current in the stator winding, rotates slower than the MMF of the generator. This slow rotation of the produced MMF make the generator to operate like an asynchronous generator. This result in exhibiting the negative resistance of rotor, to sub-synchronous current, as seen from the generator's terminal [20]. If the negative resistance of rotor exceeds the total resistance of stator and network, then the overall system shows negative resistance to the sub-synchronous current and self-excitation of the system occurs. This self excitation yields in undamped oscillations in sub-synchronous current and consequently destabilizes the system.

2.2.4 Sub-Synchronous Control Interaction (SSCI)

SSCI involves an interaction because of a power electronics device and a series compensation capacitor. Like IGE, SSCI also does not include the mechanical part of system and only occurs because of the interaction in electrical parts. As compared to the type of SSR which involves mechanical parts, SSCI is found to grow faster because of being a purely electrical phenomenon. Research shows that

SSCI is basically an interaction between a voltage-source converter (VSC) and a series compensated transmission line [8]. The controllers of the power electronics converters play a crucial role in inflicting SSCI, hence, this interaction is referred to as *control* interaction. The rapid building of oscillation because of SSCI can also be justified with the fast nature of power electronic converters. The phenomenon of SSCI does not have any fixed frequency of occurrence. This is because the frequency of SSCI relies on the control parameters of VSC and the configuration of electrical network.

The reason why SSCI is not recognized in [16] is because the very first event of SSCI occurred recently in 2009. On 10th of October, 2009, an incident occurred in Zorillo Gulf Wind farm, operating under Electric Reliability Council of Texas (ERCOT). The measurements of phase voltage and line current at Zorillo is shown in fig. 2.2, [35].

The incident was recognized as a SSR event. There was single-phase to ground fault in one of the transmission lines of the system. While clearing the fault, the operation of the circuit breaker led to a radial connection between the DFIG-based wind farms and the series compensated transmission line. With this new topology, the system experienced oscillations of sub-synchronous frequency in the voltage. The oscillation grew so fast that the system voltage reached up to 195% of its rated voltage in a short time. These oscillation damaged the converters of DFIGs and the sub-synchronous currents were indicated by the series capacitor controls [35]. After the incident in Texas, some incidents of similar nature are reported to have occurred in south western Minnesota, and in some parts of China including Hebei [21], [22].

SSCI, being a purely electrical and a non-torsional phenomenon, is usually confused with IGE. The main difference between both these phenomena is the involvement of RSC controller. It will be shown analytically in Section 4.2 that the RSC controllers play a role in increasing the negative resistance of the generator, and aggravate IGE to SSCI. This means that if the controllers of RSC are blocked in DFIG then SSCI will not occur. However, still there would be a risk of IGE if the equivalent resistance of the system is negative at the frequency where equivalent reactance approaches zero [23]– [25].

Because of being a recent and repeatedly occurring phenomenon, analysis of SSCI is the main objective of this thesis. Further explanation of how SSCI builds up in DFIG is given in Section 4.2.3 after understanding the SSCI phenomenon through eigenvalue analysis and analytical expressions.

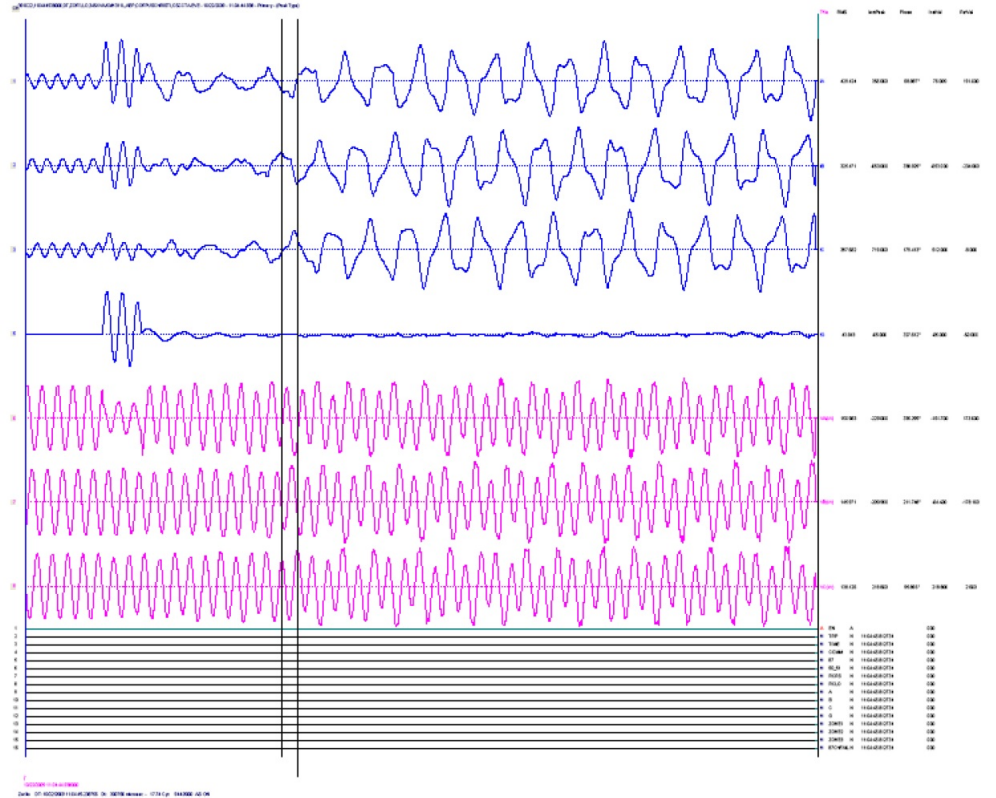


Figure 2.2: Measured phase voltage and line current for Ajo 311L at Zorillo [35].

2.3 Types of Wind Turbines

Wind turbines can have fixed rotor speed or variable rotor speed. Based on the structure, components, and operation, the wind turbines are classified into 4 types.

2.3.1 Fixed-Speed Wind Turbine (Type-1)

As the name suggests, the fixed-speed wind turbine operates for a fixed speed of rotor. It is also known as type-1 wind turbine. The unit is designed such that it can operate optimally for one rotor speed and the rotor speed is determined by the frequency of the grid, the gear box ratio and the number of generator pole-pairs. In type-1 turbine generator, the generator is connected to the grid directly to the AC grid, through a transformer, with the help of capacitor bank and soft starter,

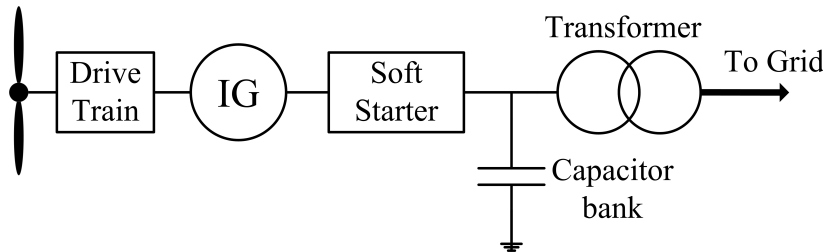


Figure 2.3: Block diagram of fixed-speed wind turbine.

as shown in fig. 2.3. The capacitor bank supports the reactive power consumption of the generator and the soft starter prevents the rush-in of a high network current in to the stator windings. The generator of type-1 turbine can be wound-rotor or squirrel cage induction generator. Type-1 wind turbines offer many benefit to the user in terms of cost, simplicity, and robustness but there are certain unfavourable characteristics which come along this type of wind turbine generator [26]. Because of being directly connected to the grid, the type-1 turbines cause power fluctuations as a result of variations in wind speed. The reactive power consumption of Type-1 turbine is not controllable.

Considering the occurrence of SSR in Type-1 wind turbines, it is reported in literature that the Type-1 wind turbines are exposed to SSR phenomena like IGE, and in certain conditions SSTI, because of being directly connected to the external network [27], [28].

2.3.2 Variable-Speed Wind Turbine (Type-2)

This type of wind generator uses wound-rotor induction generator and offers a limited range of variable speed. It is preferred to have output power of wind turbine

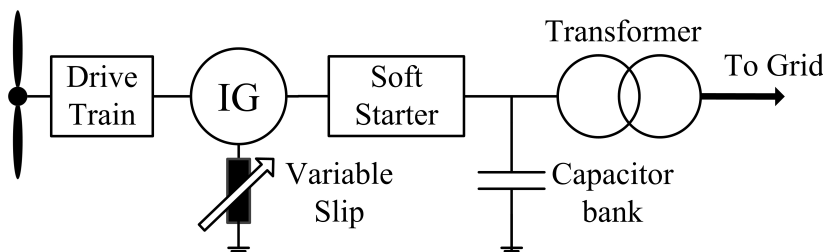


Figure 2.4: Block diagram of variable-speed wind turbine.

equal to the rated power, therefore the variable-speed wind turbines are considered to be important. Similar to Type-1 wind turbine, this wind turbine is also connected directly to the AC grid through transformer. The variable speed is achieved by the variable rotor resistors, as shown in fig. 2.4. The speed can be varied from 0% to 10% above the synchronous speed [26]. Having a similar topology as Type-1 wind turbines, the Type-2 turbines also pose risk for IGE and SSTI.

2.3.3 Doubly-Fed Induction Generator (Type-3)

DFIG operates at variable speed and it uses wound-rotor induction generator. The stator windings of the DFIG are connected to the external network directly and the rotor winding are connected to the external network through a back-to-back power electronics converter. The block diagram of DFIG is shown in fig. 2.5. The connection of the rotor with the converter is via slip rings. The presence of the converter in DFIG allows the variable speed operation of 30% speed above or below the synchronous speed, i.e., 70% to 130% of synchronous speed. The main advantages of DFIG are the comparatively high range of variable-speed, and the low rating of power electronics converter. As the converter has to deal with only 1/3 of the total power for variable speed operation, therefore the converter of lower rating is used which means that the cost and the power losses are lower as compared to fully rated converters. Another advantage of DFIG is the controllability of exchange of reactive power with the external grid.

It will be discussed in Section 2.4.1 that certain research works show that the DFIGs are not threatened by SSR phenomena that include mechanical part of the system, like SSTI or TA. However, DFIGs are susceptible to SSCI because of hav-

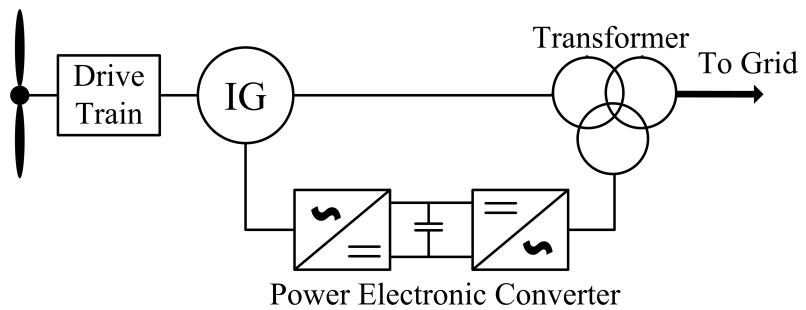


Figure 2.5: Block diagram of doubly-fed induction generator wind turbine.

ing a power electronics converter between their rotor windings and the AC network. It is shown in [29] that DFIG are also vulnerable to IGE because IGE is also a non-torsional type of SSR.

DFIG is the only type of wind turbine which experiences SSCI, therefore, the main focus of this thesis is to analyze and mitigate the occurrence of SSCI in DFIGs.

2.3.4 Full-Converter Wind Turbine (Type-4)

The Type-4 wind turbine is equipped with a back-to-back converter between the generator and the AC network, as shown in fig. 2.6. It could either use synchronous generator or cage-bar induction generator. The presence of back-to-back converter isolates the generator from the external network, hence, any disturbance that occurs in the grid can not propagate to the generator side. The converter also provides the control of active and reactive power [30]. For decoupling the generator side from the grid side, Type-4 wind turbines are known to be immune to SSCI problems, which includes the interaction with the series compensation capacitor [35]. However, as it will be mentioned in Section 2.4.1, the research shows that Type-4 turbines are vulnerable to other oscillations that occur because of the weak grid conditions and delays in the voltage measurement. Therefore, the analysis of such oscillations are out of scope of this thesis. The cons of Type-4 wind turbines are in terms of cost and losses. As the converter of Type-4 turbine has to deal with total rated power, its implementation gets expensive, and also because of the high power dealing, the power losses of the converter are high.

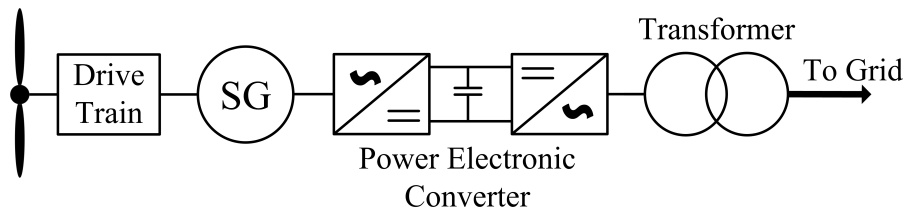


Figure 2.6: Block diagram of full-converter wind turbine.

2.4 Review of Previous Work

Being one of the recent problems that came across in wind power plants, SSCI is the focus of many researchers. The need to answer the unanswered questions

behind the infliction of SSCI has led to many important findings and conclusions. In this thesis the review of the concerned topic in previous research works is divided in to the following parts.

2.4.1 SSCI in Wind Turbines

Research shows that among all the types of wind turbine generators, DFIG is the only type which is vulnerable to SSCI because of having back-to-back power electronics converter connected between its rotor windings and the network. The research work done in [8] shows the reasons why DFIG wind turbines are vulnerable to SSCI. It comprehends that the phenomena such as TA and SSTI occur on fixed mechanical modes in turbine generator, as described before. On the other hand, SSCI has no fixed frequency of occurrence because the frequency of concern is dependent on control and electrical system parameters, and configuration. A system model was simulated in PSCAD/EMTDC and 5 steps mechanism of infliction of SSCI has been mentioned. The research work in [8] focused on the impact of control loops and it was found that rotor side current feedback loop has significant impact on SSCI. Type-4 turbines isolates the generator from the external network, so there is no infliction SSCI in them. Design of SSCI damping controller is given, and few other mitigation techniques are proposed, along with recommendations, but this research work does not show any mathematical manipulation of SSCI.

The research carried out in [9] explores the possibility of SSCI occurrence in Type-4 wind turbines. Frequency domain analysis, and PSCAD simulation was carried out and the results showed that Type-4 turbines are not vulnerable to SSCI. In [12], the occurrence of SSCI is simulated when wind farm containing Type-3 wind turbines is connected with series compensated transmission lines. This paper uses the IEEE second benchmark model for performing analytical studies. Frequency scan as well as time domain simulation methods have been used to investigate the occurrence of SSCI in Type-3 and Type-4 wind turbine generators. The benchmark model was tested for different configurations of the network, and different level of series compensation of the transmission lines.

It was observed that Type-4 wind turbines are not susceptible to SSCI even under direct radial connection of wind turbine with series compensated line, having 80% compensation. Research shows that a system with Type-3 wind turbine exhibits SSCI. Although the Type-4 wind turbine has a converter but this converter totally isolates the generator from the external network, hence, blocking any distur-

bance of resonant condition to enter into the generators side from external network. However, in DFIG the converter does not isolate the generator from the external network, totally. The other two types of wind turbines, i.e., fixed speed and variable speed wind turbines, cannot be counted in the list of generators which are vulnerable to SSCI, as both of these types do not possess any power electronic devices in their structure [12].

In [31], an interesting work is presented which shows that the type-4 wind turbines may also experience SSO. However, this SSO is not because of the radial connection with series compensated line, but because of the delay link of feed forward voltage measurement. It is shown in the paper that with the increase in this delay, the risk and intensity of the SSO increases significantly.

Other recently published papers present the analysis of SSO occurred in type-4 wind turbines. Such SSO was first observed in July 2015, in wind farms in Xinjiang, China. The research shows that main reason for the occurrence of SSO in type-4 wind turbine is the weak grid conditions, and the oscillations are observed in the system when the strength of the grid is reduced. The influence of other factors like electrical distance of the wind farm from the grid, the wind speed, and control parameters of GSC is also studied [32]. In [33], the same phenomenon is studied and the propagation of SSO in HVDC external wind power system is analytically explained. However, since the SSOs that occur in type-4 wind turbines do not include an interaction with series compensation capacitor, therefore, the study of such phenomenon is out of scope of this thesis.

2.4.2 Tools for Analysis of SSCI

In order to analyze the concerned control interaction, four main analytical techniques are used and reported in the literature.

Frequency Scanning

The first one is the frequency scanning technique. This technique is widely used to analyze SSCI by computing the equivalent reactance and resistance, as seen from the stator windings in to the network, and from the network in to the stator windings [7]. In [34], a general method for analysis of SSCI is given using frequency scanning method. The results obtained by this method are then validated by EMT programs. This research work gives a detailed description of the frequency scan-

ning method, and has used voltage signal for injecting harmonics in the system. The plus point of the research in [34] is its broad application which also includes frequency scanning for wind turbines with an active and non linear behaviour.

In [35], the frequency scanning method is implemented in PSCAD to analyze SSCI. The research is carried out to see the impact of system parameters on the equivalent resistance and reactance, over a range of frequency. It is shown that the current controllers have a significant impact on triggering the resonant condition for the interaction. The frequency scanning method is also used for analysis of control interaction in [36] to determine the presence of sub-synchronous resonant frequencies.

EMT Program

The electro-magnetic transient program (EMTP) is also used widely as a tool for the analysis of SSO. EMTP uses full three-phase of the system with detail models of all the components [7]. The analysis through EMTP is basically performed by computer simulation programs such as PSCAD/EMTDC. Due to the intricacy of mathematical equations of system during modelling, this method is preferred to observe and analyze different systems conditions that might lead to oscillations and resonance [35]. To name a few, electromagnetic transient analysis approach to investigate the occurrence of SSO in wind power plants has been used in [8], [9], [12], [34], [35], [41], and [42].

Eigenvalue Analysis

Eigenvalue analysis, being another analytical tool, has also been used to investigate SSO. This analysis provides valuable information about the performance of the system and is capable of providing the frequencies of oscillation and the damping at each frequency [7]. In order to perform the eigenvalue analysis, a detailed mathematical model of the whole system is required, which is also counted as a limitation for this technique. It is also used to determine the sensitivity of different modes of the system for different systems parameters. Eigenvalue analysis is used in many research work to understand the SSO. In [37] and [38], the eigenvalue analysis is used to study SSO in DFIG-based wind farm connected to series compensated line. The work studied the effect of series compensation level and wind speed on SSO, and it also addressed the impact of control parameters of current controller of converter on SSO conditions.

In [39], eigenvalue analysis is applied on a modified IEEE first benchmark model, with 100 MW DFIG-based wind farm, to study the control interaction. It explains the impact of wind speed and the variation of the compensation level on the control interaction. The research work in [40] uses the same analytical tool to study the behaviour of a grid connected DFIG. A detailed mathematical model of the whole system is established and eigenvalue analysis is applied on DFIG-based wind farm to study the modes of the system, which deteriorate the stability, in [41]. There are a number of other research papers that have used eigenvalue analysis investigating SSCI and for studying the respective proposed mitigation techniques [43]– [49].

Impedance-based Method

The impedance-based small signal analysis had been used previously for the analysis of power electronic converter, but the work in [50] proposes to use this technique for the analysis of SSCI. In impedance-based method, the impedance model of the whole DFIG system is derived. The system is represented as an equivalent voltage source in series with source impedance and connected to the load impedance. Based on this method, the effect on the internal impedance of the generator is observed to study the phenomenon of the interaction. In [50], the Nyquist stability criterion is used to analyze the stability of the system for different wind speeds. An equivalent second-order series *RLC* circuit is derived in [57] for the investigation of SSCI. The work presented in [52] also uses the impedance-based method and shows the analysis of the oscillation for different rotating speed, series compensation level, and control parameters, using Bode and Nyquist plots. Moreover, impedance-based method is also used in [53] and [54] as a tool to understand SSCI.

2.4.3 Identification of Involved Parameters & Components

The investigation and study of SSO in DFIG-based wind farms are also followed by the identification of sensitive control parameters of DFIG converters in some research papers.

In [47] the tool of eigenvalue analysis is used to identify the main parameters which contribute in causing the control interaction. This paper concludes that as the proportional parameters of inner current control loop in RSC are increased, the system gets more vulnerable to fall for the interaction. Similar results are found in [38], however, it is concluded that only the current controller of the torque con-

trol loop has the sensitive proportional parameter. In both [38] and [47] the impact of GSC control parameters are studied and it is observed that these parameters do not have any negative impact on sub-synchronous modes.

The movement of eigenvalues is studied in [55] to identify the control parameters which destabilize the sub-synchronous modes of the system. This research work also concludes that when both the proportional and integral parameters of rotor current controller are increased then the eigenvalues corresponding to sub-synchronous frequency tend to move towards right half plane, hence, making the system unstable. In [56] and [57], it is concluded that the proportional parameters of current controllers of the DFIG converters have significant influence on the sub-synchronous modes of DFIG system as compared to the integral parameters.

The research papers have also used eigenvalue analysis to compute the participation factors. With the help of the participation factors, the states of the system which play role in jeopardizing the sub-synchronous mode are identified [38], [41], [47], [58], [59]. It is found that the states which have high participation factors, corresponding to the sub-synchronous mode, are the states which represent the dynamics of induction generator, which in this case are d and q components of rotor and stator currents. However, the involvement of series compensation capacitor is not comprehended from the participation factors. Other factors like series compensation level and wind speed also play a role in the occurrence of SSCI in the system [41], [50], [52].

2.4.4 Mitigation of SSCI

Along with the investigation of SSCI, the solutions for its mitigation are also reported in the literature. In [55] a multi-input multi-output state-space methodology is used to design a damping controller. Two different approaches are added in grid-side and rotor-side converter controllers and are compared. It is found that the controller added in RSC is more effective as compared to the one in GSC because the former one has the capability to modify the effective resistance of rotor which impacts the damping of the oscillations directly.

The work in [60] uses flexible AC transmission system (FACTS) devices to damp the oscillations caused by SSCI. A damping control algorithm is designed for the mitigation of oscillations by using static synchronous compensator (STATCOM) and static synchronous series compensator (SSSC). The research shows that

SSOs can be mitigated by using the FACTS device. A SSCI-triggered damping control strategy is proposed in [61]. The proposed control strategy contains SSCI frequency acquisition, SSCI judgement, damping control, and dq decoupling control as the parts of RSC control system. The idea for this work is to use the damping control only in the conditions when SSCI is highly likely to be triggered in order to reduce the impact of damping controller in the normal operation of DFIG.

The ability of oscillation damping of converters of DFIG is investigated in [41] and [61] and an auxiliary damping controller is designed which feed in the control signal into converter controller. Different signals, as the input to the auxiliary controller, are tested. In [41], additional effort is done to find the optimal placement of the auxiliary control signal with in the controller of both RSC and GSC. Both the research works conclude that the auxiliary controller works best when it is added into GSC, and when the voltage across series capacitor, which is a remote signal, is used as the input to auxiliary controller. However, the controller does not perform well when the local signals are used as the inputs to it.

Moreover, there are a few other research papers that take different approach to solve the problem of SSCI. The mitigation technique proposed in [42] uses LQR controller. The LQR controller uses a full-state observer to estimate the state variables, and the control from LQR is added to the converters to get the desired dynamic response. The research presented in [43] proposes a two-degree-of-freedom control strategy combined with a damping control loop to eliminate SSCI from the system. In [62], the mitigation of SSCI is proposed using the modulation of reactive power generated by DFIG, and by type-4 wind turbine using supplementary controls. An optimal quadratic technique is used to design a supplementary observer-based controller to damp SSCI in [63].

Chapter 3

Modelling of a DFIG-based Power System

As discussed in the previous chapter, the DFIG is the only type of wind turbine generator which is vulnerable to SSCI. In order to investigate the SSCI phenomenon thoroughly, a detailed mathematical model of DFIG is required. This chapter deals with the mathematical modelling of a DFIG-based power system. Ordinary differential equations are used to represent the dynamics of all the parts of the DFIG and the external network. The modelling of the system is mainly inspired by [65]. Simulation results for the normal operation of the DFIG-based system are also shown and discussed. The mathematical model derived here will be further analyzed in later chapters. The block diagram of the test system which is designed for carrying out the analysis of SSCI is shown in fig. 3.1.

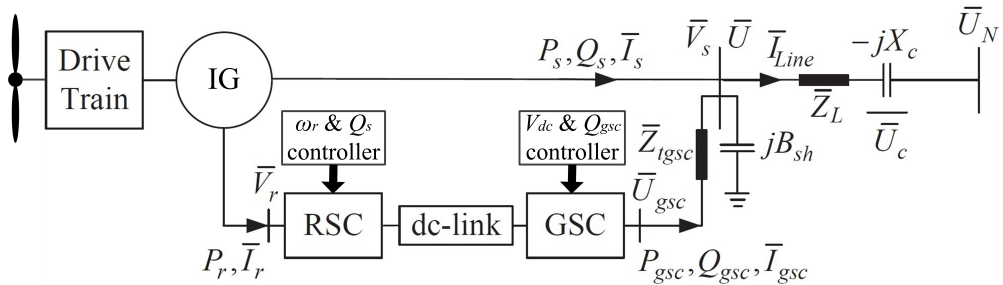


Figure 3.1: Block diagram of DFIG-based power system.

A single machine infinite bus (SMIB) model is used for the test of the DFIG-based system and to observe the occurrence of SSCI. It can be seen in fig. 3.1 that the DFIG is connected to an infinite bus through a series compensated transmission line having resistance R_L , reactance X_L , and impedance $\bar{Z}_L = R_L + jX_L$, while the reactance of the series compensation capacitor is X_C .

3.1 Modelling of DFIG

The DFIG consists of an induction generator whose stator is connected directly to the grid through a transformer, while the rotor is connected through a back-to-back converter. DFIG is capable of operating at the speed which can be below or above the synchronous speed to a certain limit. The back-to-back converter is further classified into two parts. The voltage source converter (VSC) close to the rotor of the generator is called rotor-side converter (RSC) and the converter close to the grid is called grid-side converter (GSC). There is a dc-link between the RSC and GSC with a purpose of storing the energy, and to enable the proper operation of both the converters. The converters being used in DFIG are of ratings lower than the rated power of DFIG. This is because the converters only deal with the fraction of total power.

The ordinary differential equations are used to model drive train, induction generator, RSC, GSC, dc-link, and grid-side transformer. The DFIG, as a whole, is modelled in dq coordinate system such that its q -axis leads d -axis by 90° , i.e., $\bar{V}_{dq} = V_d + jV_q$, and the external network is modelled in orthogonal two axes Real-Imaginary (RI) frame with the imaginary axis leading the real axis by 90° i.e., $\bar{U}_{RI} = U_{Re} + jU_{Im}$.

It is assumed that both the dq and RI frames are rotating with the synchronous speed ω_s , so the voltage \bar{V} at stator of DFIG is equal to its terminal voltage \bar{U} . It should be noted that the per unit system is used to represent all the quantities, unless otherwise stated. The following subsections discuss the modelling of each part of DFIG in detail. In every subsection, a table is shown which summarizes the details of state variables, input, and output of the concerned part of the DFIG.

3.1.1 Drive Train Model

Since the focus of this research work is to investigate a phenomenon which is purely electrical, therefore, the one-mass dynamic model for the drive train is con-

sidered here. Also, the mechanical damping of the drive train is neglected in order to achieve a worst case damping scenario. Being a simple model, it is not capable of showing the torsional oscillations in the system. As SSCI is non-torsional phenomenon so there is no need to add the torsional characteristics of mechanical part of the turbine and the one-mass model of drive train is sufficient for this study.

The one-mass dynamic model of the drive train is given by:

$$\dot{\omega}_r = \frac{1}{2H}(T_m - T_e) \quad (3.1)$$

where ω_r is the angular speed of the rotor, T_m is the mechanical torque of the turbine, and T_e is the electromagnetic torque of the generator. H is the inertia constant of an equivalent mass which is composed of the inertia constant of the turbine, shaft, and generator [40].

Table 3.1: Quantities of Drive Train Model

State Variables	Inputs from System	Calculated Outputs
ω_r	T_m : has a constant value. T_e : is taken from the induction generator block.	ω_r

3.1.2 Induction Generator Model

A wound-rotor induction generator is used in the DFIG with its stator windings connected to the AC grid directly, while its rotor windings are not short-circuited and are connected to the grid, through a back-to-back converter. In this thesis the induction generator is modelled in a dq coordinate system with its d and q components of the stator and rotor fluxes as the state variables. The rotating dq reference frame rotates with synchronous speed. Generator convention is used for the modelling of DFIG, i.e., the current is considered to be positive when it flows out of induction generator. The dynamics of induction generator can be represented mathematically by the following equations [40],

$$\dot{\psi}_{ds} = \omega_0(\omega_s \psi_{qs} + R_s I_{ds} + V_{ds}) \quad (3.2)$$

$$\dot{\psi}_{qs} = \omega_0(-\omega_s \psi_{ds} + R_s I_{qs} + V_{qs}) \quad (3.3)$$

$$\dot{\psi}_{dr} = \omega_0((\omega_s - \omega_r) \psi_{qr} + R_r I_{dr} + V_{dr}) \quad (3.4)$$

$$\dot{\psi}_{qr} = \omega_0(-(\omega_s - \omega_r) \psi_{dr} + R_r I_{qr} + V_{qr}) \quad (3.5)$$

where, ψ_{ds} , ψ_{qs} , ψ_{dr} , and ψ_{qr} are the d and q components of stator and rotor fluxes, respectively, V_{ds} , V_{qs} , V_{dr} , and V_{qr} are the d and q components of stator and rotor voltages, respectively. Moreover, I_{ds} , I_{qs} , I_{dr} , and I_{qr} are the d and q components of stator and rotor currents, respectively, and R_s and R_r are the stator and rotor winding resistance, respectively. The base angular speed and the synchronous speed are denoted by ω_0 and ω_s , respectively.

The stator and rotor current can be expressed in terms of flux by using the following equations,

$$\begin{aligned} I_{ds} &= \frac{L_{rr}}{\delta} \psi_{ds} - \frac{L_m}{\delta} \psi_{dr} \\ I_{qs} &= \frac{L_{rr}}{\delta} \psi_{qs} - \frac{L_m}{\delta} \psi_{qr} \\ I_{dr} &= \frac{L_{ss}}{\delta} \psi_{dr} - \frac{L_m}{\delta} \psi_{ds} \\ I_{qr} &= \frac{L_{ss}}{\delta} \psi_{qr} - \frac{L_m}{\delta} \psi_{qs}. \end{aligned} \quad (3.6)$$

In above equations, L_s , L_r , and L_m are the stator winding, rotor winding, and magnetizing inductances, respectively, and $L_{ss} = L_s + L_m$, $L_{rr} = L_r + L_m$, and $\delta = L_m^2 - L_{ss}L_{rr}$.

The electromagnetic torque of DFIG can be calculated based on (3.2)-(3.6) as,

$$T_e = \psi_{ds} I_{qs} - \psi_{qs} I_{ds}. \quad (3.7)$$

This electromagnetic torque is then used in the dynamics of drive train. The following table summarizes the state variables, inputs, and calculated outputs of induction generator block.

Table 3.2: Quantities of Induction Generator

State Variables	Inputs from System	Calculated Outputs
$\psi_{ds}, \psi_{qs}, \psi_{dr}$, and ψ_{qr}	V_{ds}, V_{qs} : Stator voltage is taken from the external grid model. V_{dr}, V_{qr} : Rotor voltage is taken from the RSC controller block. ω_r : Its value is taken from drive train model	$\psi_{ds}, \psi_{qs}, \psi_{dr}$, and ψ_{qr} $I_{ds}, I_{qs}, I_{dr}, I_{qr}$, and T_e

3.1.3 Rotor-Side Converter (RSC) Controller Model

A pulse width modulation (PWM) voltage source converter (VSC) is considered as the RSC. A simple model of VSC is chosen and its switching dynamics are neglected. The switching of the power electronic converters is very fast, and the frequency of switching is around 5 kHz, which is very high as compared to the frequency of interest, i.e., sub-synchronous frequency range. Also, these high switching frequencies can be easily filtered out of the system by the inductances of the transformers.

In the designed system, the terminal voltage (TV) reference frame is chosen to design the control strategy for both the RSC and GSC controllers. The direct and quadrature axes in TV frame are denoted by dt and qt , respectively, and same subscripts are used to denote the components of quantities in TV reference frame. In TV frame the dt -axis is aligned along the stator voltage of DFIG, i.e., \bar{V}_s , such that $V_{dts} = |\bar{V}_s|$ and $V_{qts} = 0$. It should be noted that the stator voltage of DFIG, V_s , and the terminal voltage U (see fig. 3.1) are same as mentioned earlier in Section 3.1. The alignment of TV reference frame can be depicted from fig. 3.2.

Using the quantities in TV reference frame, the active power of the stator P_s can be calculated as,

$$P_s = V_{dts}I_{dts} + V_{qts}I_{qts}. \quad (3.8)$$

Since $V_{qts} = 0$, (3.8) can be written as,

$$P_s = V_{dts}I_{dts}. \quad (3.9)$$

Now using the quantities in TV in (3.6) to get I_{dts} ,

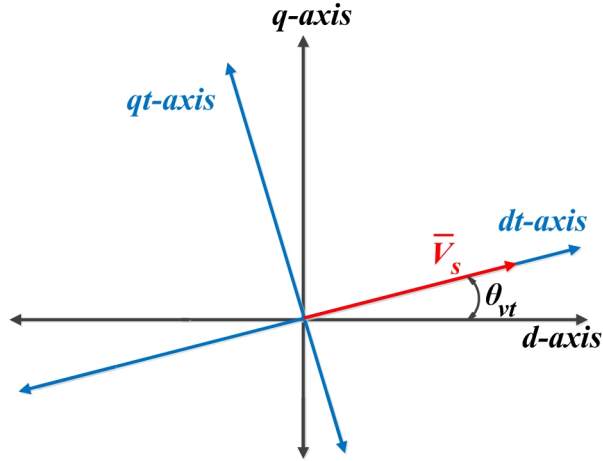


Figure 3.2: Visualization of TV reference frame.

$$I_{dts} = \frac{L_{rr}}{\delta} \psi_{dts} - \frac{L_m}{\delta} \psi_{dtr}, \quad (3.10)$$

using (3.6) the equation for I_{dtr} can be rearranged to get the equation for ψ_{dts} as,

$$\frac{\psi_{dts}}{\delta} = \frac{L_{ss} \psi_{dtr}}{L_m \delta} - \frac{I_{dtr}}{L_m}. \quad (3.11)$$

Putting the value of $\frac{\psi_{dts}}{\delta}$ in (3.10),

$$I_{dts} = L_{rr} \left(\frac{L_{ss} \psi_{dtr}}{L_m \delta} - \frac{I_{dtr}}{L_m} \right) - \frac{L_m \psi_{dtr}}{\delta}. \quad (3.12)$$

By putting $L_{rr}L_{ss} = L_m^2 - \delta$ in (3.12) and rearranging,

$$I_{dts} = \frac{1}{L_m} (-L_{rr} I_{dtr} - \psi_{dtr}). \quad (3.13)$$

By putting the value of I_{dts} in (3.9) the stator active power in TV frame can be written as,

$$P_s = \frac{V_{dts}}{L_m}(-L_{rr}I_{dtr} - \psi_{dtr}). \quad (3.14)$$

It can be seen in (3.14) that through I_{dtr} the active power of the stator can be controlled. The controller of RSC is designed in such a way that P_s is controlled through the dt component of rotor current and the corresponding reference rotor voltage $V_{dtr-ref}$ is generated which is then fed to PWM converter to get the desired rotor voltage V_{dtr} . Since in this thesis, a simple model of converters is considered, switching dynamics and losses are ignored. Therefore, the converters are considered to be transparent such that the generated voltage of PWM is equal to the reference voltage, i.e., $V_{dtr} = V_{dtr-ref}$.

Similarly, the qt component of rotor voltage is generated by controlling the reactive power of stator Q_s . In TV frame the reactive power of stator can be given as,

$$Q_s = V_{qts}I_{dts} - V_{dts}I_{qts} \quad (3.15)$$

$$Q_s = -V_{dts}I_{qts}. \quad (3.16)$$

Similar to I_{dts} , as in the case of P_s , the equation for I_{qts} can be derived in terms of rotor flux and current using the equation set (3.6) as,

$$I_{qts} = \frac{1}{L_m}(-L_{rr}I_{qtr} - \psi_{qtr}). \quad (3.17)$$

By putting I_{qts} in (3.16) the stator reactive power in TV frame can be written as,

$$Q_s = \frac{V_{dts}}{L_m}(L_{rr}I_{qtr} + \psi_{qtr}). \quad (3.18)$$

It can be seen in above equation that the stator reactive power can be controlled through the qt -axis component of the rotor current.

A cascade controller with a slower outer loop and a faster inner loop is used. The strategy of cascade control can allow the independent control of active and reactive power [66]. Simple PI controllers are used for the cascade control. The block diagram of the control strategy used for RSC controller is shown in fig. 3.3.

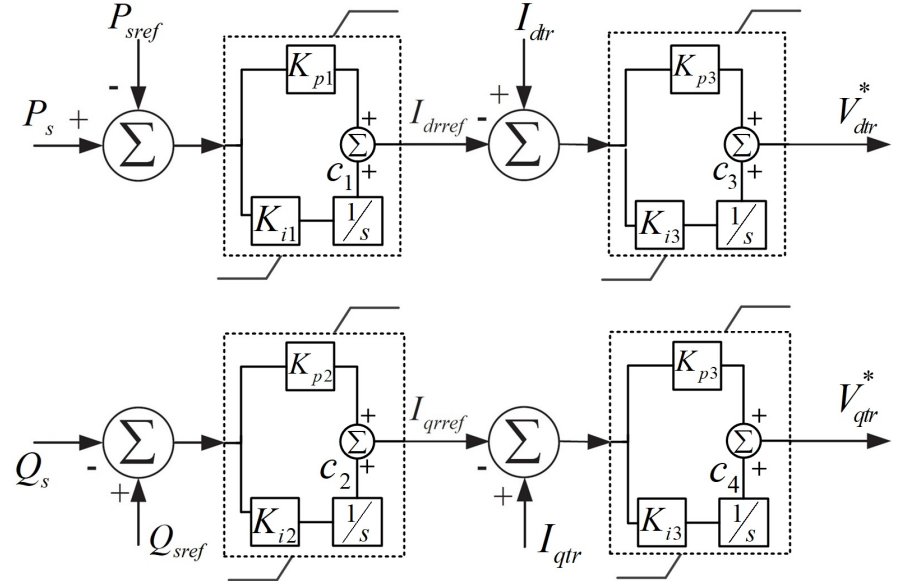


Figure 3.3: Block diagram of RSC controller.

K_{p1} , K_{p2} , and K_{p3} are the proportional control parameters of outer and inner control loop, respectively, while, K_{i1} , K_{i2} , and K_{i3} are the integral control parameters of outer and inner control loop, respectively. The value of these control parameters are initially selected based on work done in [36]. The equations which represent the dynamics of RSC controller are,

$$\begin{aligned}\dot{c}_1 &= K_{i1}(P_s - P_{sref}) \\ \dot{c}_2 &= K_{i2}(Q_{sref} - Q_s) \\ \dot{c}_3 &= K_{i3}(I_{dtr} - I_{drref}) \\ \dot{c}_4 &= K_{i3}(I_{qtr} - I_{qrref})\end{aligned}\tag{3.19}$$

$$\begin{aligned}I_{drref} &= K_{p1}(P_s - P_{sref}) + c_1 \\ I_{qrref} &= K_{p2}(Q_{sref} - Q_s) + c_2 \\ V_{dtr}^* &= K_{p3}(I_{dtr} - I_{drref}) + c_3 \\ V_{qtr}^* &= K_{p3}(I_{qtr} - I_{qrref}) + c_4.\end{aligned}\tag{3.20}$$

The differential equations in (3.19) represent the dynamics of integral part of the PI regulator, while the equations in (3.20) represent the overall dynamics of the controller.

Decoupled dq axes current tracking

In many references, the dq -axes decoupling is used for the converter controllers. To derive the decoupled converter controller, consider the set of equations in (3.6). By rearranging the equations, the d and q components of stator flux can be given in terms of currents as,

$$\begin{aligned}\psi_{ds} &= -(L_{ss}I_{ds} + L_mI_{dr}) \\ \psi_{qs} &= -(L_{ss}I_{qs} + L_mI_{qr}) \\ \psi_{dr} &= -(L_mI_{ds} + L_{rr}I_{dr}) \\ \psi_{qr} &= -(L_mI_{qs} + L_{rr}I_{qr})\end{aligned}\tag{3.21}$$

which will become,

$$\begin{aligned}\bar{\psi}_s &= \psi_{ds} + i\psi_{qs} \\ \bar{\psi}_s &= -(L_{ss}\bar{I}_s + L_m\bar{I}_r)\end{aligned}\tag{3.22}$$

and

$$\begin{aligned}\bar{\psi}_r &= \psi_{dr} + i\psi_{qr} \\ \bar{\psi}_r &= -(L_m\bar{I}_s + L_{rr}\bar{I}_r).\end{aligned}\tag{3.23}$$

By rearranging (3.22) and (3.23) and by eliminating \bar{I}_s from the two equations, it becomes,

$$L_{ss}\bar{\psi}_r = L_m\bar{\psi}_s + \sigma\bar{I}_r.\tag{3.24}$$

Now writing (3.4) and (3.5) in terms on rotating reference frame,

$$\begin{aligned}\dot{\psi}_r &= (\dot{\psi}_{dr} + i\dot{\psi}_{qr}) \\ \dot{\psi}_r &= \omega_0(R_r\bar{I}_r + \bar{V}_r - i(\omega_s - \omega_r)\bar{\psi}_r).\end{aligned}\tag{3.25}$$

Substituting $\bar{\psi}_r$ from (3.24) into (3.25) and solving for \bar{V}_r ,

$$\bar{V}_r = -R_r \bar{I}_r + \frac{L_m \dot{\psi}_s}{\omega_0 L_{ss}} + \frac{\sigma \dot{\bar{I}}_r}{\omega_0 L_{ss}} + i(\omega_s - \omega_r) \left(\frac{L_m \bar{\psi}_s}{L_{ss}} + \frac{\sigma \bar{I}_r}{L_{ss}} \right). \quad (3.26)$$

$$\bar{V}_r = -R_r \bar{I}_r + \frac{\sigma \dot{\bar{I}}_r}{\omega_0 L_{ss}} + i(\omega_s - \omega_r) \frac{\sigma \bar{I}_r}{L_{ss}} + \underbrace{\frac{L_m \dot{\psi}_s}{\omega_0 L_{ss}} + i(\omega_s - \omega_r) \frac{L_m \bar{\psi}_s}{L_{ss}}}_{\text{emf}}. \quad (3.27)$$

where the term *emf* represents the back emf of the generator.

The quantities in (3.27) can now be decomposed into their respective *d* and *q* components as,

$$\begin{aligned} V_{dr} &= -R_r I_{dr} + \frac{\sigma \dot{I}_{dr}}{\omega_0 L_{ss}} - \omega_{sr} \frac{\sigma I_{qr}}{L_{ss}} + \text{emf}_d \\ V_{qr} &= -R_r I_{qr} + \frac{\sigma \dot{I}_{qr}}{\omega_0 L_{ss}} + \omega_{sr} \frac{\sigma I_{dr}}{L_{ss}} + \text{emf}_q \end{aligned} \quad (3.28)$$

where $\omega_{sr} = \omega_s - \omega_r$. Rearranging (3.28) for \dot{I}_{dr} and \dot{I}_{qr} ,

$$\begin{aligned} \dot{I}_{dr} &= \frac{\omega_0 L_{ss}}{\sigma} \left(V_{dr} + R_r I_{dr} + \omega_{sr} \frac{\sigma I_{qr}}{L_{ss}} - \text{emf}_d \right) \\ \dot{I}_{qr} &= \frac{\omega_0 L_{ss}}{\sigma} \left(V_{qr} + R_r I_{qr} - \omega_{sr} \frac{\sigma I_{dr}}{L_{ss}} - \text{emf}_q \right) \end{aligned} \quad (3.29)$$

It can be seen clearly in (3.29) that in both the *d* and *q* axis component there is a cross-coupling. In order to achieve an independent control of *d* and *q* components of the quantities, in this case the rotor current, their components can be decoupled based on the control law described in [67]. Two virtual variables are introduced to decouple the cross coupling of *d* and *q* components and to compensate for the back emf of the generator,

$$\begin{aligned} V_{dr}^* &= V_{dr} + \omega_{sr} \frac{\sigma I_{qr}}{L_{ss}} - emf_d \\ V_{qr}^* &= V_{qr} - \omega_{sr} \frac{\sigma I_{dr}}{L_{ss}} - emf_q \end{aligned} \quad (3.30)$$

Substituting (3.30) in (3.29),

$$\begin{aligned} \dot{I}_{dr} &= \frac{\omega_0 L_{ss}}{\sigma} \left(V_{dr}^* + R_r I_{dr} \right) \\ \dot{I}_{qr} &= \frac{\omega_0 L_{ss}}{\sigma} \left(V_{qr}^* + R_r I_{qr} \right). \end{aligned} \quad (3.31)$$

It can be seen in (3.31) that the control of d and q components of the rotor current is now independent and also the back emf is compensated. Equation sets (3.30) and (3.31) are given for general control strategies. For control strategies in TV reference frame, the quantities of the virtual variables will change accordingly. The block diagram of RSC controller after the implementation of decoupling and emf compensation is shown in fig. 3.4.

There are many references that used the converter controller without the decoupling effect [68]. In this thesis, the theoretical analysis of SSCI is carried out using the model with decoupled converter controllers, as shown in fig. 3.4. Table 3.3 summarizes the relation of RSC controller block with other blocks of the design system, and makes the integration of this block, in the system, simple.

Conversion between reference frames

In order to control the RSC properly, all the concerned quantities should be converted in to TV reference frame from dq reference frame. And, the generated rotor voltage references must be converted in to dq reference frame from TV frame to be used in other blocks of the system. For example, the d and q components of rotor current I_{dr} and I_{qr} must be converted to I_{dtr} and I_{qtr} when being used for the calculations of RSC controller. The transformation from dq reference frame to TV reference frame is given by,

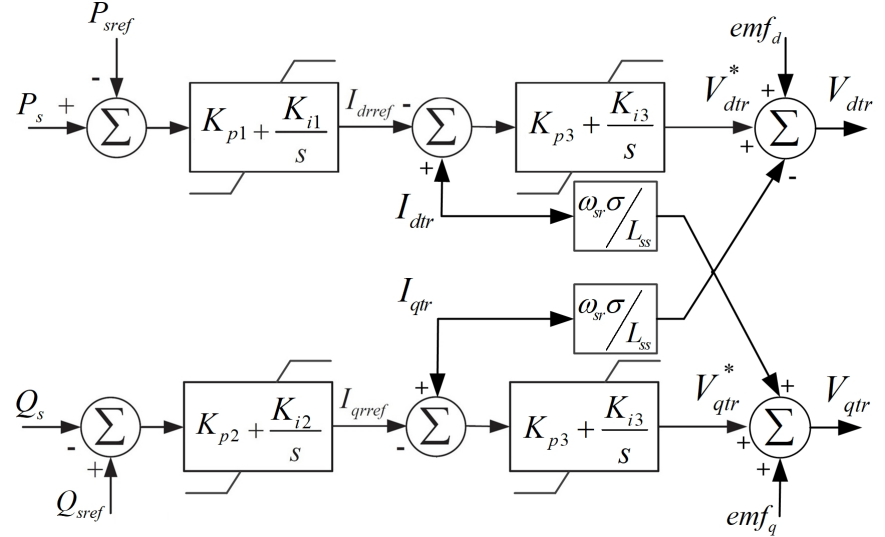


Figure 3.4: RSC controller with decoupling.

$$\begin{bmatrix} I_{dtr} \\ I_{qtr} \end{bmatrix} = \begin{bmatrix} \cos\theta_{vt} & -\sin\theta_{vt} \\ \sin\theta_{vt} & \cos\theta_{vt} \end{bmatrix} \begin{bmatrix} I_{dr} \\ I_{qr} \end{bmatrix} \quad (3.32)$$

where θ_{vt} is the angle between dq -axis of dq frame and dt -axis TV reference frames, as shown in fig. 3.2. As the dt -axis of TV frame is aligned along \bar{V}_s , so θ_{vt} is same as the angle between \bar{V}_s and d -axis and can be written as,

Table 3.3: Quantities of RSC Controller

State Variables	Inputs from System	Calculated Outputs
c_1, c_2, c_3 , and c_4	P_{s-ref}, Q_{s-ref} : Have constant defined values P_s and Q_s : Calculated by (3.9) and (3.16), V_{dts} and I_{dts} : taken from external network model and induction generator model, respectively, after converting to TV I_{dtr}, I_{qtr} : Are taken from induction generator model	V_{dtr} and V_{qtr}

$$\theta_{vt} = -\tan^{-1} \left(\frac{V_{qs}}{V_{ds}} \right). \quad (3.33)$$

After the components rotor voltage V_{dtr} and V_{qtr} are generated by RSC, these components need to be converted to ordinary dq reference frame from TV frame so that these components can be used for calculations outside the RSC model. The conversion from TV to dq reference frame is given by,

$$\begin{bmatrix} V_{dr} \\ V_{qr} \end{bmatrix} = \begin{bmatrix} \cos\theta_{vt} & \sin\theta_{vt} \\ -\sin\theta_{vt} & \cos\theta_{vt} \end{bmatrix} \begin{bmatrix} V_{dtr} \\ V_{qtr} \end{bmatrix}. \quad (3.34)$$

3.1.4 Grid-Side Converter (GSC) Controller Model

The controller of GSC is also designed in TV reference frame such that the dc-link voltage V_{dc} is controlled to get the dt -component of reference voltage $V_{dtg-ref}$, generated at GSC. The reference value of the qt -component of the GSC voltage $V_{qtg-ref}$ is generated by controlling the reactive power Q_g of GSC. The block diagram of GSC controller is shown in fig. 3.5. As considered in the design of RSC controller, the converters are lossless, that is why it is assumed that the voltage generated by the PWM converter is same as the reference voltage, i.e., $V_{dtg} = V_{dtg-ref}$ and $V_{qtg} = V_{qtg-ref}$.

Four PI controllers are used in the design of GSC controller. K_{p4} , K_{p5} , and K_{p6} are the proportional parameters of PI regulators and K_{i4} , K_{i5} , and K_{i6} are the integral parameters. The outer loops of the controller control dc-link voltage V_{dc} and reactive power generated by GSC Q_g , while the inner current control loops control I_{dtg} and I_{qtg} which are the dt and qt components of the current generated by GSC, respectively. The mathematical representation of GSC controller is given by the following equations,

$$\begin{aligned} \dot{c}_5 &= K_{i4}(V_{dc} - V_{dcref}) \\ \dot{c}_6 &= K_{i5}(Q_g - Q_{gref}) \\ \dot{c}_7 &= K_{i6}(I_{dgref} - I_{dtg}) \\ \dot{c}_8 &= K_{i6}(I_{qgref} - I_{qtg}) \end{aligned} \quad (3.35)$$

$$\begin{aligned}
 I_{dgref} &= K_{p4}(V_{dc} - V_{dcref}) + c_5 \\
 I_{qgref} &= K_{p5}(Q_g - Q_{gref}) + c_6 \\
 V_{dtg} &= K_{p6}(I_{dgref} - I_{dtg}) + c_7 \\
 V_{qtg} &= K_{p6}(I_{qgref} - I_{qtg}) + c_8,
 \end{aligned} \tag{3.36}$$

the reactive power generated by GSC can be calculated as,

$$Q_g = V_{qts}I_{dtg} - V_{dts}I_{qtg} \tag{3.37}$$

where V_{dts} and V_{qts} are the dt and qt components of stator voltage. The stator voltage is used here to calculate Q_g with computational ease, because Q_g is measured after the converter transformer, and the voltage after the converter transformer is \bar{V}_s/\bar{U} .

In equation set (3.35), c_5, c_6, c_7 , and c_8 are the state variables which represent the dynamics of integral part of PI regulator.

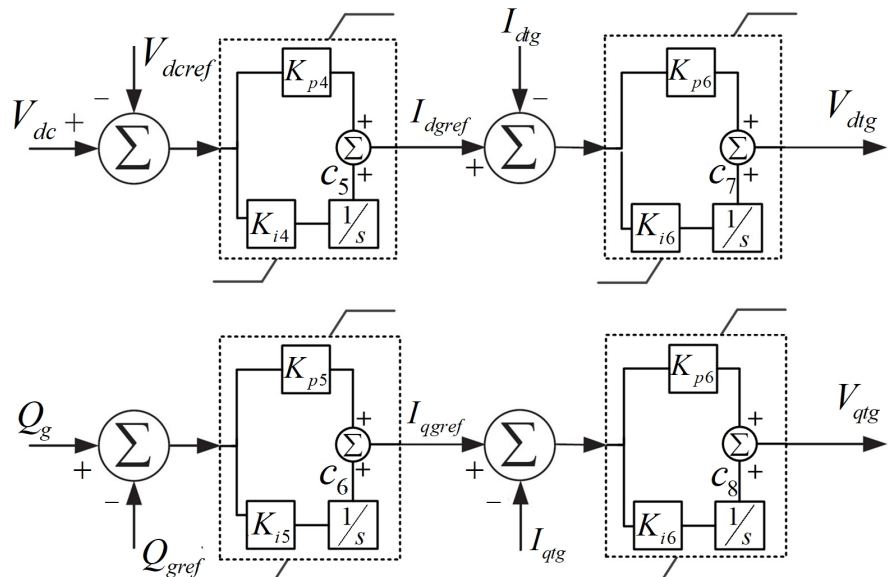


Figure 3.5: Block diagram of GSC controller.

The execution of GSC controller model gives V_{dtg} and V_{qtg} as the output. These voltages are in TV reference frame and must be converted to dq reference frame, i.e. $V_{dtg} \rightarrow V_{dg}$ and $V_{qtg} \rightarrow V_{qg}$, to be used outside the GSC controller block.

V_{dg} and V_{qg} are the d and q components of the GSC voltage in dq reference frame which are respectively equal to U_{Rgsc} and U_{Igsc} in RI reference frame because both the frames rotate with same speed, as mentioned in earlier Section 3.1,

$$\begin{aligned}\bar{V}_g &= \bar{U}_{gsc} \\ V_{dg} &= U_{Rgsc} \\ V_{qg} &= U_{Igsc}.\end{aligned}\tag{3.38}$$

The table below summarizes the state variable, inputs, and calculated output of GSC control model.

Table 3.4: Quantities of GSC Controller

State Variables	Inputs from System	Calculated Outputs
c_5, c_6, c_7 , and c_8	Q_{gref}, V_{dcref} : Have constant defined values Q_g : Calculated by (3.37), \bar{V}_s is taken from external network model and is converted to TV frame. I_{dtg} and I_{qtg} : taken from converter transformer model, and converted to TV frame V_{dc} : is taken from dc-link model	V_{dtg} and V_{qtg}

3.1.5 Converter Transformer Model

In this section the mathematical model of the transformer at GSC is discussed. This transformer is used to match the voltage generated by GSC with the terminal voltage of DFIG. The converter transformer is located between the GSC and the DFIG terminal, and the impedance of transformer is represented by \bar{Z}_{tgsc} , as shown in fig. 3.1. The dynamics of converter transformer can be represented by the following differential equations [36],

$$\dot{I}_{Rgsc} = \omega_0 \left(-\frac{R_g}{X_g} I_{Rgsc} + \omega_s I_{Igsc} + \frac{U_{Rgsc} - U_{Re}}{X_g} \right)\tag{3.39}$$

$$\dot{I}_{Igsc} = \omega_0 \left(-\frac{R_g}{X_g} I_{Igsc} - \omega_s I_{Rgsc} + \frac{U_{Igsc} - U_{Im}}{X_g} \right) \quad (3.40)$$

where R_g is winding resistance of transformer, X_g is its leakage reactance, and I_{Rgsc} and I_{Igsc} are R -axis and I -axis components of current generated by GSC \bar{I}_{gsc} . U_{Rgsc} and U_{Igsc} are R -axis and I -axis components of voltage generated by GSC, while U_{Re} and U_{Im} are the R -axis and I -axis components of terminal voltage of DFIG. Table 3.6 summarizes the integration of converter transformer model in to the other blocks of the system.

Table 3.5: Quantities of Converter Transformer Model

State Variables	Inputs from System	Calculated Outputs
I_{Rgsc} and I_{Igsc}	ω_0 : Base angular frequency U_{Rgsc}, U_{Igsc} : Obtained by converting the output of GSC model (V_{dtg} and V_{qtg}) in to dq/Rl reference frame U_{Re} and U_{Im} : Are equal to V_{ds} and V_{qs} respectively, and are taken from the external grid model	I_{Rgsc} and I_{Igsc}

3.1.6 DC-Link Model

The back-to-back converter has a dc-link which is the voltage-stiff connection between the two converters. This dc-link is mostly modelled as a pure capacitor, which means that the dynamics of dc-link are modelled as the dynamics of a capacitor. In this work the converters are assumed to be lossless. It means that the total power coming from the rotor P_r is equal to the total power going out from GSC P_{gsc} . The mathematical expressions for both the mentioned powers can be written as,

$$\begin{aligned} P_r &= V_{dr} I_{dr} + V_{qr} I_{qr} \\ P_{gsc} &= U_{Rgsc} I_{Rgsc} + U_{Igsc} I_{Igsc}. \end{aligned} \quad (3.41)$$

Fig. 3.6 shows the representation of the dc-link model. Since the total power coming in and going out of the back-to-back converter is same, so the dynamics of

the dc-link can be expressed as the power balance between RSC and GSC as the following differential equation,

$$\dot{V}_{dc} = \frac{P_r - P_{gsc}}{CV_{dc}} \quad (3.42)$$

where C is the capacitance of dc-link and V_{dc} is its voltage. The summary table of the dc-link model is given below.

Table 3.6: Quantities of DC-Link Model

State Variables	Inputs from System	Calculated Outputs
V_{dc}	V_{dr}, V_{qr} : Obtained after converting V_{dfr} and V_{qfr} in to dq reference frame I_{dr}, I_{qr} : Taken from induction generator model U_{Rgsc}, U_{Igsc} : Obtained by converting the output of GSC model (V_{dtg} and V_{qtg}) in to dq/RI reference frame I_{Rgsc}, I_{Igsc} : Taken from converter transformer model	V_{dc}

3.2 Modelling of External Network

Here, the whole DFIG-based test system is basically a single machine infinite bus (SMIB) system, with DFIG at one end of the transmission line and an infinite bus at another end, as shown in fig. 3.7. As mentioned in Section 3.1, the external

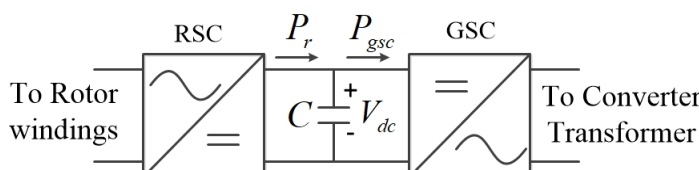


Figure 3.6: Block diagram of DC-link between converters.

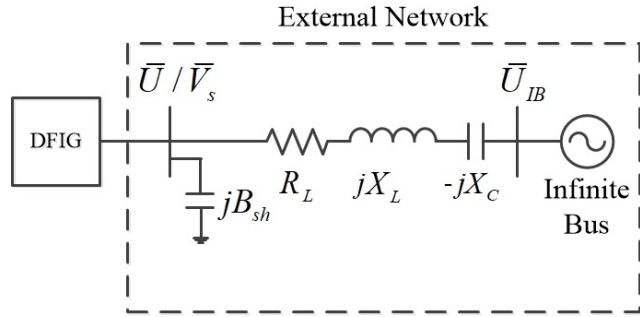


Figure 3.7: Single line diagram of external network.

network of the designed system is modelled in a Real-Imaginary (*RI*) reference frame with *I*-axis leading the *R*-axis by 90° .

There are total of three different rotating reference frames that are used for designing the DFIG, its controllers, and the external network. The illustration in fig. 3.8 simplifies the understanding of the use of different reference frames for designing the different parts of the test system.

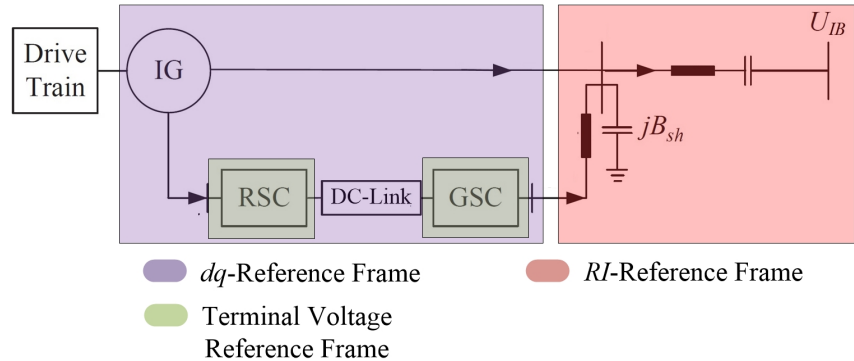


Figure 3.8: Different reference frames.

3.2.1 Shunt Capacitor at DFIG Terminal

In order to cater the reactive power demand of the generator, a local capacitor bank is used at the terminal of DFIG. The reactive power demand depends upon the terminal voltage of DFIG and its output power. In this research, a shunt capacitor is

connected at the point of common coupling to integrate the DFIG model with the external network. By adding this shunt capacitor, the mathematical integration of DFIG with external network becomes numerically stable, as this addition makes the terminal voltage of DFIG a state variable. Such strategy of making the terminal voltage, of the generator, a state variable is used in few other research work, but in those work a large fictitious resistor is used instead of shunt capacitor [36] [69]. According to [36], the EMTP inject the current in to the external network based on the currents and voltages from the calculation of previous steps. Then this injected current is used by the network model to calculate the new voltage which further calculates the new current for next time step. Because of the time delay, there can be a large mismatch between old and new current if there is sudden increase in voltage. Adding a fictitious large resistor can eliminate the numerical instability by introducing the variables of the terminal voltage which can be calculated at the same time step.

In order to derive the dynamic equation for shunt capacitor let us consider a simplified representation of the system in fig. 3.9.

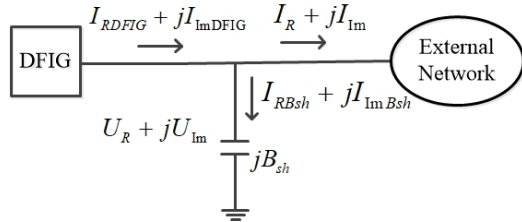


Figure 3.9: Connection of shunt capacitor between DFIG and network.

The quantities in the fig 3.9 are,

$$\begin{aligned}
 \bar{I}_{DFIG} &= I_{RDFIG} + jI_{ImDFIG} \\
 \bar{I} &= I_R + jI_{Im} \\
 \bar{I}_{Bsh} &= I_{RBsh} + jI_{ImBsh} \\
 \bar{U} &= \bar{V}_s = U_R + jU_{Im} \\
 B_{sh} &= \omega_s C_{sh}
 \end{aligned} \tag{3.43}$$

where, \bar{I}_{DFIG} is the total current generated by DFIG which is the sum of stator current \bar{I}_s and the current generated by GSC \bar{I}_{gsc} , \bar{I} is the current through transmission line in external network, \bar{I}_{Bsh} is the current in the shunt capacitance branch, and B_{sh}

and C_{sh} are the susceptance and capacitance of the shunt capacitor, respectively. In fig 3.9, applying the Kirchhoff's law at the point of common coupling,

$$\bar{I}_{DFIG} = \bar{I} + \bar{I}_{Bsh} \quad (3.44)$$

$$\bar{I}_{DFIG} = \bar{I} + C_{sh} \frac{d\bar{U}}{dt}. \quad (3.45)$$

Converting the equation from stationary reference frame to rotating *RI* reference frame, i.e., $\frac{d}{dt} \rightarrow \frac{d}{dt} + j\omega_s$

$$I_{RDFIG} + jI_{ImDFIG} = I_R + jI_{Im} + C_{sh} \frac{d}{dt} (U_R + jU_{Im}) + jC_{sh}\omega_s (U_R + jU_{Im}). \quad (3.46)$$

By rearranging and separating the real and imaginary parts of the above equation, the following expressions are obtained,

$$\begin{aligned} \frac{d}{dt} U_R &= \frac{1}{C_{sh}} (I_{RDFIG} - I_R + \omega_s C_{sh} U_{Im}) \\ \frac{d}{dt} U_{Im} &= \frac{1}{C_{sh}} (I_{ImDFIG} - I_{Im} - \omega_s C_{sh} U_R). \end{aligned} \quad (3.47)$$

By multiplying the right hand side of equation set (3.47) with base angular speed ω_o to de-normalize the time, and by replacing C_{sh} with B_{sh} , the following equations are obtained,

$$\begin{aligned} \dot{U}_R &= \dot{V}_{ds} = \frac{\omega_o \omega_s}{B_{sh}} (I_{RDFIG} - I_R + B_{sh} U_{Im}) \\ \dot{U}_{Im} &= \dot{V}_{qs} = \frac{\omega_o \omega_s}{B_{sh}} (I_{ImDFIG} - I_{Im} - B_{sh} U_R). \end{aligned} \quad (3.48)$$

By using the equation set (3.48), the DFIG model and external network model can be integrated together and the dynamics of stator/terminal voltage of DFIG can be represented. The summary of the state variables, inputs, and calculated outputs of this block is shown in Table 3.7.

3.2.2 Transmission Network Model

In this research work, the transmission network is a single transmission line connected to the DFIG from one end and an infinite bus from the other end. The transmission network is modelled in rotating *RI* reference frame. The *R*-axis of the

Table 3.7: Quantities of Shunt Capacitance Model

State Variables	Inputs from System	Calculated Outputs
$U_R/V_{ds}, U_{Im}/V_{qs}$	I_R, I_{Im} : Obtained from the transmission line model I_{RDFIG}, I_{ImDFIG} : The sum of currents taken from induction generator block and GSC transformer block	$U_R/V_{ds},$ U_{Im}/V_{qs}

RI -reference frame is aligned along the direction of the infinite bus voltage \bar{U}_{IB} , such that $U_{RIB} = |\bar{U}_{IB}|$ and $U_{IIB} = 0$, which equivalently mean that the angle which \bar{U}_{IB} makes with the R -axis of RI frame is zero. The magnitude of voltage at infinite bus is selected to be of nominal value, i.e., 1 pu, and its angle is 0° .

The model of the transmission line consists of line resistance R_L , line inductive reactance X_L , and a series compensated capacitive reactance X_C . a simple circuit diagram of the transmission network is shown in fig. 3.10.

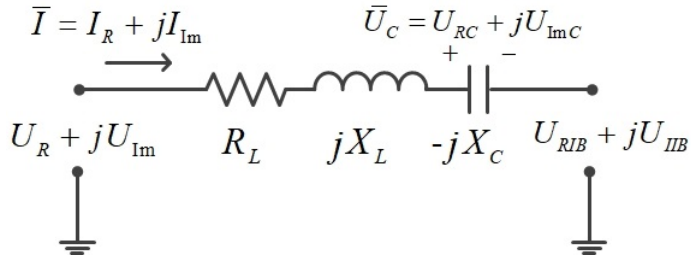


Figure 3.10: Single line diagram of external network.

By applying the Kirchhoff's voltage law in the transmission network circuit, the following equation is obtained,

$$\bar{U} = R_L \bar{I} + \frac{X_L}{\omega_s} \frac{d}{dt} \bar{I} + \bar{U}_C + \bar{U}_{IB}. \quad (3.49)$$

By using similar procedure, as in Section 3.2.1, to convert the above equation from stationary frame to rotating RI reference frame and to rearrange and separate the

real and imaginary quantities, the following equations are obtained,

$$\dot{I}_R = \frac{\omega_0 \omega_s}{X_L} (U_R - U_{RIB} - U_{RC} - R_L I_R + X_L I_{Im}) \quad (3.50)$$

$$\dot{I}_{Im} = \frac{\omega_0 \omega_s}{X_L} (U_{Im} - U_{IIB} - U_{ImC} - R_L I_{Im} X_L I_R), \quad (3.51)$$

where U_{RC} and U_{ImC} are the R and I components of the series compensation capacitor.

The dynamics of the voltage across the series compensation capacitor can be represented by the following equations,

$$\dot{U}_{RC} = \omega_o \omega_s (X_C I_R + U_{ImC}). \quad (3.52)$$

$$\dot{U}_{ImC} = \omega_o \omega_s (X_C I_{Im} - U_{RC}). \quad (3.53)$$

The equations (3.50), (3.51), (3.52), and (3.53) represent the dynamic of the whole transmission network.

Table 3.8: Quantities of Transmission Network Model

State Variables	Inputs from System	Calculated Outputs
$I_R, I_{Im}, U_{RC}, U_{ImC}$	U_R, U_{Im} : Obtained from shunt capacitance model	$I_R, I_{Im}, U_{RC}, U_{ImC}$

3.3 Initialization and Finding Equilibrium Points

As the aim of this research is to analyse the occurrence of SSCI through eigenvalue analysis, the designed model must be capable of being linearized. That is why the whole test system is designed using the differential equations and no pick-and-use blocks of simulink are used. In a summary, the dynamics of the designed DFIG-based power system is represented by the derivative $f(x)$ of state vector x , as given in (3.54). For the purpose of linearization of the test system, the initial

equilibrium points x_0 of the state variables must be calculated so that the system can be linearized around the accurate equilibrium points,

$$\dot{x} = \begin{bmatrix} \dot{\omega}_r \\ \dot{\psi}_{ds} \\ \dot{\psi}_{qs} \\ \dot{\psi}_{dr} \\ \dot{\psi}_{qr} \\ \dot{c}_1 \\ \dot{c}_2 \\ \dot{c}_3 \\ \dot{c}_4 \\ \dot{c}_5 \\ \dot{c}_6 \\ \dot{c}_7 \\ \dot{c}_8 \\ \dot{I}_{Rgsc} \\ \dot{V}_{dc} \\ \dot{V}_{ds} \\ \dot{V}_{qs} \\ \dot{I}_R \\ \dot{I}_{Im} \\ \dot{U}_{RC} \\ \dot{U}_{ImC} \end{bmatrix} = \begin{bmatrix} \frac{1}{2H}(T_m - T_e) \\ \omega_0(\omega_s \psi_{qs} + R_s I_{ds} + V_{ds}) \\ \omega_0(-\omega_s \psi_{ds} + R_s I_{qs} + V_{qs}) \\ \omega_0((\omega_s - \omega_r) \psi_{qr} + R_r I_{dr} + V_{dr}) \\ \omega_0(-(\omega_s - \omega_r) \psi_{dr} + R_r I_{qr} + V_{qr}) \\ K_{i1}(P_s - P_{sref}) \\ K_{i2}(Q_{sref} - Q_s) \\ K_{i3}(I_{dtr} - I_{drref}) \\ K_{i3}(I_{qtr} - I_{qrref}) \\ K_{i4}(V_{dc} - V_{dcref}) \\ K_{i5}(Q_g - Q_{gref}) \\ K_{i6}(I_{dgref} - I_{dtg}) \\ K_{i6}(I_{qgref} - I_{qtg}) \\ \omega_0(-\frac{R_g}{X_g} I_{Rgsc} + \omega_s I_{Igsc} + \frac{U_{Rgsc} - U_{Re}}{X_g}) \\ \omega_0(-\frac{R_g}{X_g} I_{Igsc} - \omega_s I_{Rgsc} + \frac{U_{Igsc} - U_{Im}}{X_g}) \\ \frac{P_r - P_{gsc}}{CV_{dc}} \\ \frac{\omega_o \omega_s}{B_{sh}} (I_{RDFIG} - I_R + B_{sh} U_{Im}) \\ \frac{\omega_o \omega_s}{B_{sh}} (I_{ImDFIG} - I_{Im} - B_{sh} U_R) \\ \frac{\omega_0 \omega_s}{X_L} (U_R - U_{RIB} - U_{RC} - R_L I_R + X_L I_{Im}) \\ \frac{\omega_0 \omega_s}{X_L} (U_{Im} - U_{IIB} - U_{ImC} - R_L I_{Im} X_L I_R) \\ \omega_o \omega_s (X_C I_R + U_{ImC}) \\ \omega_o \omega_s (X_C I_{Im} - U_{RC}) \end{bmatrix} = f(x). \quad (3.54)$$

To start the calculations for equilibrium points of the system, consider the system shown in fig. 3.7. The bus connected to DFIG is considered as a *PU* bus, with the known value of active power and the voltage magnitude, while the infinite bus is considered as a slack bus with the known values for voltage magnitude and angle. Based on the known values, the load flow calculations are carried out. The results from load flow calculations determined the values of active power, reactive power, voltage magnitude, and voltage angle of both the buses.

Knowing the magnitude and angle of the DFIG bus, the values of *R*-axis and

I-axis components of terminal voltage of DFIG can be easily calculated by

$$\begin{aligned}\bar{U}_0 &= \bar{V}_{s0} = U_{R0} + jU_{Im0} \\ U_{R0} &= V_{ds0} = V_s \cos \theta_s \\ U_{Im0} &= V_{qs0} = V_s \sin \theta_s.\end{aligned}\quad (3.55)$$

The current through the transmission line and the voltage across series capacitor can also be calculated by using the following equation:

$$\begin{aligned}\bar{I}_0 &= \frac{\bar{V}_{s0} - \bar{U}_{IB0}}{R_L + j(X_L - X_C)} \\ I_{R0} &= Re[\bar{I}_0] \\ I_{Im0} &= Im[\bar{I}_0]\end{aligned}\quad (3.56)$$

$$\begin{aligned}U_{RC0} &= X_C I_{Im0} \\ U_{ImC0} &= X_C I_{R0}.\end{aligned}\quad (3.57)$$

Using (3.55), (3.56), and (3.57) the initial values of all the state variables that represent the external network dynamics, can be calculated.

To calculate the equilibrium value of state variables of DFIG, first of all the active and reactive power of stator and rotor should be calculated. The generated active power of DFIG at the terminal is basically the sum of stator power P_{s0} and the power generated by GSC P_{gsc0} . Since the converters are assumed to be lossless therefore rotor power P_{r0} would be $P_{r0} = P_{gsc0}$,

$$P_{DFIG0} = P_{s0} + P_{r0}. \quad (3.58)$$

Looking at the side of turbine the mechanical power of turbine P_{m0} would be,

$$\begin{aligned}P_{m0} &= P_{s0} + P_{r0} \\ P_{r0} &= P_{m0} - P_s = T_{m0} \omega_{r0} - T_{e0} \omega_{s0}.\end{aligned}\quad (3.59)$$

During steady state both the electrical and mechanical torque, T_{e0} and T_{m0} respectively, would be equal so (3.59) becomes,

$$P_{r0} = -s_{slip0} P_{s0} \quad P_{s0} = \frac{P_{DFIG0}}{1 - s_{slip0}} \quad (3.60)$$

where s_{slip0} is the slip of a generator. Using (3.60) the active power of stator and rotor can be determined.

The reactive power generated by the DFIG Q_{DFIG0} at its terminal is the sum of reactive power of stator Q_{s0} and the reactive power generated by GSC Q_{gsc0} . Since the controller of GSC is selected such that no reactive power is generated at GSC so $Q_{gsc0} = 0$, which implies that $Q_{DFIG0} = Q_{s0}$.

The expression for the active and reactive power of stator are,

$$\begin{aligned} P_{s0} &= V_{ds0} I_{ds0} + V_{qs0} I_{qs0} \\ Q_{s0} &= V_{qs0} I_{ds0} - V_{ds0} I_{qs0}. \end{aligned} \quad (3.61)$$

As the active power, reactive power, and the voltage of stator are known so the stator current can be easily found using the equation set (3.61). The initial values of stator flux $\bar{\psi}_{s0}$, rotor flux $\bar{\psi}_{r0}$, and rotor voltage \bar{V}_{r0} are determined using the following equations,

$$\begin{aligned} \bar{\psi}_{s0} &= -j\bar{V}_{s0} \\ \psi_{ds0} &= Re[\bar{\psi}_{s0}] \\ \psi_{qs0} &= Im[\bar{\psi}_{s0}] \end{aligned} \quad (3.62)$$

$$\begin{aligned} \bar{I}_{r0} &= -\frac{1}{L_m}(\bar{\psi}_{s0} + L_s \bar{I}_{s0}) \\ I_{dr0} &= Re[\bar{I}_{r0}] \\ I_{qr0} &= Im[\bar{I}_{r0}] \end{aligned} \quad (3.63)$$

$$\begin{aligned} \bar{\psi}_{r0} &= -(L_r \bar{I}_{r0} + L_m \bar{I}_{s0}) \\ \psi_{dr0} &= Re[\bar{\psi}_{r0}] \\ \psi_{qr0} &= Im[\bar{\psi}_{r0}] \end{aligned} \quad (3.64)$$

$$\begin{aligned}\bar{V}_{r0} &= js\bar{\psi}_{r0} \\ V_{dr0} &= \text{Re}[\bar{V}_{r0}] \\ V_{qr0} &= \text{Im}[\bar{V}_{r0}].\end{aligned}\tag{3.65}$$

(3.63) and (3.64) are derived from the equation set (3.6). The power mismatch equations, as given below,

$$0 = P_{DFIG0} - P_{s0} - P_{r0}\tag{3.66}$$

$$0 = Q_{DFIG0} - Q_{s0}\tag{3.67}$$

From the obtained values the equilibrium values of all other state variables of the DFIG model can easily be obtained, in a similar way, from their respective differential equations.

3.4 Observation of the SSCI

After the design of a stable DFIG-based test system, it is tested under different circumstances to observe the occurrence of SSCI in it. As during the actual event of SSCI, there was a change in system topology after a transmission line was tripped. The new topology left the wind farm in radial connection with the series compensated transmission line. This change in topology can be comprehended as the increase in series compensation level, as the tripping of a transmission line decreased the equivalent inductive reactance of the system. Hence, the equivalent compensation level also increased. The percentage series compensation can be calculated as

$$\text{Percentage Series Compensation} = \frac{X_C}{X_L} \times 100.\tag{3.68}$$

Based on the above equation, if the equivalent inductive reactance decreases then, even the capacitive reactance being unchanged, the percentage compensation will increase. So, it can be said that in the actual even when the DFIG-based wind farm came in radial connection with the series compensated line, the equivalent series compensation faced by wind farm increased and the SSCI was inflicted. In

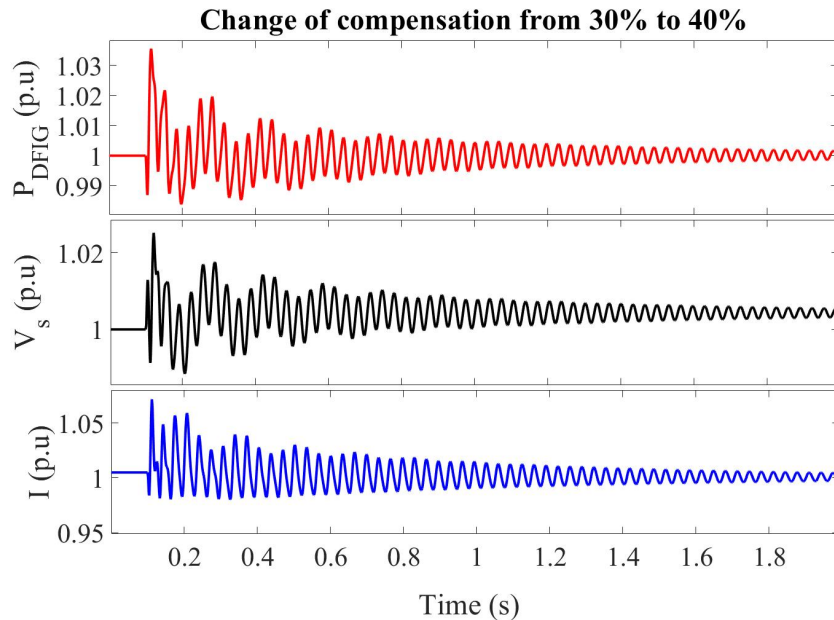


Figure 3.11: Response of system for increase in compensation to 40%.

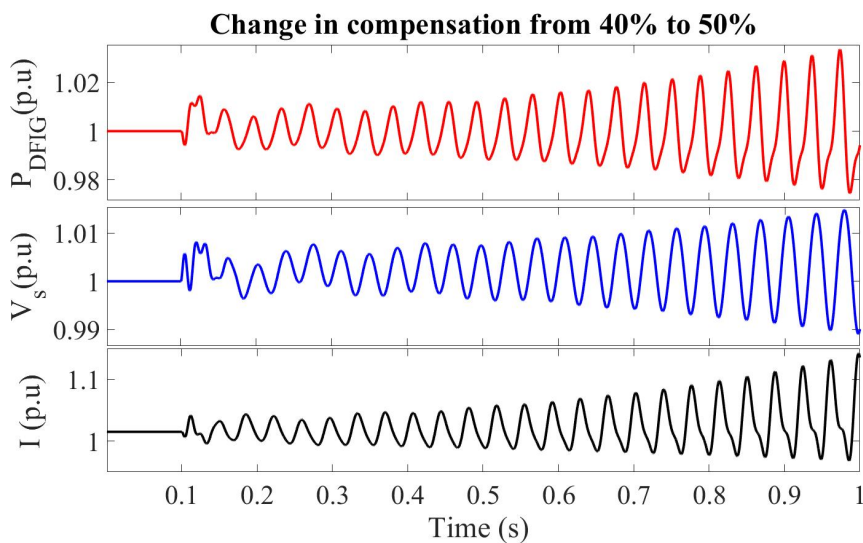


Figure 3.12: Response of system for increase in compensation to 50%.

order to put the designed test system into similar circumstances, the compensation level of the transmission line is increased to see if the mathematical model is capable of capturing the dynamics of SSCI. For the simulation, the series compensation level of the transmission line is increased from 0% with the steps of 10% compensation. For the initial steps, no interaction and undamped oscillations are observed, and the system gets back to stability after the disturbance. Fig. 3.11 shows the simulation of the active power of DFIG P_{DFIG} , the magnitude of its terminal voltage V_s , and the current through transmission line I , when the compensation level of the transmission line is stepped up from 30% to 40%.

The undamped oscillations come into existence when the compensation level of the system is changed from 40% to 50%, as shown in fig. 3.12. These undamped oscillations are because of the increase in compensation level to an extent when the system gets vulnerable to SSCI. While looking at the simulation results, without any analytical explanation, it can be said that the SSCI occurs in the system when the compensation level is increased beyond 50%. The analytical reasoning for the infliction of SSCI for higher compensation levels will be given in the subsequent chapter.

Chapter 4

Eigenvalue Analysis & Infliction of SSCI in DFIG-based Power System

This chapter deals with the analysis of the occurrence of SSCI in DFIGs. In order to investigate the interaction between DFIG and series compensated transmission line, the eigenvalue analysis is used as a tool. Based on the analysis, certain reasons for the infliction of SSCI are concluded. The effect of all the control parameters of DFIG's converter controllers are analyzed. The parameters of DFIG controllers that play significant role, in generating SSCI condition, are pointed out based on eigenvalue sensitivity analysis. The effect of different series compensation levels, rotor speeds, and generated power of the DFIG are taken into consideration. Moreover, the infliction of SSCI is explained and it is shown analytically that how and why these components and parameters play a role in the occurrence of SSCI in DFIG-based power system.

4.1 Eigenvalue Analysis of the DFIG-based Power System

Out of all the other analytical tools, as described in Section 2.4.2, eigenvalue analysis is selected in this research work. Although the eigenvalue analysis requires a detailed mathematical model of the system to be carried out, but the information

which it gives is much valuable for pursuing the investigation of the concerned phenomena. This tool is capable of computing the characteristics of the oscillation in terms of frequencies and the damping at each frequency. Such characteristics play an essential in the investigation of SSCI.

Eigenvalues

To find the eigenvalues, the designed system of differential equations $f(x)$ in (3.54) is linearized around its equilibrium points x_0 , which were calculated in Section 3.3. Consider a non-linear system with the dynamics as represented by the following equation,

$$\begin{aligned}\dot{x} &= f(x, u) \\ y &= h(x).\end{aligned}\tag{4.1}$$

The non-linear system in (4.1) can be linearized around its equilibrium points in to a linear time invariant (LTI) system. The dynamics of the LTI system can be written as,

$$\begin{aligned}\Delta\dot{x} &= A\Delta x + B\Delta u \\ \Delta y &= C\Delta x.\end{aligned}\tag{4.2}$$

Here, n state variables are included in the perturbation state vector Δx , the perturbation form of the output signal is denoted by Δy and it contains m outputs, whereas Δu represents the perturbation form of input signal and contains r inputs. A is the state matrix of dimension $n \times n$, B is the input matrix of dimension $n \times r$, and C is the output matrix of dimension $m \times n$. The state matrix A can be calculated by the following equation.

$$A = \left[\begin{array}{cccc} \frac{\partial f_1(x)}{x_1} & \frac{\partial f_1(x)}{x_2} & \dots & \frac{\partial f_1(x)}{x_n} \\ \frac{\partial f_2(x)}{x_1} & \frac{\partial f_2(x)}{x_2} & \dots & \frac{\partial f_2(x)}{x_n} \\ \vdots & \vdots & \ddots & \vdots \\ \frac{\partial f_n(x)}{x_1} & \frac{\partial f_n(x)}{x_2} & \dots & \frac{\partial f_n(x)}{x_n} \end{array} \right]_{n \times n}\tag{4.3}$$

where x_n is the n th state variable of the designed system and $f_n(x)$ describes the dynamics of the respective n th state variable.

After obtaining the A matrix using (4.3), the eigenvalues of the system λ can be determined as,

$$\det(A - \lambda II) = 0 \quad (4.4)$$

where II is the identity matrix. Each eigenvalue corresponds to a mode of the system. The eigenvalues of the system, calculated at a specific equilibrium point, determine the stability of system at that point.

For a system the eigenvalues can be real or complex. A real eigenvalue corresponds to a non-oscillatory mode while a complex eigenvalue corresponds to an oscillatory mode. The i th oscillatory mode of the system is expressed by

$$\lambda_i = \sigma_i \pm j\omega_i, \quad (4.5)$$

where σ_i is the real part of the i th mode and gives its damping, and the imaginary part of the i th mode, ω_i , gives its angular frequency. If the real part of the eigenvalue is negative then it shows that the mode is oscillatory damped, and if it is positive, the mode is unstable.

There is another ratio which is used widely to determine the stability of a particular mode, known as damping ratio. The damping ratio of i th mode of the system is given by

$$\zeta_i = \frac{-\sigma_i}{\sqrt{\sigma_i^2 + \omega_i^2}}. \quad (4.6)$$

Naturally, a stable system will have a positive damping ratio for all the modes. Higher the damping ratio of a particular mode, highly damped the mode will be. In this thesis the damping ratio is used to analyze the stability of the modes of interest during the investigation of SSCI.

4.1.1 Computed Eigenvalues of DFIG Test System

The non-linear DFIG-based test system is linearized around its equilibrium point and the state matrix A is computed using the equations (4.2) and (4.3). The eigen-

values of the linearized system are then determined by (4.4).

It was presented in the previous chapter, in Section 3.4, that designed system remained stable below 50% series compensation level and experienced undamped oscillations at 50% compensation level. Here, the eigenvalues of the system for both the circumstances are analyzed. Fig. 4.1 shows the scattered plot of the calculated eigenvalues of the system with 35% series compensation level (with blue crosses) and with 50% series compensation level (with red crosses). It can be seen that most of the modes of the system have high damping ratio for both the circumstances except for the modes which are inside the dotted box.

The zoomed-in version of the dotted box in fig. 4.1 is shown in fig. 4.2. It can be seen that the complex conjugate pairs of two modes have the lowest damping ratio when the compensation level is 35%, and one of those pairs even gets negative damping ratio when the compensation level is 50%. The pair of modes with the least damping ratio ζ and with the frequency less than 50 Hz are classified sub-synchronous (SUB) modes and the pair of modes with frequency higher than 50 Hz are classified as super-synchronous (SUP) modes. The damping ratio and frequency characteristics of these modes are shown in Table 4.1.

From fig. 4.2 it can be analyzed that the increase in series compensation level

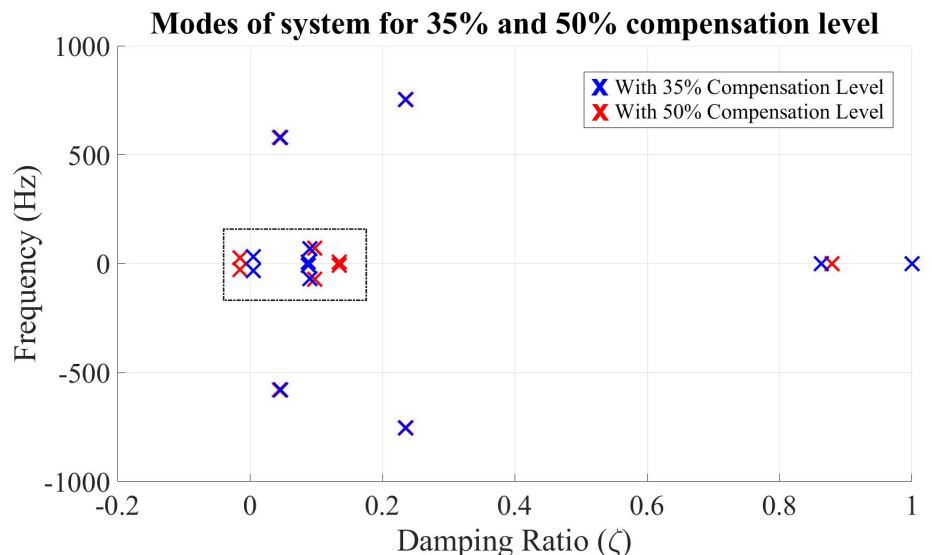


Figure 4.1: Eigenvalues of the system.

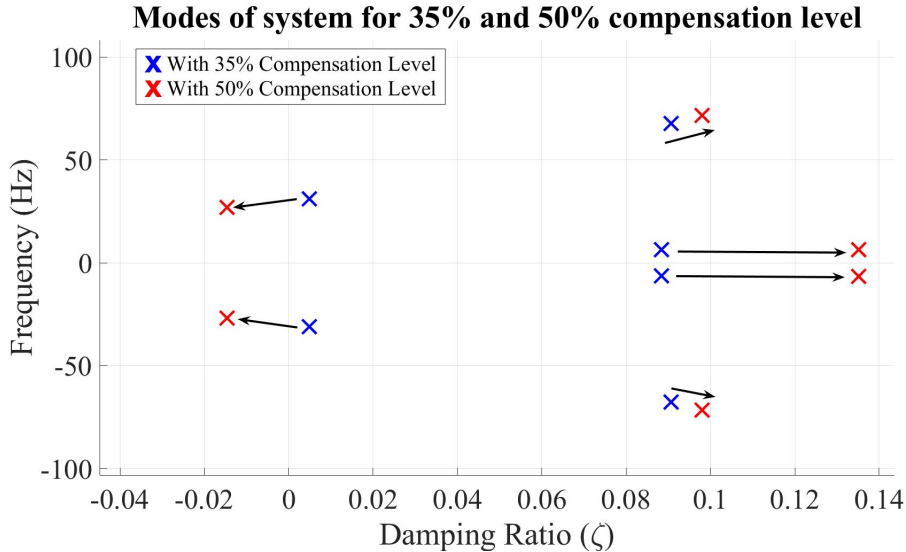


Figure 4.2: Eigenvalues of the system zoomed-in.

Table 4.1: Eigenvalues of Modes of Interest

Modes with 35% Compensation		
Eigenvalues	Frequency (Hz)	Damping Ratio
$-0.94 \pm i195.4$	31.1	0.005
$-38.7 \pm i426.2$	67.8	0.091
Modes with 50% Compensation		
Eigenvalues	Frequency (Hz)	Damping Ratio
$2.47 \pm i169.5$	26.9	-0.014
$-44.3 \pm i450.1$	71.6	0.097

significantly affects the SUB modes in an adverse way. The movement of eigenvalues corresponding to both the modes of the system is shown with arrows. As the compensation level increased from 35% to 50%, the SUB modes move towards the left plane, having the negative damping ratio, hence making the system unstable. On the other hand, the increase in compensation level slightly affects the SUP modes, but in a positive way, as it can be seen from fig. 4.2 and Table 4.1. There is another mode of sub-synchronous frequency in fig. 4.2, but this mode does not seem to threaten the stability of the system with the increase in compensation level,

therefore it is not of the interest in this analysis.

From above analysis of eigenvalues, corresponding to SUB and SUP modes, it can be said that the oscillation observed in the designed system in Section 3.4 are the SSO, as the mode which was responsible for causing those undamped oscillations is of sub-synchronous frequency range.

4.1.2 Effects of Different Compensation Levels

As seen in previous section, an increase in the compensation level of the DFIG system, beyond a certain percentage, made the system unstable and it experienced undamped oscillation after being disturbed. In this section the effect of series compensation level on the modes of interest is observed. The series compensation level of the system is increased from 1% to 70% in order to check the movement of system modes, as a response to this change. Fig. 4.3 shows the eigenvalue movements of all the modes of the system. The direction of increasing size of the marker can be comprehended as the increase in series compensation level. As it can be seen in the figure that when the compensation level is changed from 1% to 70%, all the

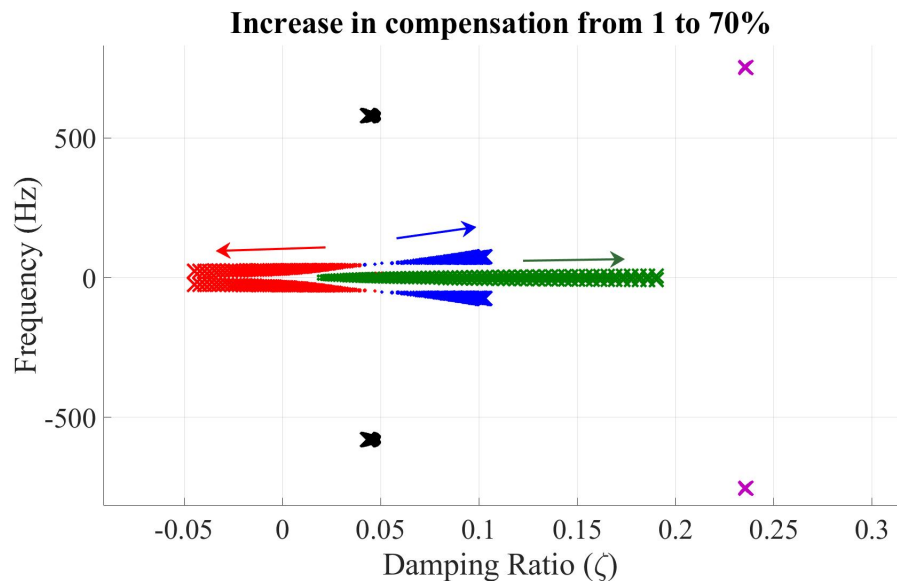


Figure 4.3: Effect of series compensation level.

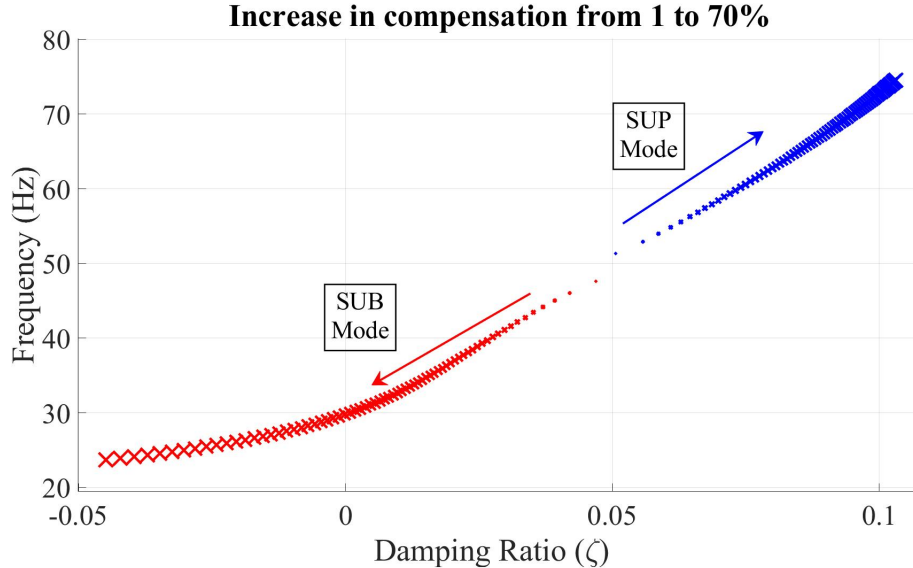


Figure 4.4: Effect of series compensation level zoomed-in.

modes of system remain stable with positive damping ration except for the SUB mode.

By zooming in to the modes of interest in fig. 4.3, the movement of eigenvalues corresponding to SUB and SUP modes can be clearly observed. Fig. 4.4 shows the zoomed-in plot for the movement of the modes with respect to the increase in series compensation level. It can be seen that initially, at 1% compensation, the SUB mode has almost similar damping ratio as compared to SUP mode. As the compensation level increases, the SUB mode deteriorates. On the contrary, the damping ratio of SUP mode improves with the increase in the series compensation. The increase in series compensation level makes the system vulnerable to SSCI by significantly affecting the mode of sub-synchronous frequency range.

4.1.3 Effect of Different Rotor Speed and Generated Power

The effect of wind speed on the SSCI conditions is also analyzed by observing the movement of SUB and SUP modes for different rotor speed. The compensation level of the transmission line is set equal to 40% and the speed of rotor is varied from 0.9 to 1.2 p.u. The movement of modes of interest for this range of speed is

Increase in ω_r from 0.9 to 1.2 p.u. with 40% compensation

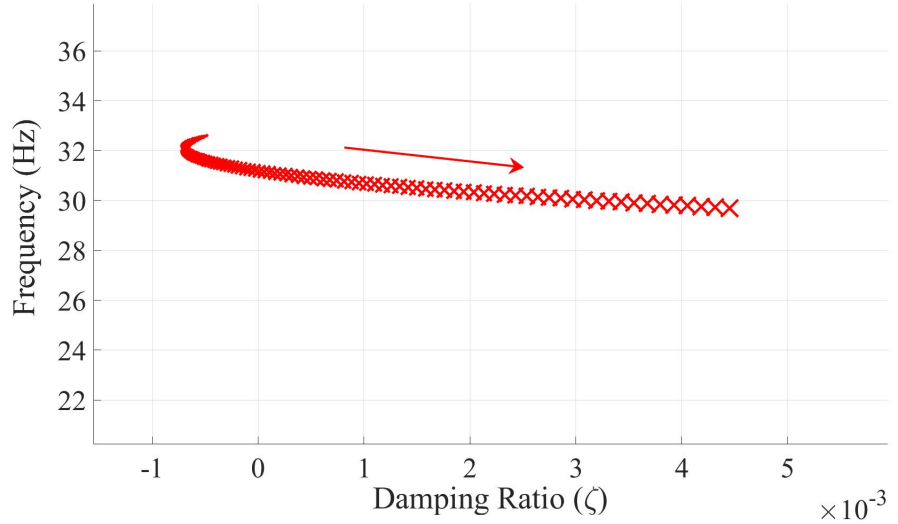


Figure 4.5: Effect of different rotor speed ω_r on SUB mode.

shown in fig. 4.5. Again, the increasing size of the markers depicts the increase in the rotor speed.

It can be seen in the figure that the SUB mode has the least damping ratio, initially, when the speed of rotor is set to 0.9 p.u. As the speed of rotor is increased, the damping ratio of SUB mode also increases while making it stable. Considering the analysis above, it can be concluded that wind speed can play a role in inflicting or avoiding the SSCI condition up to a certain level, but this role is not very significant.

The impact of the generated power of DFIG on the SSCI condition is also analyzed. The generated power of DFIG is initially set to 0.9 p.u. and then varied up to 1.2 p.u. The movement of eigenvalues corresponding to SUB modes is shown in fig. 4.6. It can be observed in the figure that the increase in the generated power increases the damping ratio of SUB mode. It can be said that the pattern of movement of both the modes is same as was in the case of different rotor speed ω_r .

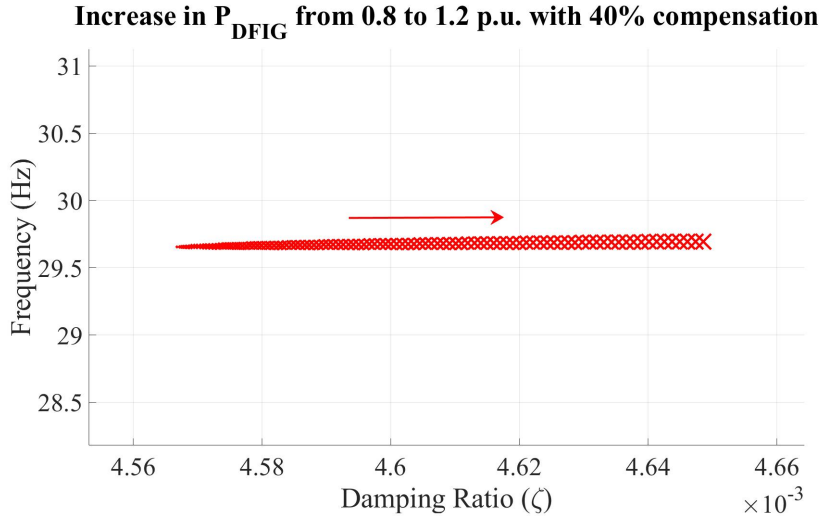


Figure 4.6: Effect of generated DFIG power on SUB mode.

4.1.4 Sensitivity Analysis of Control Parameters

The term control parameter is referred to the proportional and integral parameters of the PI controllers of VSC. The designed DFIG system uses 8 PI regulators, 4 in RSC and 4 in GSC, and a total of 16 control parameters. In the DFIG model, 8 state variables represent the dynamics of the integral part of PI controllers. The block diagrams of RSC and GSC controllers are shown in fig. 3.3 and fig. 3.5, respectively.

In order to find out the control parameters to which the modes of interest are sensitive, the eigenvalue sensitivity analysis is performed. This analysis is performed by changing the value of each parameter, turn by turn, and observing the movement of eigenvalues corresponding to the modes of interest. The series compensation level of the system is kept to be 40% so that the SUB modes becomes poorly damped but the system stays in stable region. The value of each control parameter is increased from 0 to a certain value to see the impact of each parameter. Broadly, all the 16 control parameters of the system are classified in to 4 groups based on their effect on the modes of the system. The classification of control parameters is shown in Table 4.2.

Table 4.2: Classification of Control Parameters

Type	Parameters	Property
A	$K_{i1}, K_{i2}, K_{i3}, K_{i4}, K_{i5}, K_{i6}, K_{p4}$, and K_{p5}	No significant effect on SUB and SUP mode
B	K_{p6}	has a specific range of values with stable SUB mode
C	K_{p1} and K_{p2}	Increase in the value of parameters decreases the damping ratio of SUB modes considerably
D	K_{p3}	Increase in the value of parameters affects the SUB mode significantly

Type A Parameters

Type A parameters are those which do not affect the SUB as well as SUP modes significantly. In the designed DFIG system, all the integral control parameters are not sensitive to the modes of interest. While observing the movement of eigenvalues, all the parameters in type A, given in Table 4.2, are increased from 0 to 100 p.u. Even for this larger range the eigenvalues corresponding to SUB and SUP mode do not show any appreciable movement. Fig. 4.7 shows the movement of eigenvalues when 3 out of 6 integral parameters are varied, one by one. It can be seen that displacement of eigenvalues of SUB and SUP modes is very small with respect to the large change in the values of the control parameters. Also for the two proportional parameters of the outer control loop of GSC, K_{p4} , and K_{p5} , there was no significant effect on the modes of interest, as shown in fig. 4.8

Type B Parameters

The parameters K_{p6} is classified as Type B because of its peculiar effect on the modes on interest. The response of SUB and SUP modes is observed while changing the values of K_{p6} from 0 to 2. The resultant movement of eigenvalues shows that the increase in K_{p6} has a appreciable impact on the movement of SUB and SUP mode, but for SUB mode there is a very small range of values of K_{p6} for which the damping ratio is positive, as shown in fig. 4.9. This means that the value of K_{p6} should be selected carefully to keep the damping ration of SUB mode positive.

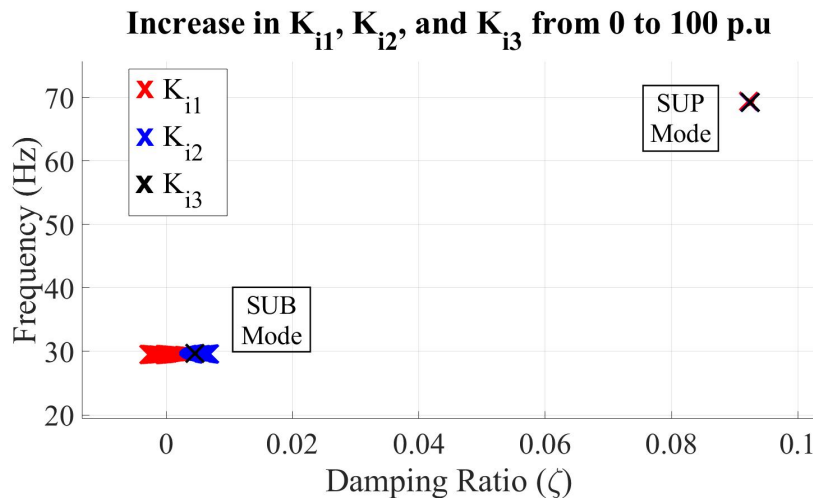


Figure 4.7: Effect of integral parameters on SUB and SUP modes.

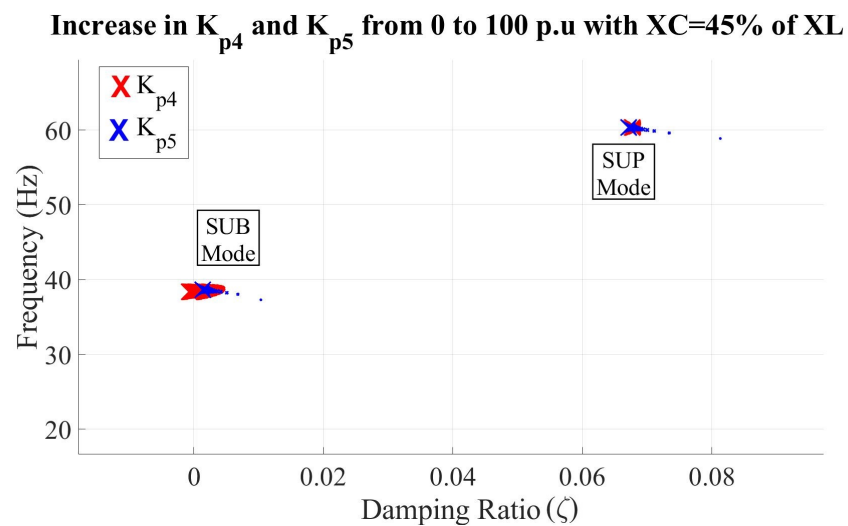


Figure 4.8: Effect of K_{p4} and K_{p5} on SUB and SUP modes.

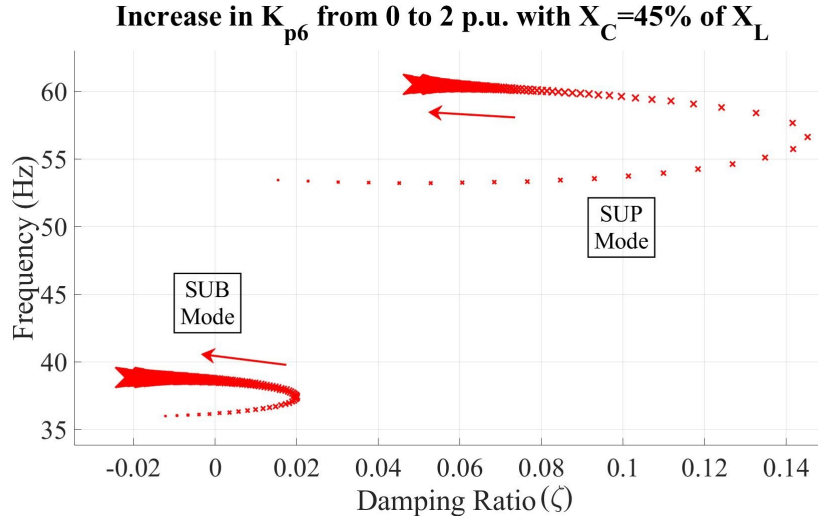


Figure 4.9: Effect of K_{p6} on SUB and SUP modes.

Type C Parameters

The proportional parameters of the outer power control loop of RSC, K_{p1} and K_{p2} , are classified as Type C for having a considerable effect on SUB mode. Fig. 4.10 shows the response of the SUB and SUP modes with the increase in K_{p1} and K_{p2} , one by one. For both the parameters, only the increase of 5 p.u. manages to push the SUB mode towards the negative damping ratio, with K_{p2} having a comparatively higher effect on SUB mode than K_{p1} . On the other hand, the increase in Type C parameters increases the damping of SUP mode, but this increase is insignificant as compared to the respective deterioration of SUB mode.

Type D Parameters

The proportional parameter K_{p3} is found to be the most sensitive parameter for the infliction of SSCI. K_{p3} is the proportional parameters of the inner current controller of RSC. The value of K_{p3} is altered from 0 to 0.2 p.u. Although the variation is notably small, as compared to the variations made for other parameters, both the SUB and SUP modes show significant movement as a result of this variation. It can be seen in fig. 4.11 that the net change in the damping ratio of SUB mode is around 0.13 for the small change in K_{p3} . The behaviour of modes of interest in response to small alteration in K_{p3} implies that the SUB mode is very sensitive to

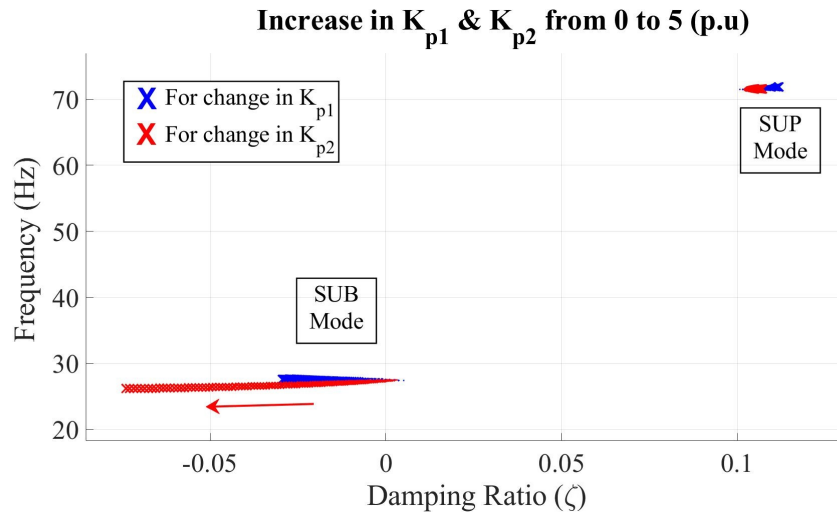


Figure 4.10: Effect of K_{p1} and K_{p2} on SUB and SUP modes.

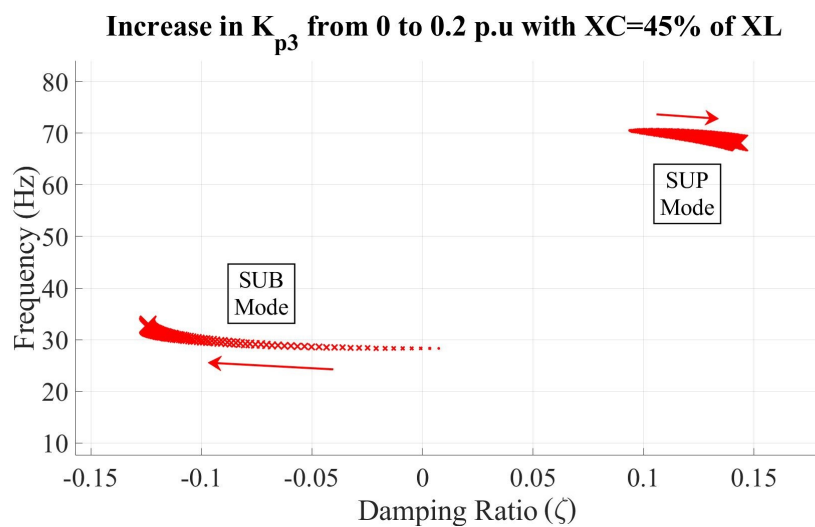


Figure 4.11: Effect of K_{p3} on SUB and SUP modes.

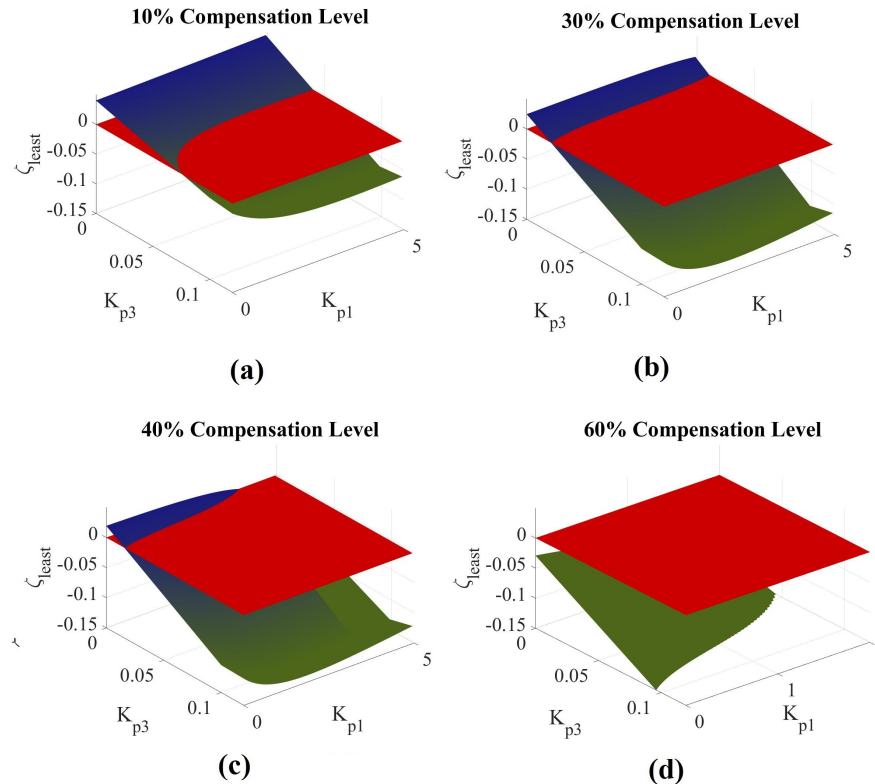


Figure 4.12: Range of parameters for different compensation levels.

this parameter. It is of great importance to chose the value of K_{p3} properly, so that the system can with stand the series compensation level as high as possible.

In order to keep the DFIG system stable until a certain limit of series compensation level, it is extremely important to tune the control parameters properly, especially type C and D parameters. Although, the proper tuning of control parameters can help the DFIG system to stay immune to SSCI, but based on the analysis, this immunity does not stand for the compensation level higher than a certain limit.

The effect of series compensation level on the range of two of the sensitive parameters, to which the system can remain stable, is shown in fig. 4.12. The range of K_{p1} and K_{p3} are evaluated for 10%, 30%, 40%, and 60% compensation level

separately. In fig. 4.12, the blue surface shows the area of the values of the parameters where the least damping ratio ζ_{least} of the system is positive and the system operates in stable region. The green surface shows the values of the parameters for which the system gets unstable. The red surface is for zero damping ratio which divides stable and unstable ranges.

It can be seen in fig. 4.12 that the stable range of the parameters gets smaller as the compensation level is increased. In fig. 4.12(c), the stable range of K_{p1} and K_{p3} is very small, but proper selection of the parameters can allow the system to operate stably. As the compensation level is increased to 60%, the system gets unstable for any simulated value of the parameters and it shows that the solution to mitigate SSCI through simulated range of control parameters is limited to certain level of series compensation.

4.1.5 Participation Factor

In previous section, the designed system was linearized and the eigenvalues of the system were calculated. After pointing out the eigenvalues corresponding to the modes of interest, i.e. SUB and SUP modes, for SSCI, there is a need to identify the state variables which play a role in making those modes stable or unstable. This can be done by determining the eigenvectors.

Eigenvector can be any non-zero vector V_i^r which satisfies

$$AV_i^r = \lambda_i V_i^r \quad (4.7)$$

or any non-zero vector V_i^l which satisfies

$$V_i^l A = V_i^l \lambda_i, \quad (4.8)$$

where V_i^r and V_i^l are the right and left eigenvectors, respectively. A is the state matrix of dimension $n \times n$. V_i^r is a column vector of order $n \times 1$ and V_i^l is a row vector of order $1 \times n$.

Although the activity of any state variable in a particular mode of the system might be determined by V_i^r , but the elements of this vector are dependent upon the dimensions and scaling of the state variables of the system, hence, making it difficult to measure the activity level based on the same standards. In order to identify

the activity level of all the state variables with a same measurement standard, the work in [70] presented a factor which has no dimensions and is named as participation factor p_{ki} .

Participation factor determines the strength of the contribution, of a particular state variable, in a specific mode of oscillation. The mathematical definition of participation factor can be given as

$$p_{ki} = V_{ik}^l V_{ki}^r \quad (4.9)$$

where V_{ik}^l is the element in k th column of the left eigenvector and V_{ik}^r is the element in the k th row of the right eigenvector of A , corresponding to the i th eigenvalue. The participation matrix can be determined as

$$P = \begin{bmatrix} p_{1,1} & p_{1,2} & \cdots & p_{1,n} \\ p_{2,1} & p_{2,2} & \cdots & p_{2,n} \\ \vdots & \vdots & \ddots & \vdots \\ p_{n,1} & p_{n,2} & \cdots & p_{n,n} \end{bmatrix}_{n \times n} \quad (4.10)$$

Having obtained the state matrix A already, the right and left eigenvectors are found using (4.7) and (4.8) and the participation matrix is found using (4.10).

The participation factors for the DFIG-based system are calculated. The tables below contains the participation factors of the state variables, with highest participation, corresponding to the SUB and SUP modes. These values are obtained from the eigenvalues of the system when the series compensation level of transmission line is set to 50%. The eigenvalues of SUB and SUP modes of both the systems are given before in Table 4.1.

Table 4.3: Participation Factors of DFIG System

State Variables	SUB Mode	SUP Mode
d -axis stator flux ψ_{ds}	0.26	0.19
q -axis rotor flux ψ_{qr}	0.12	0.02
Im -axis line current I_{Im}	0.19	0.18
R -axis series capacitor voltage U_{RC}	0.33	0.24
Im -axis series capacitor voltage U_{ImC}	0.22	0.29

From the calculated participation factors of the DFIG system, it can be noticed that the state variables corresponding to stator $\bar{\psi}_s$ and rotor fluxes $\bar{\psi}_r$, the current through the transmission line \bar{I} , and the voltage across the series compensation capacitor \bar{U}_C highly participate in generating the SSCI condition and in making the system prone to oscillations. Among all, the Re component of series capacitor voltage U_{RC} and the d component of stator flux ψ_{ds} have the significant contribution for making the SUB mode unstable. While, the SUP mode is vitally affected by the Re and Im component of series capacitor voltage. It is found that mechanical part of the turbine generator does not play any significant part in the interaction, as the participation factor related to drive train of the turbine has a negligible value (0.002 for SUB mode and 0.07×10^{-3} for SUP mode). This shows that the SSCI is purely an electrical phenomenon as the state variables which participates in making the SUB mode unstable do not represent any mechanical component.

The obtained participation factors show that beyond a certain level of compensation there occurs an interaction between the series compensation capacitor and the induction generator which generates a resonant condition. This resonant condition then propagates to the controllers of the VSC and amplifies the phenomenon. Up till now the components of the power system which contribute in the occurrence of SSCI are identified. Now it is important to explain the process of the infliction of SSCI. This investigation is done in the subsequent section.

4.2 Infliction of SSCI in DFIG-based Power System

In Section 4.1.5, the results obtained from the participation factors of the state variables corresponding to generator flux, transmission line current, and series capacitor voltage exhibited highest participation amongst the other states of the system. This implies the role of resonant current of the electrical network in the infliction of SSCI. However, the state variables corresponding the RSC and GSC controller did not show any significant participation towards the SUB and SUP modes. But, the sensitivity analysis of control parameters shows that the occurrence of SSCI greatly depends on the selection of control parameters of the converters, especially the proportional parameters of RSC, and that the slight change in values of these parameters can move the SUB and SUP modes significantly.

4.2.1 Internal Equivalent Resistance of Generator

Now a question arises here that since the state variables related to the converter controllers do not show appreciable participation in making the SUB mode unstable, would the DFIG system still fall under the SSCI condition if RSC controller is blocked?

In order to answer this question analytically, consider an equivalent circuit of an induction generator as seen from the stator terminal, for sub-synchronous frequency f_{ss} , shown in fig. 4.13. The figure shows that the resistance of the rotor can be mathematically expressed as R_r/s_{slip} , where

$$s_{slip} = \frac{f_{ss} - f_r}{f_{ss}}. \quad (4.11)$$

Generally the sub-synchronous frequency f_{ss} is lower than rotor frequency f_r , therefore the slip s_{slip} of the generator will be negative, which eventually makes the effective rotor resistance negative for the sub-synchronous currents in the system, as seen from the stator terminal.

There can be a case when the total resistance of stator and the external network is exceeded by the effective rotor resistance in magnitude, then the equivalent resistance of the generator, $R_G = Re\{Z_G(j\omega)\}$, would become negative. This negative equivalent resistance of the generator will lead to the self-excitation of the system, and this is exactly what happens in induction generator effect (IGE) [16].

IGE occurs in a series compensated network when the total resistance of the network becomes negative at a resonant frequency. This leads to undamped oscillation in the system that are self-sustained [71]. IGE is also a purely electrical phenomenon, like SSCI, and does not include the mechanical shaft of the turbine.

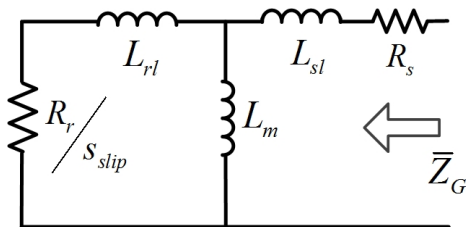


Figure 4.13: Equivalent circuit of induction generator.

Whenever there is any disturbance in the network, there will be a flow of sub-synchronous currents in generator's armature. These sub-synchronous currents create magnetic field that rotates slower than the generator's magnetic field [7].

Based on fig. 4.13, the equivalent resistance of the generator, as seen from stator terminal, can be derived in Laplace domain as

$$Z_G(s) = R_s + sL_{sl} + \left(\frac{R_r}{s_{slip}} + sL_{rl} \right) \parallel sL_m \quad (4.12)$$

$$Z_G(s) = R_s + sL_{sl} + \frac{s^2 L_{rl} L_m s_{slip} + sL_m R_r}{R_r + s_{slip}(sL_{rl} + sL_m)} \quad (4.13)$$

where $s = j\omega$ is the Laplace variable and is d/dt in time domain. In order to visualize the value of equivalent resistance R_G , as seen from the stator terminal, (4.13) is simulated for the set of frequencies from 0 to 50 Hz based on the values in Table 6.3. Fig 4.14 shows the equivalent resistance R_G against the sub-synchronous frequencies. It can be seen from the figure that at lower frequencies the equivalent resistance is positive. However, for the frequency above around 37 Hz, R_G starts to get negative, and hence appearing negative for the sub-synchronous currents of frequency 37 Hz and above.

By observing (4.12), it can be said that if the value of stator resistance R_s is increased then it will have positive impact on R_G . On the other hand, if the rotor resistance is increased, it will makes the effective rotor resistance R_r/s_{slip} more negative, and hence will decrease the equivalent generator resistance R_G , and consequently system will be prone to instability for comparatively lower sub-synchronous frequencies. This observation holds true when (4.13) is simulated for different values of R_s and R_r , as shown in fig. 4.15.

But, what effect does the real part of $Z_G(j\omega)$ has on the stability of the system? It has been already discussed and described in literature that when the effective rotor resistance exceeds the total of stator and network resistance, then the self-excitation of the electrical system occurs [7], [14], [16]. In essence, it means that the more negative value of R_G is, higher is the risk of it exceeding the stator and network resistance. And, when the negative value of R_G exceeds the other resistances of the system, then the instability occur at the resonant frequency. The result of the analysis shown in fig. 4.15 is then applied to the designed DFIG-based test system. It can be seen in fig. 4.16, that although with whole system's dynamics included, the increase in R_s increases the damping of SUB mode, hence eliminating

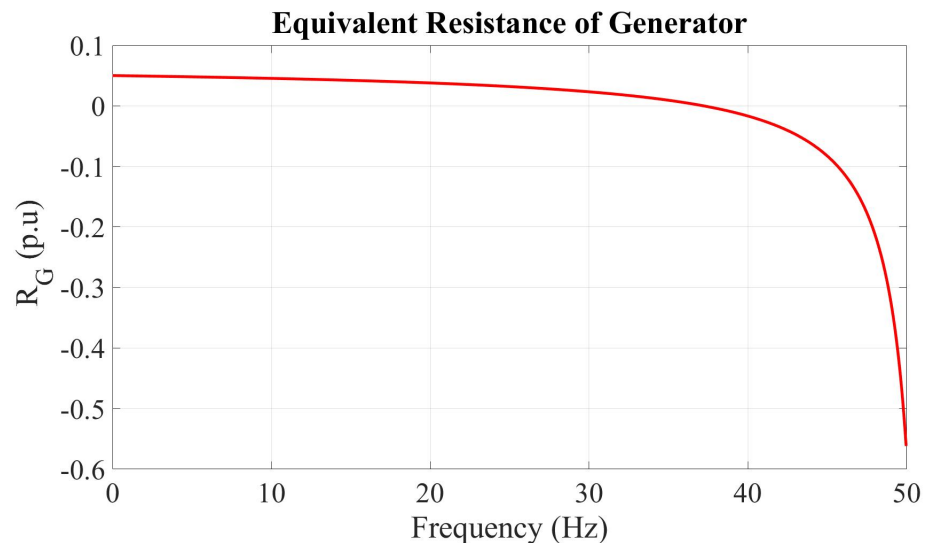


Figure 4.14: Equivalent resistance as seen from stator terminal.

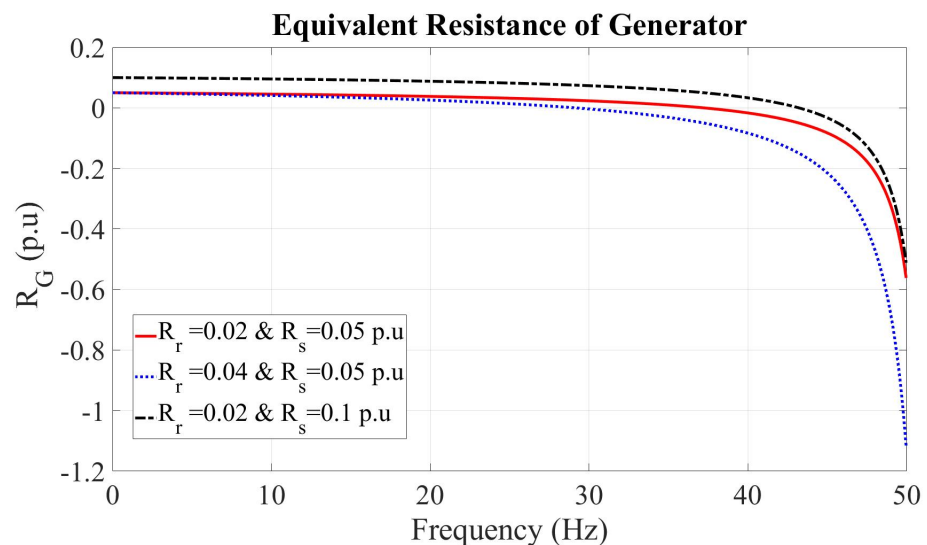


Figure 4.15: Equivalent resistance for different R_s and R_r .

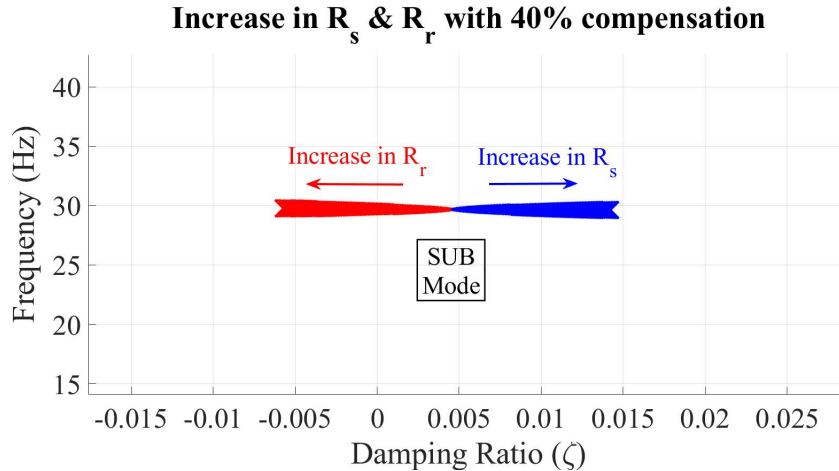


Figure 4.16: Effect of R_s and R_r on SUB mode of DFIG system.

the risk of SSCI. It is well in accordance with the result shown in fig. 4.15, because the increase in R_s increases R_G towards positive direction. However, the increase in R_r in fig. 4.16 pushes the SUB mode towards negative damping. This is because the increase in R_r makes R_G more negative, and hence exposes the system to the instability. In other research works, where the Nyquist stability criterion is used for the analysis of SSCI, same conclusion is drawn. It is shown that for higher negative R_G at sub-synchronous frequencies, as seen from stator terminal, the system gets unstable and the Nyquist plot of the open-loop system encircles -1 [52], [68], [72].

The plots in fig. 4.14 and fig. 4.15 only show the internal resistance of the generator. As discussed above, The instability will occur when the total equivalent resistance of the system, i.e., R_G combined with the resistance of the external network is negative, and when the total impedance of the system is zero. So, for the external network with resistance R_{ext} , inductance L_{ext} , and series capacitance C_{ext} , connected to the generator, (4.12) will become

$$Z_{tot}(s) = R_s + sL_{sl} + \left(\frac{R_r}{s_{slip}} + sL_{rl} \right) \parallel sL_m + R_{ext} + sL_{ext} + \frac{1}{sC_{ext}} \quad (4.14)$$

Looking at (4.14), it can be observed that the resistance of external network is adding up to the equivalent resistance of the system, hence enabling $R_{tot} = Re\{Z_{tot}(j\omega)\}$ to stay positive for even higher frequencies. For the system to show instability in this case, a very high level of series compensation is required for such

a high resonant frequency. That is why before last decade, IGE was never observed practically and was only considered as a possible academic problem [23]. However in the last decade, because of high penetration of wind turbines based on doubly-fed induction generators, there are some cases of IGE reported in literature [24], [25].

4.2.2 Effect of RSC on Internal Equivalent Resistance

Now to determine the effect of RSC controller on the internal equivalent resistance of the generator, first consider the equivalent circuit of the generator when RSC is connected to it, as shown in fig. 4.17.

From fig. 4.17, it can be observed that as compared to the circuit in fig. 4.13, there will be some additional components in the circuit of induction generator as seen from the stator terminal. In fig. 4.17, the T-model of induction generator is considered. In order to simplify the study and make the derivation of control law easier, all the leakage inductances can be shifted to rotor side [73], this model is known as Γ -model, and is shown in fig. 4.18. While transforming from T-model to Γ -model, some new variables are introduced and the relation between the new variables is given as follows [74]

$$\begin{aligned}\gamma &= \frac{L_{ss}}{L_m}, \quad \bar{V}_R = \gamma \bar{V}_r, \quad \bar{I}_R = \frac{\bar{I}_r}{\gamma} \\ L_M &= \gamma L_m, \quad \bar{\psi}_R = \gamma \bar{\psi}_r, \quad R_R = \gamma^2 R_r \\ L_R &= \gamma L_{sl} + \gamma^2 L_{rl}.\end{aligned}\tag{4.15}$$

From fig. 4.18, based on Γ -model of induction generator, the rotor voltage \bar{V}_R can be given as

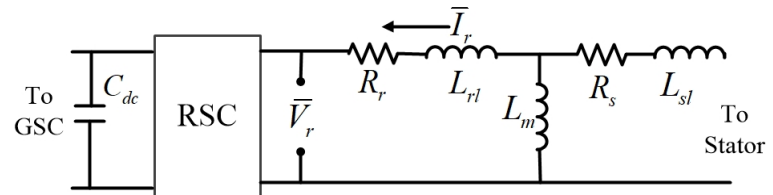
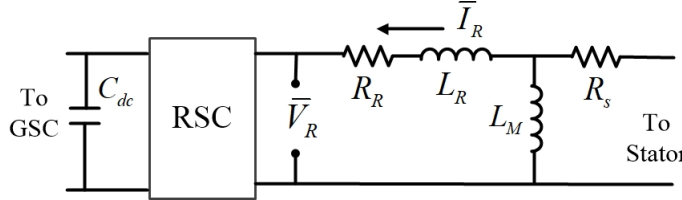


Figure 4.17: Equivalent circuit of generator with RSC.

Figure 4.18: Equivalent Γ model.

$$\bar{V}_R = -R_R \bar{I}_R - L_R \dot{\bar{I}}_R - i\omega_{sr} L_R \bar{I}_R + \underbrace{\dot{\psi}_s + i\omega_{sr} \psi_s}_{emf} \quad (4.16)$$

Decomposing \bar{V}_R into its d and q components, and rearranging the above equation to find \dot{I}_{dR} and \dot{I}_{qR}

$$\begin{aligned} L_R \dot{I}_{dR} &= -V_{dR} - R_R I_{dR} + \omega_{sr} L_R I_{qR} + emf_d \\ L_R \dot{I}_{qR} &= -V_{qR} - R_R I_{qR} - \omega_{sr} L_R I_{dR} + emf_q \end{aligned} \quad (4.17)$$

With cross-coupling effect of d and q axes and the perfect estimation of emf, the equation set (4.17) becomes

$$\begin{aligned} L_R \dot{I}_{dR} &= -V_{dR} - R_R I_{dR} \\ L_R \dot{I}_{qR} &= -V_{qR} - R_R I_{qR} \end{aligned} \quad (4.18)$$

which becomes

$$L_R \dot{\bar{I}}_R = -\bar{V}_R - R_R \bar{I}_R \quad (4.19)$$

where $\bar{I}_R = I_{dR} + jI_{qR}$ and $\bar{V}_R = V_{dR} + jV_{qR}$. In Laplace domain, the equivalent expression of (4.19) will become [52], [68],

$$\bar{I}_R(s) = -\frac{1}{sL_R + R_R} \bar{V}_R(s) \quad (4.20)$$

$$\bar{I}_R(s) = G_R(s) \bar{V}_R(s) \quad (4.21)$$

The minus sign in (4.20) is because of the direction of current that is considered to be flowing towards the converter. Based on RSC controllers, there is a need to derive the relation between $\bar{V}_R(s)$ and $\bar{I}_R(s)$. For simplicity, the outer-loop power controllers are ignored here, only the inner-loop current controller are considered. The block diagram of inner-loop current controller of RSC is shown in fig. 4.19.

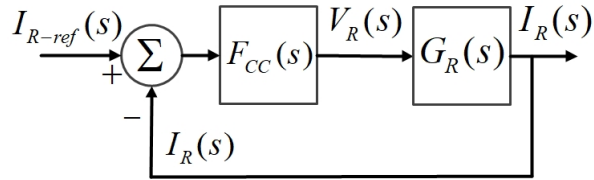


Figure 4.19: Inner current control loop of RSC.

In correlation with (4.21), the transfer function $G_R(s)$ represents the rotor circuit of induction generator that gives $\bar{I}_R(s)$ based on $\bar{V}_R(s)$. The input output relationship of the RSC inner current control loop can be found as

$$\bar{I}_R(s) = G_R(s)F_{CC}(s)(\bar{I}_{R-ref}(s) - \bar{I}_R(s)) \quad (4.22)$$

$$\bar{I}_R(s) = \frac{1}{sL_R + R_R}F_{CC}(s)(\bar{I}_R(s) - \bar{I}_{R-ref}(s)). \quad (4.23)$$

Again, in (4.23), the sign of $\bar{I}_{R-ref}(s)$ is negative and $\bar{I}_R(s)$ is positive because of the direction of rotor current. Solving (4.22) for $\bar{I}_R(s)$

$$\bar{I}_R(s) = \frac{G_R(s)F_{CC}(s)}{1 + G_R(s)F_{CC}(s)}\bar{I}_{R-ref}(s). \quad (4.24)$$

According to the Internal Mode Control (IMC), the closed looped system in (4.24) can be represented as a first order low pass filter [75],

$$\frac{G_R(s)F_{CC}(s)}{1 + G_R(s)F_{CC}(s)} = \frac{\alpha_{CC}/s}{1 + \alpha_{CC}/s} \quad (4.25)$$

$$\implies G_R(s)F_{CC}(s) = \alpha_{CC}/s \quad (4.26)$$

$$F_{CC}(s) = \frac{\alpha_{CC}}{s} G_R^{-1}(s) = \frac{\alpha_{CC}}{s} (sL_R + R_R) \quad (4.27)$$

$$= \alpha_{CC} L_R + \frac{\alpha_{CC} R_R}{s} = K_{p3} + \frac{K_{i3}}{s} \quad (4.28)$$

where α_{CC} is the bandwidth.

From (4.28), it is clear that the transfer function $F_{CC}(s)$ is a proportional-integral (PI) controller, which has K_{p3} and K_{i3} parameters, that gives the reference value of rotor voltage by controlling the rotor current. So, based on $F_{CC}(s)$ the relation between the rotor voltage and rotor current can be written as

$$\bar{V}_R(s) = \left(K_{p3} + \frac{K_{i3}}{s} \right) (\bar{I}_R(s) - \bar{I}_{R-ref}(s)) \quad (4.29)$$

$$\bar{V}_R(s) = \overbrace{\left(K_{p3} + \frac{K_{i3}}{s} \right) \bar{I}_R(s)}^{\text{RSC Impedance}} - \overbrace{\left(K_{p3} + \frac{K_{i3}}{s} \right) \bar{I}_{R-ref}(s)}^{\text{RSC Voltage}} \quad (4.30)$$

From (4.30), it can be comprehended that the rotor voltage \bar{V}_R that is obtained from RSC current controller can be expressed in terms of a voltage source ($\bar{V}_{RSC-\Gamma}(s)$) with an impedance ($Z_{RSC-\Gamma}(s)$). Therefore, by adding the deduced model of RSC controller in to the equivalent circuit of induction generator in fig. 4.13, there will be an additional voltage source and an impedance. The new equivalent circuit of induction generator with RSC in time domain is shown in fig. 4.20.

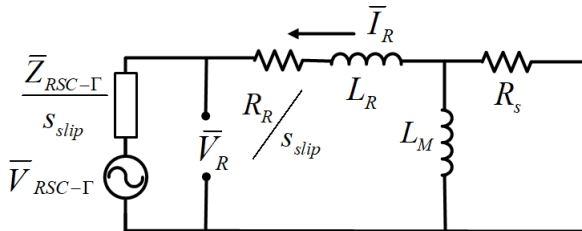


Figure 4.20: RSC in equivalent circuit of induction generator.

To find the equivalent impedance of the generator with RSC $Z_{G-RSC-\Gamma}(s)$, as seen from the stator terminal, the voltage source $\bar{V}_{RSC-\Gamma}(s)$ will become short circuit, and the equivalent circuit will become as shown in fig. 4.21. Based on the figure, $Z_{G-RSC-\Gamma}(s)$ can be calculated as

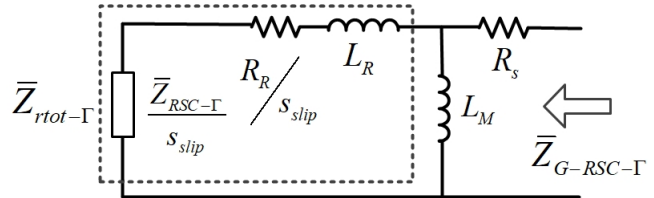


Figure 4.21: Equivalent impedance of generator with RSC.

$$Z_{G-RSC-\Gamma}(s) = R_s + \left(Z_{rtot-\Gamma}(s) || sL_M \right) \quad (4.31)$$

where

$$Z_{rtot-\Gamma}(s) = \frac{R_R}{s_{slip}} + sL_R + \frac{K_{p3} + \frac{K_{i3}}{s}}{s_{slip}} \quad (4.32)$$

$$Z_{rtot-\Gamma}(s) = \underbrace{\frac{R_R + K_{p3}}{s_{slip}}}_{\text{Resistance}} + sL_R + \underbrace{\frac{\frac{K_{i3}}{s}}{s_{slip}}}_{\text{Reactance}} \quad (4.33)$$

With T-model of Induction Generator

The analytical expression in (4.31) may also be derived based on T-model of synchronous generator. In order to do so, remove the time normalization in (3.31), after assuming perfect emf estimation and decoupling, and rearrange for the rotor current I_r

$$\dot{\bar{I}}_r = \frac{L_{ss}}{\sigma} (\bar{V}_r + R_r \bar{I}_r) \quad (4.34)$$

In Laplace domain, (4.34) becomes

$$\left(\frac{\sigma}{L_{ss}} \right) s \bar{I}_r(s) - R_r \bar{I}_r(s) = \bar{V}_r(s) \quad (4.35)$$

$$- \left(\frac{L_{ss} L_{rr} - L_m^2}{L_{ss}} \right) s \bar{I}_r(s) - R_r \bar{I}_r(s) = \bar{V}_r(s) \quad (4.36)$$

$$\bar{I}_r(s) = -\frac{\bar{V}_r(s)}{sL_{Rl} + R_R} \quad (4.37)$$

Here, a new inductance term $L_{Rl} = \frac{L_{ss}L_{rr}-L_m^2}{L_{ss}}$ is introduced. The above equation looks similar to (4.20), and based on the T-model of induction generator, (4.28) and (4.30) will become

$$F_{CC}(s) = \alpha_{CC}L_{Rl} + \frac{\alpha_{CC}R_r}{s} = K_{p3} + \frac{K_{i3}}{s} \quad (4.38)$$

$$\bar{V}_r(s) = \overbrace{\left(K_{p3} + \frac{K_{i3}}{s}\right)\bar{I}_r(s)}^{\text{RSC Impedance}} - \overbrace{\left(K_{p3} + \frac{K_{i3}}{s}\right)\bar{I}_{r-ref}(s)}^{\text{RSC Voltage}}, \quad (4.39)$$

and the equivalent impedance circuit of the generator, in time domain, as seen from the stator terminal will become as shown in fig. 4.22.

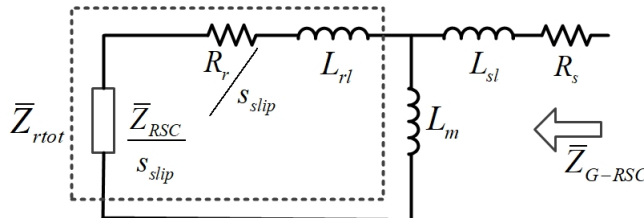


Figure 4.22: Equivalent impedance of generator with RSC using T-model.

Moreover the for the impedance of generator for T-model $Z_{G-RSC}(s)$ can be calculated as,

$$Z_{G-RSC}(s) = R_s + sL_{sl} + \left(Z_{rtot}(s) \parallel sL_M\right) \quad (4.40)$$

Equations (4.33) and (4.40) both show that the total impedance of the rotor, along with RSC, consists of a resistance and a reactance. The resistive part of $Z_{rtot}(s)$ contains the proportional parameter K_{p3} in it. It means that K_{p3} is adding up to the rotor resistance R_R , making the whole resistive term more negative, as it contains the s_{slip} as well. It can be said that for higher values of K_{p3} , the system

may become unstable for lower sub-synchronous frequencies, as compared to the system with lower or with no K_{p3} . In order to verify this claim, the real part of the system given in (4.40) is simulated for all the sub-synchronous frequencies, for different values of K_{p3} . The result is shown in fig. 4.23.

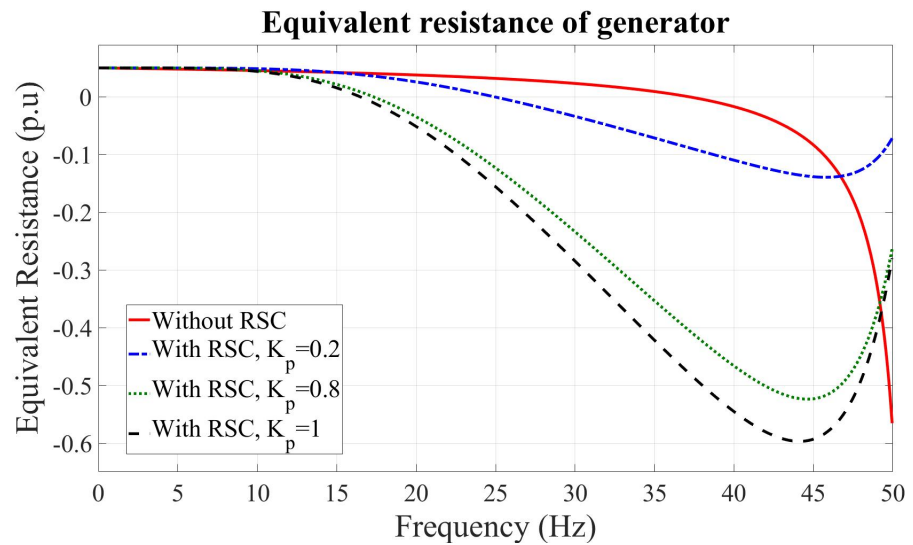


Figure 4.23: Equivalent resistance of generator with RSC.

The figure shows that when the RSC is added in to the generator's equivalent circuit, the equivalent resistance gets more negative for lower frequencies as compared to the resistance of generator with out RSC. It can be seen that when there is no RSC, the resistance gets negative after around 37 Hz, however, even for a small value of K_{p3} the generator with RSC shows negative resistance after around 25 Hz. This threshold frequency for negative equivalent resistance decreases with the increase in K_{p3} . Moreover, with the increase in K_{p3} , the magnitude of the resistance also increase in negative, hence, pushing the system higher towards instability.

The result shown in fig. 4.23 is completely in accordance with that of eigenvalue sensitivity analysis obtained while investigating the effect of K_{p3} in Section 4.1.4. The sub-synchronous (SUB) mode moves higher towards instability with the increase value of K_{p3} , as shown in fig. 4.11. Moreover, The effect of the value of K_{p3} on the equivalent resistance is similar to the conclusion made in studies where the outer power loop of RSC controller is also considered [54].

Fig. 4.23 also explains the difference between IGE and SSCI. For the generator without RSC, the system is prone to instability, or IGE, for much higher frequency. To have the resonant current of such high frequency, a very high series compensation level is required. However, the system with RSC can become unstable because of SSCI for comparatively lower frequencies, and the resonant current of such lower frequencies can be obtained with low compensation levels, that is why in actual there are many reported event of SSCI. Based on the obtained results, it is evident that IGE and SSCI are closely related, and SSCI is basically an aggravated form of IGE because of the presence of RSC.

In order to see the effect of RSC on the stability of DFIG based system and the difference in the behaviour of modes of interest of the system with and without RSC, the eigenvalue sensitivity analysis is carried out for different compensation levels. The proportional parameter K_{p3} is kept as low as 0.001 p.u., and the series compensation level is changed from 35% to 90%, as shown in fig. 4.24.

The simulation results show that the two systems with everything same, except for RSC, show tremendously different behaviours when exposed to different levels of series compensation. In the system with RSC, the SUB mode moves towards negative damping ratio with the increase in compensation level, and gets unstable

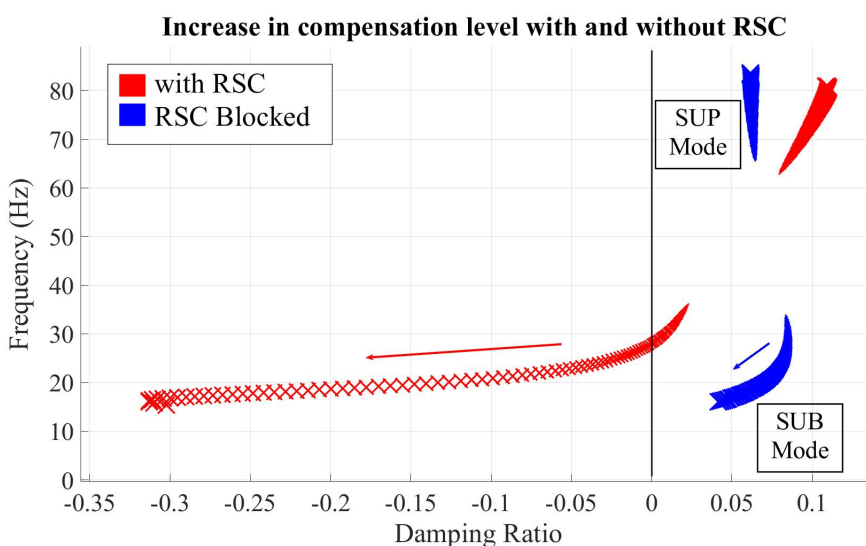


Figure 4.24: Influence of RSC on modes of interest.

for higher levels. On the other hand, in the system with blocked RSC, the SUB mode moves towards left side with the increasing compensation level, but remains stable even at 90% compensation. It means that SSCI is dependent on the presence of and on the parameters of RSC controller, and its absence will not inflict the SSCI condition in the DFIG system.

4.2.3 Explanation of infliction of SSCI

It is shown analytically in Section 4.2.2 that the inner current control loops of DFIG converters adds up to the negative internal resistance of the induction generator. The external grid sees the negative resistance of the generator, which gets more negative based on the parameters of RSC controller. If negative internal resistance exceeds the total resistance of the system, when the total impedance of the system is zero, then the DFIG system falls in a resonant condition with the series-compensated line.

Moreover, the obtained high participation factors of generator flux, transmission line current, and series capacitor voltage imply the role of resonant current of the electrical network in the infliction of SSCI. During the disturbance the system, the resonant currents of sub-synchronous frequency come into existences in the series-compensated transmission line. These resonant currents cause distortion in the active and reactive powers of stator, which are being controlled by the rotor-side converter. These distortions are reflected in the reference values of rotor current that are further used in the inner-loop current controllers, hence the reference current which the controllers need to track are also distorted.

On the other hand, the currents of sub-synchronous frequency are also generated in rotor winding by the magnetic fields induced by the sub-synchronous currents of the stator. These distorted rotor currents are then processed as the information through the turbine controller and are compared with the distorted reference rotor current. This enables the RSC controllers to track the distorted signal to the distorted reference, and form the reference voltage for rotor. The output of VSC imposes the voltage, based on distorted information, on the rotor windings and consequently a cycle is formed which causes the instability in the system, as also explained mathematically in [29].

The participation factors show that generator flux, line current, and series capacitor voltage participates in the phenomenon, while the state variables related to RSC controllers do not exhibit high participation factors. However, the result in

fig. 4.24 shows that the presence of RSC is essential to inflict SSCI in the system. This means that RSC does not interact itself, but it just enables the exchange of energy between the generator and series compensated capacitor by making the internal equivalent resistance negative and by providing a closed loop.

Based on the results from previous sections, participation factors and from the parameter sensitivity analysis, SSCI can be described as a condition of the DFIG system, which is sensitive to the controller parameters and is enabled by the converter controller, in which the exchange of energy happens between the generator and the series compensation capacitor through the currents of sub-synchronous frequencies.

Chapter 5

Mitigation of SSCI in DFIG-based Power System

This chapter deals with the techniques for the mitigation of SSCI from the DFIG system. Two techniques are analyzed here. The first technique eliminates the SSCI condition from the system through a proper tuning of sensitive control parameters, while the second technique uses a supplementary control signal in the VSC controller to damp the oscillations. The details of the designs of the techniques and the corresponding results are presented in this chapter.

5.1 Mitigation through Control Parameters Tuning

As shown in Chapter 4, through eigenvalue analysis, that the modes of interest of the DFIG-based system are sensitive to converter control parameters, and the modes may get stable or unstable based on the values of parameters. In this section the dependency of stability of DFIG system on control parameters is investigated and the SSCI is mitigated through proper tuning of control parameters. The theoretically obtained results are also validated experimentally.

5.1.1 The Boomerang Effect of K_{p3}

As described in Section 4.1.4, the proportional parameters of the inner current controller of RSC is found to be the parameter with the most significant effect on the modes of interest of the DFIG system. It is observed that the SUB mode deteriorates when the values of K_{p3} increased. This effect is also explained analytically

in Section 4.2.2. It is shown that the increase in K_{p3} plays a role in increasing the negative resistance of the induction generator, as seen from stator terminal. Hence, making the system prone to the risk of SSCI. In both the sections and also in other research work [43], [47], [52], [79], and [80], similar results are observed for the effect of proportional parameter of inner current controller of RSC. It is found that the increase in the proportional parameter affects the sub-synchronous mode significantly and inflicts the SSCI condition in the system. It is concluded in all the mentioned research work that the value of this parameter should be kept as low as possible to keep the system away from the risk of SSCI, up to a certain level of series compensation. However, it is pertinent to mention that in all the cited research, along with Section 4.1.4 and Section 4.2.2 of this thesis, the investigation is carried out by increasing the value of proportional parameter to the maximum value of 1 p.u. or lesser.

But, what will happen if the value of the proportional parameter is increased beyond 1 p.u.? Would it keep on pushing the SUB mode towards negative damping ratio? And, would it continue to increase the negative equivalent resistance of the generator? To answer this question, again consider the expression of the equivalent internal impedance of an induction generator given by (4.40), which is derived in Section 4.2.2. Previously, the real part of $\bar{Z}_{G-RSC}(j\omega)$ was simulated for a range of frequencies for different K_{p3} , with the maximum value of 1 p.u. Now again, it is simulated for same range of frequencies but with higher value of K_{p3} , as shown in fig. 5.1.

It can be seen in fig. 5.1 that the increase in K_{p3} from 0.2 to 2 p.u. exhibits a major decrease in the effective resistance of the generator, as seen from the stator. This increase in the risk towards SSCI is same as observed before. However, when K_{p3} is increased further to 4 p.u., the effective resistance becomes less negative than it was at $K_{p3}=2$ p.u. When K_{p3} is increased further, it affects the effective resistance in an opposite way, i.e., the effective resistance increases toward positive direction. There comes a value of K_{p3} , in this case at 60 p.u, when the internal resistance, as seen from the stator, is not negative at all for any sub-synchronous frequency. This effect is named as boomerang effect of K_{p3} . It is named boomerang because of its characteristic of going first towards instability with the increasing K_{p3} and then going back towards the stability. It seems that K_{p3} was considered to be the one of the main reason for exposing the system to SSCI, but after observing the boomerang effect, K_{p3} is the parameter that can make the system immune to SSCI if its value is chosen properly.

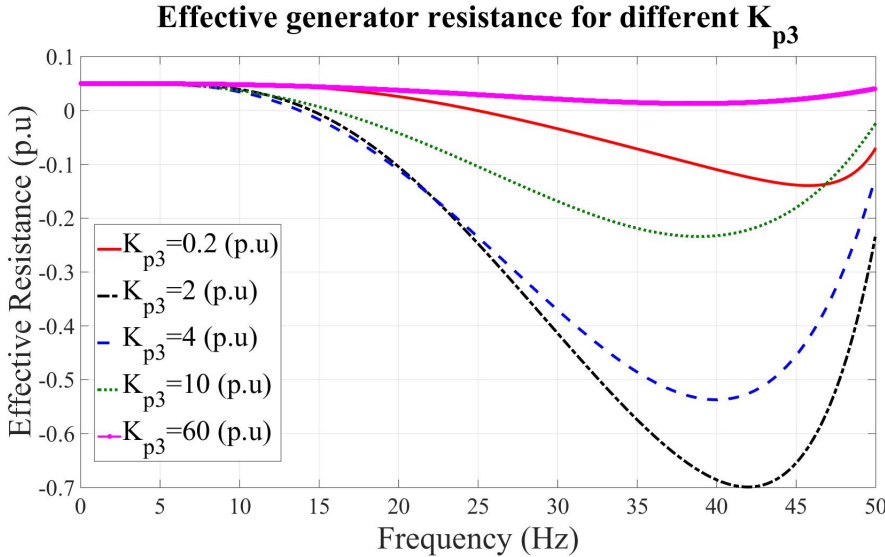


Figure 5.1: Equivalent resistance of generator with different K_{p3} .

Since, it is shown analytically that the value of K_{p3} higher than a specific value can bring the system back to stability and can avoid the undamped oscillation, so both linear and non-linear simulations are carried out to study the effect of higher values of K_{p3} in details. It must be noted that in the simulation based on analytical expression, as shown in fig. 5.1, the positive effective resistance of generator is achieved for a very high value of K_{p3} , which appears to be very unreasonable for an inner current controller of RSC. However, it will be shown in subsequent sections that the positive effective resistance is achieved with much lesser values of K_{p3} in the designed and in experimental DFIG system. This is because in the analytical studies the non-linearities of the outer loop power controllers are ignored and also the external network is not considered.

5.1.2 Results of Linearized DFIG System

The DFIG system is linearized and the eigenvalue analysis is performed to observe the boomerang effect of K_{p3} on the SUB and SUP modes of the system. Previously in Section 4.1.4, it was observed in fig. 4.11 that the SUB mode moves towards the negative damping ratio aggressively even with a small change in K_{p3} from 0 to 0.2 p.u. However, now the sensitivity analysis is performed by increasing K_{p3} from 0

to 6 p.u., as shown in fig. 5.2.

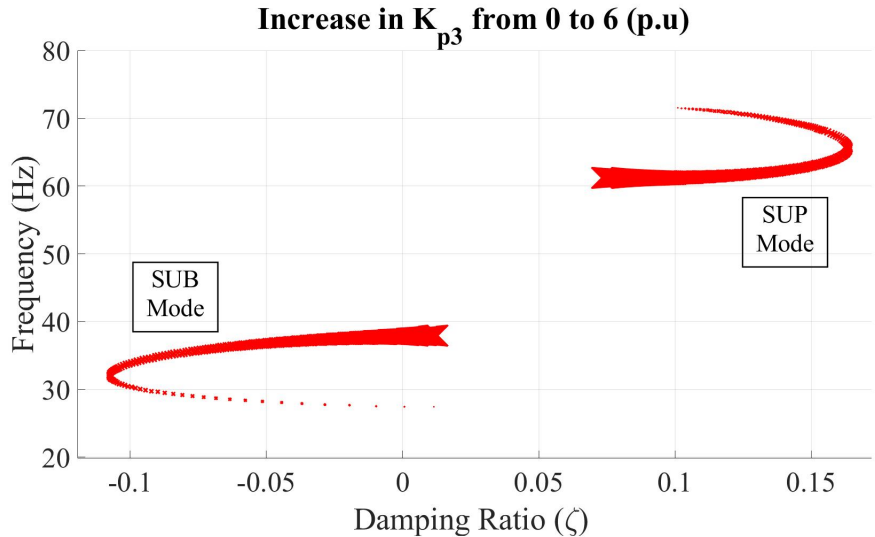


Figure 5.2: Effect of higher K_{p3} on SUB and SUP modes.

The boomerang effect of K_{p3} can be seen in fig. 5.2. As K_{p3} is increased from 0 p.u., the SUB mode starts to move accordingly towards the left half plane and gets unstable. However, there comes a point when, for higher values of K_{p3} , the SUB turns its direction back to positive damping ratio. This movement continues until a value of K_{p3} to which SUB mode has positive damping ratio and the system is no longer exposed to the SSCI condition. On the other hand, the SUP mode shows a movement opposite to SUB mode for different values of K_{p3} . It first starts to increase its damping ratio but then because of the boomerang effect the damping ratio decreases. However, even for the highest simulated value of K_{p3} , both the SUB and SUP modes are stable, and hence the SSCI is mitigated from the DFIG system.

To find the exact values of K_{p3} at which the system gets stable and unstable, the root locus of the system and open-loop Bode plot is shown in fig. 5.26. The root locus plot also shows the similar effect of K_{p3} as in previous figure. When K_{p3} is increased beyond 0.007 p.u., the SUB mode gets unstable inflicting the SSCI in the system. The system remains exposed to SSCI condition until $K_{p3} = 1.59$ p.u. Once the K_{p3} is increased further, the SUB mode gets negative real part and introduces

damping to the oscillation of sub-synchronous frequencies. On the other hand, the open-loop Bode plot shows that when the value of K_{p3} is between 0.007 and 1.59 p.u., the phase margin is negative below -180° which makes the loop unstable.

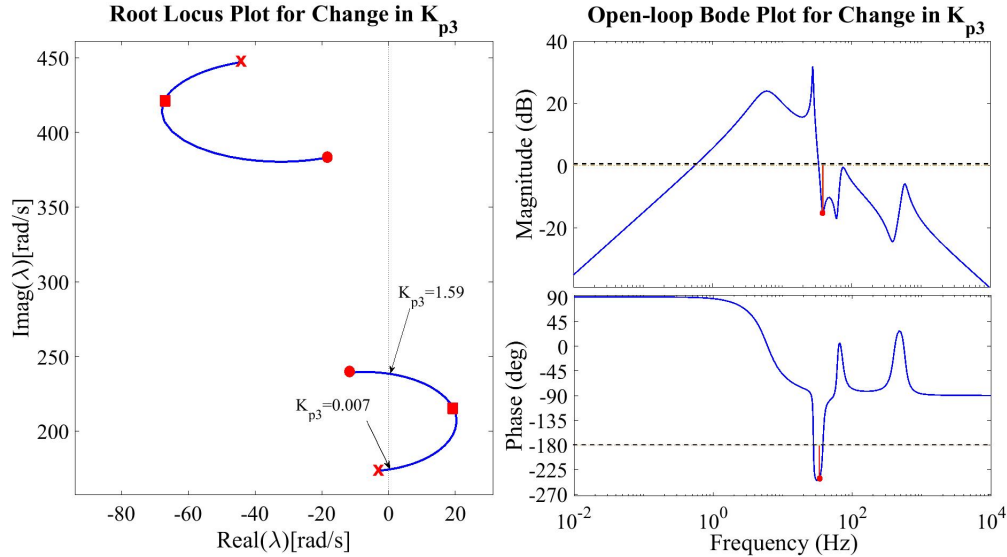


Figure 5.3: Root-locus and open-loop Bode plot for change in K_{p3} .

Optimum Value of K_{p3}

The improvement in the damping of SUB mode with the increase in K_{p3} deteriorates the damping of SUP mode. There might be a possibility that the increase in K_{p3} also deteriorate other modes of the system to the point of making them unstable. Therefore, it is needed to investigate the least damping ration of the system and to see the effect of proportional parameters on the least damped mode of the system. Since, the proportional parameters of RSC outer loop controller were also found to have an impact on the stability of SUB mode, the linearized system is simulated for different values of K_{p1} and K_{p3} to find the range of values where the system can stay immune to SSCI, for different compensation levels. The plot in fig. 5.4 shows that ranges of the proportional parameters where the system may or may not stay stable, based on the least damped mode ζ_{least} of the system. It can be seen that even for compensation level as high as 90%, there is still a range

of proportional parameters where the system can avoid the occurrence of SSCI. For the lower compensation levels, there is a very small range of lower values of K_{p3} where the system can stay stable, this is the range of K_{p3} that is used in cited research work to avoid SSCI for lower compensation levels.

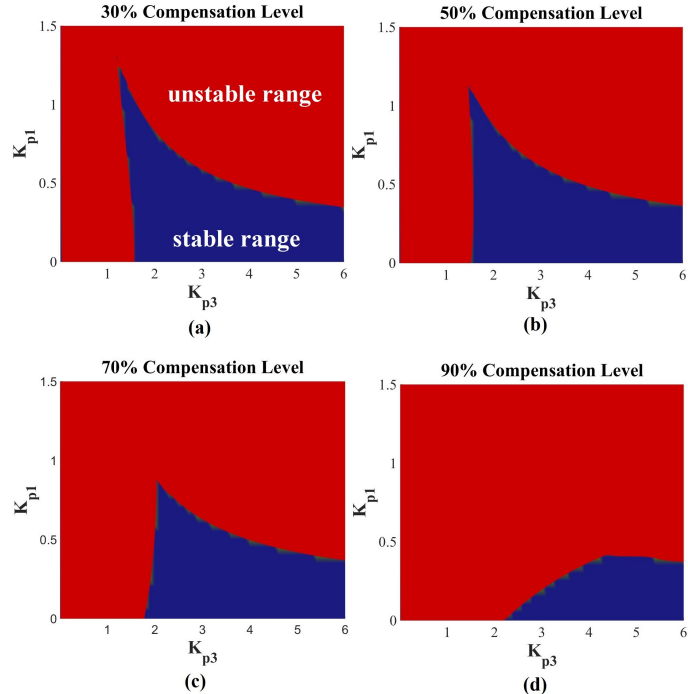


Figure 5.4: Range of sensitive parameters for different compensation.

In order to find the optimal value of K_{p3} , it should be noted that the main objective here is to keep the damping ratio of least damped mode ζ_{least} of the system to the maximum value, especially the damping ratio of SUB mode which is responsible for making the system prone to sub-synchronous oscillations. Since it has been shown that change in K_{p3} affects the damping ratio of SUB mode the most, so for any set of values of other control parameters, the K_{p3} should be selected higher than the value where it passes the boomerang phase and the damping ratio of SUB mode gets back to positive. In fig. 5.4, only the stability region of ζ_{least} is shown, but still there is a need to find the value of K_{p3} where the system can exhibit the maximum damping of ζ_{least} . To find this, a 3D plot is shown in fig. 5.5, with

ζ_{least} along the z -axis.

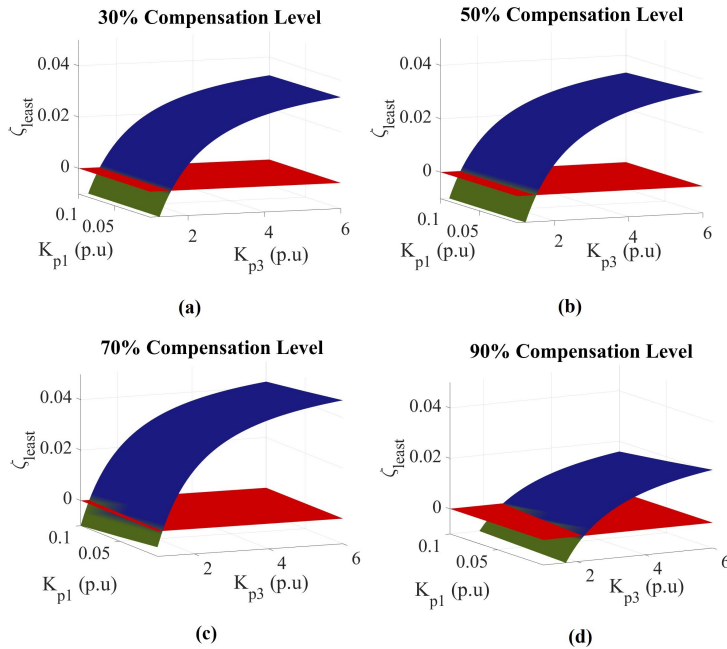


Figure 5.5: Value of K_{p3} for highest damping.

It can be seen from fig. 5.5 that for all the simulated series compensation levels, the maximum damping of ζ_{least} is achieved by keeping K_{p1} to minimum and K_{p3} to the maximum, in this case 6 p.u. K_{p3} has appreciable effect on damping ratio of ζ_{least} . The higher the K_{p3} , the higher will be the damping ratio of least damped mode.

By looking at the plots in fig. 5.4 and fig. 5.5, it can be said that K_{p3} should be kept as high as possible to achieve the maximum damping of the least damped mode. On the lower side, K_{p3} should be kept at least around 2.5 p.u. to make the DFIG system immune to SSCI, for any realistic series compensation level. However, in normal operation of DFIG, and in the literature showing the modeling of DFIG, the proportional parameters of current controller are kept very low, or lesser than 0.5 p.u. It raises a question about the safety and health of the converter if the proportional parameters are kept to a comparatively higher value.

This issue can be addressed by the recommendation for the bandwidth of current controller in [19] and [75]. It is reported that a higher bandwidth of current control loop α_{CC} , as given in (4.28), can be selected if the converter has a high angular switching frequency ω_{sw} . Based on the recommendation in the cited work, the bandwidth can be set either lesser or equal to $0.2\omega_{sw}$, i.e., $\alpha_{CC} \leq 0.2\omega_{sw}$. For the experimental setup used in this research work, the switching frequency of the power electronic converter is 5 kHz. For 5 kHz switching frequency the angular switching frequency will be $\omega_{sw} = \frac{2\pi 5000}{\omega_o} = 100$ p.u.. Based on the recommendations

$$\begin{aligned}\alpha_{CC} &\leq 0.2\omega_{sw} \\ \alpha_{CC} &\leq 20(\text{p.u.}) \\ \implies K_{p3} &\leq 20L_{RI}(\text{p.u.}).\end{aligned}\tag{5.1}$$

Usually, there are different values for the leakage and magnetizing inductances for different rating of the generators. For generator less than 100 kW, the typical value of inductance L_{RI} is calculated to be approximately 0.35 p.u. [81]. For the parameters of the actual generator used in experimental validation, $L_{RI} \approx 0.2$ p.u. Therefore, it would be recommended to keep $K_{p3} \leq 4$ p.u.. Based on the analysis shown in fig. 5.4, keeping K_{p3} between 2.5 and 4 p.u. can keep the system safe and free of the risk of SSCI, even for 90% compensation level.

Using the value of $K_{p3} = 4$ p.u. is well justified based on the recommendations, and the results for the linearized system show that the system will be immune to SSCI for this value. It is important to study the behaviour of current controller for this value of K_{p3} , because with high K_{p3} , there might be an issue about the performance of DFIG system under normal conditions of lesser or no series compensation. The DFIG system is tested under different circumstances with $K_{p3}=4$ p.u., and for all the circumstances, the system performs very well. One of the example is shown in fig. 5.6. It can be seen that when there is no series compensation in the system, the controllers of RSC successfully track the references when K_{p3} is set to 4 p.u.

5.1.3 Simulation of DFIG System

The mitigation of SSCI in DFIG system, through proper selection of control parameters, is also validated through the simulation of non-linear system in MATLAB and Simulink platform. The system is simulated for different values of K_{p3}

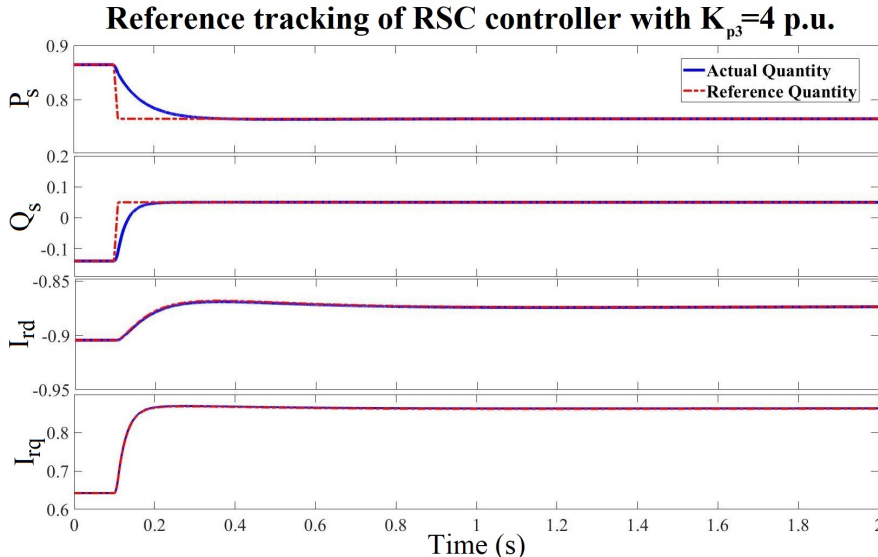


Figure 5.6: Reference tracking of RSC controller for $K_{p3}=4$ p.u.

and for different compensation levels. The result of the non-linear simulation is shown in fig. 5.7.

At first K_{p3} is set to 0.004 p.u., based on the result of linearized system, this K_{p3} should keep the system stable for lower compensation levels. The figure shows the system is stable at the start at 30% compensation. At 0.1 s, there is a change in compensation level from 30% to 45%. The system gets back to stability after the disturbance, since the damping ratio of SUB mode below 50% compensation is positive. However, when the compensation level is increased to 65% at 1.5 s, the undamped oscillations are observed in the system because the SUB mode has moved towards the negative damping ratio. These growing oscillations are aggravated when the compensation level is further increased to 85%.

On the other hand, when K_{p3} is set to 4 p.u., the system remains stable for all the simulated compensation levels. It not only keeps the system immune to SSCI, but also manages to keep the system operation smooth even after large disturbances of 20% change in the compensation level. This result shows that just by carefully selecting K_{p3} and by using its boomerang effect as an advantage, the SSCI condition can be mitigated from DFIG based power system with out using any additional

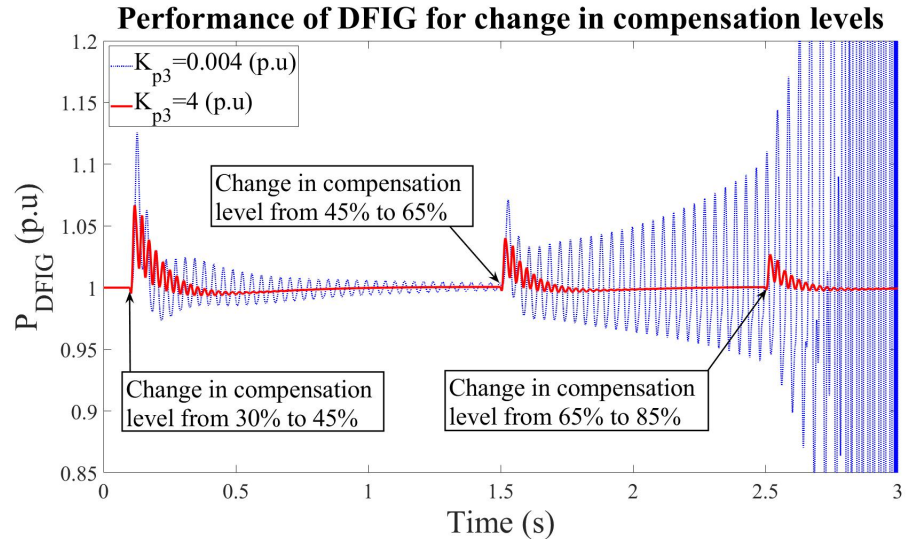


Figure 5.7: Simulation of DFIG system with different K_{p3} .

device or supplementary control.

To observe the boomerang effect of K_{p3} on DFIG system, the system is simulated while gradually increasing K_{p3} from 0.004 p.u. onwards, as shown in fig. 5.8.

It can be seen that initially the system is stable at 30% compensation level, but there are oscillations in the system when the level is changed to 45%. From 0.5 s onwards, the value of K_{p3} is gradually increased, and it can be seen that at first the oscillations started to grow, but as K_{p3} crossed 2 p.u., the oscillations start to damp, and with further increase in K_{p3} the damping also increased, and the system gets back to the stability. This behaviour of the system is well in accordance with the results obtained from the linearized system as shown in fig. 5.2.

Although the justification of a higher gain of K_{p3} is explained in Section 5.1.2, but in any cases there might be the need of using lower value K_{p3} for the normal operation of DFIG. For such case, it is needed to observe the effect of change in K_{p3} to a higher value in runtime, after a disturbance occurred in a system that leads to the infliction of SSCI. The result of simulation based on such a case is shown in fig. 5.9.

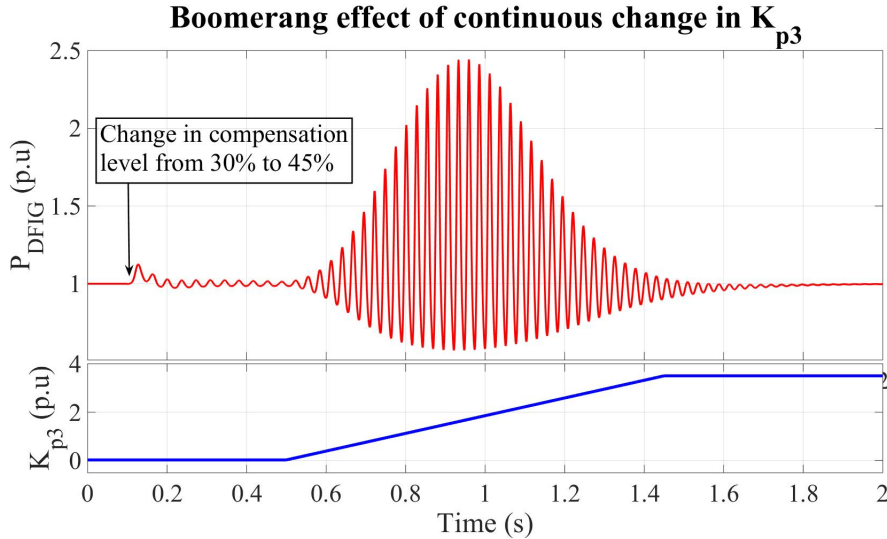


Figure 5.8: The boomerang effect of K_{p3} on DFIG system.

The value of K_{p3} in the system is initially set to 0.004 p.u., for any possible requirement of a low gain for the normal DFIG operation at 30% compensation level. At 0.1 s, a disturbance occurs and the compensation level get increased to 45%. The system stays stable and damps the oscillations. However, another disturbance occurs at 1 s, when the compensation level get 65%, this time the undamped oscillations come in to existence. As the oscillations grow, the instability in the system is detected either by the operator or protection system. After detection of SSCI, the gain K_{p3} is increased to a higher value to mitigate SSCI, and even in run-time, the increase in K_{p3} to an appropriate value mitigates SSCI from the system. The new values keeps the system immune to SSCI even after another disturbance of the change in compensation level to 85%.

The oscillations caused by SSCI grow faster because of it being an electrical phenomenon. Therefore if there is a need to change K_{p3} to a higher stable value during SSCI event, then the detection of the growing oscillations should be fast so that K_{p3} can be changed in a safer time. To detect the undamped oscillation in the system at sub-synchronous frequencies, a simple algorithm is developed which measures the dc-link voltage V_{dc} and compares it with the reference voltage. If the actual voltage deviates from the reference values, and if this deviation keeps on

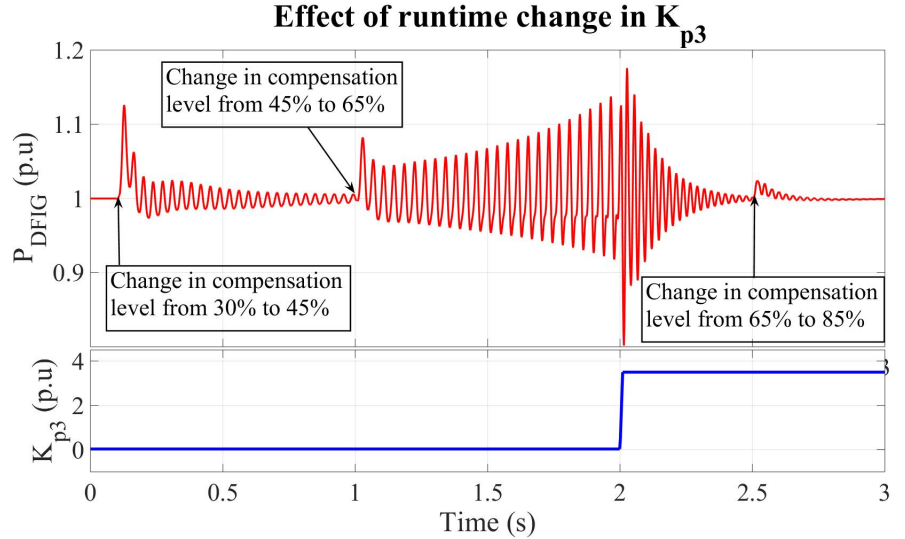


Figure 5.9: Runtime effect of K_{p3} to mitigate SSCI.

increasing in second or third cycle then the growing oscillations in the system are detected and the scheduling of K_{p3} to a higher stable value is triggered. The flow chart of the algorithm is shown in fig. 5.11. The algorithm developed for the detection of SSCI is simple and has much room for improvement as the main purpose here is only to see whether the real-time change of K_{p3} can mitigate SSCI after its occurrence and detection.

The detection algorithm for SSCI is implemented in DFIG system to schedule K_{p3} after detection of SSCI. The result of the implementation of the algorithm is shown in fig. 5.10. In order to see that the algorithm only detects SSCI in the system and not any other disturbance or other damped oscillations, at first the reference value of dc-link voltage was increased at 0.1 s. It can be seen that the gain scheduling was not triggered as the algorithm does not detect this disturbance as SSCI.

The reference value is changed again at 1 s, and here again the scheduling is not triggered. At 2 s, the compensation level is decreased from 40% to 10% to generate damped oscillations in the system. Although these are the oscillations of voltage but still the gain is not triggered because the oscillations are not growing. However, at 3 s, when the compensation level is increased to 55%, there are

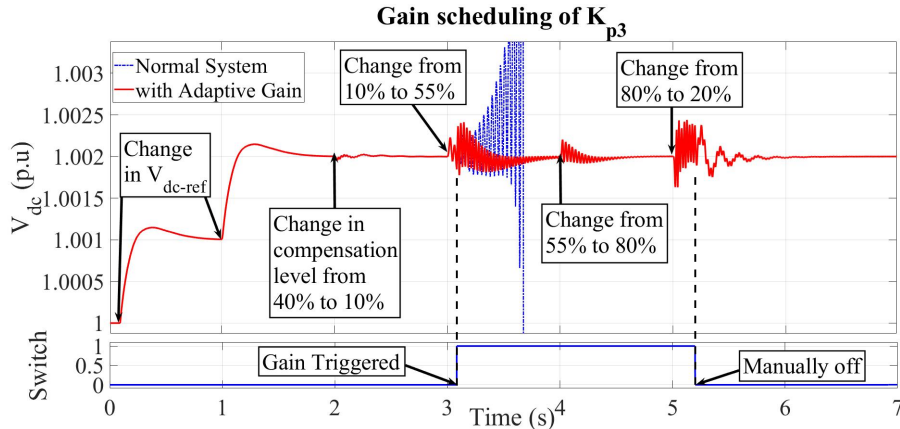


Figure 5.10: Gain scheduling of K_{p3} after SSCI detection.

undamped oscillations in the system and the gain is triggered as soon as SSCI is detected. K_{p3} is increased to a higher stable value and keeps the system free from the risk of SSCI even for the change of compensation level to 80% at 4 s. When the system is restored back to a compensation level where the normal low gain of K_{p3} can be selected then the gain is restored manually for the normal operation of DFIG.

5.1.4 Experimental Validation of SSCI Analysis and Mitigation

The theoretical findings of the analysis of SSCI in DFIG-based system, that are obtained in Chapter 4, and the findings of SSCI mitigation presented earlier in this chapter, are then validated through the experiments on actual DFIG-based system.

Experimental Setup

A downscaled 7.5 kW DFIG is used for the experimental validation of the analysis and mitigation of SSCI. The experimental facility at the Department of Energy Technology at Aalborg University, Denmark, is used for this research work. The experimental setup is shown in fig. 5.12. The DFIG is externally driven by prime motor. For RSC and GSC, two 5.5 kW Danfoss motor drives are used. The Danfoss motor drives are controlled with dSPACE 1006 control system. The control strategy for RSC and GSC is designed in MATLAB/Simulink and is transferred to

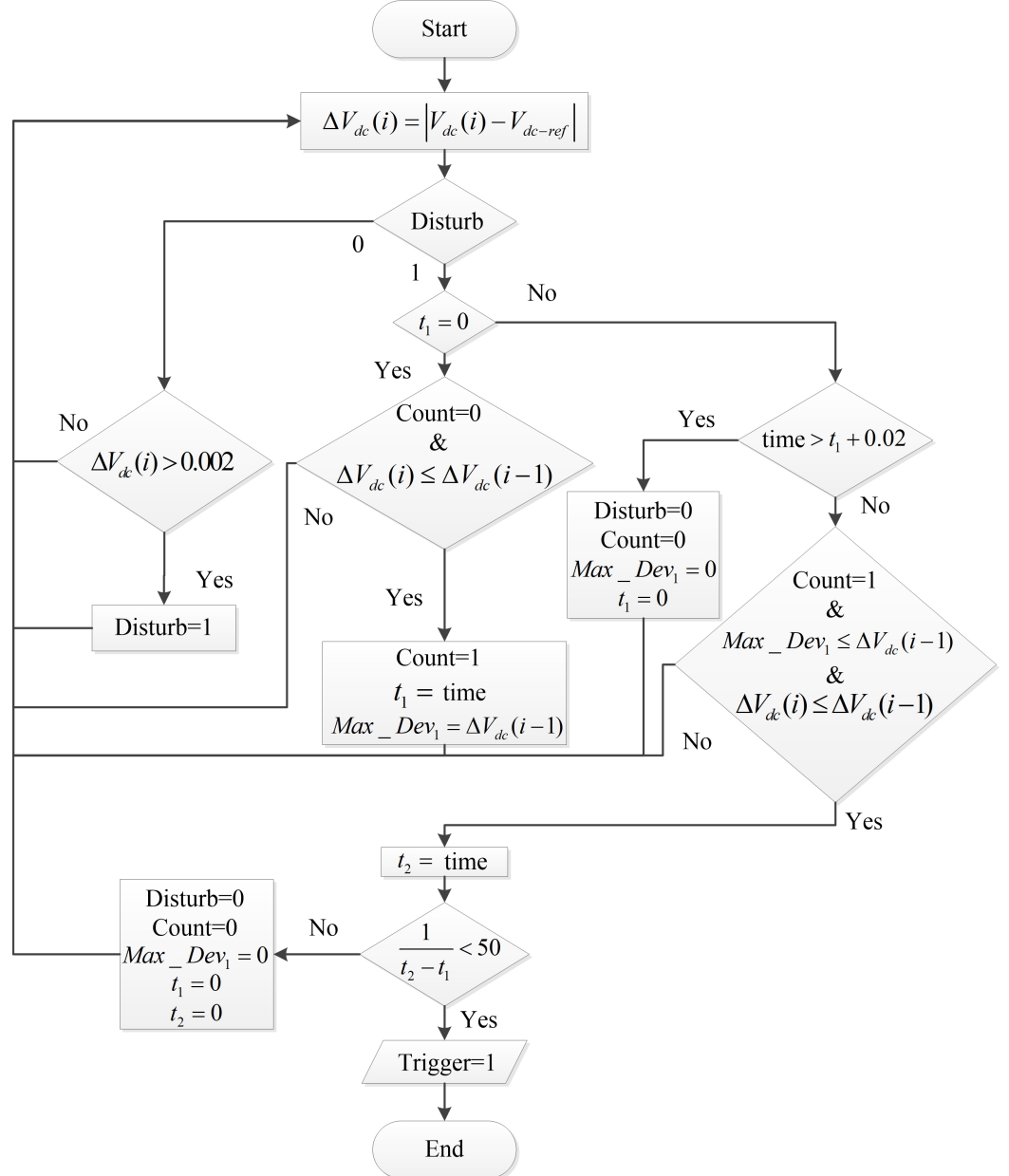


Figure 5.11: Flowchart of SSCI detection and gain scheduling.

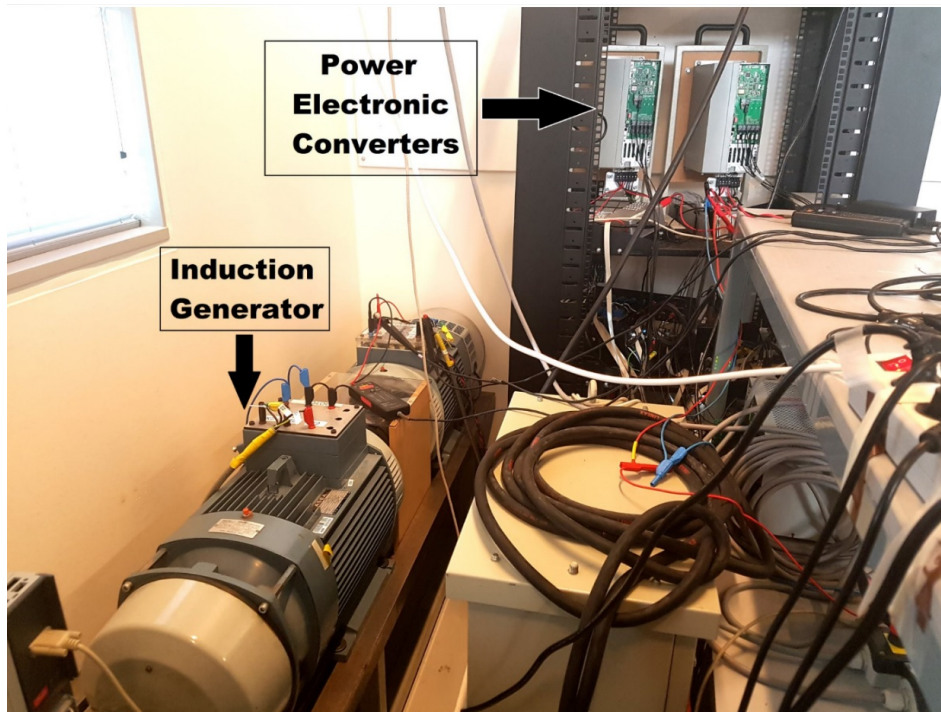


Figure 5.12: Experimental setup of DFIG test system.

dSPACE. The sampling frequency of both drive is 10 kHz and the switching frequency is 5 kHz. The RSC, GSC and dc-link of the experimental setup is shown in fig. 5.13.

The DFIG is connected to the grid via series compensated transmission line. For this research, the experiments are conducted for different compensation levels of the transmission lines. The compensation levels ranged from the experimental value of 33.7% up to 92.1%. The test setup of line resistors, inductors, and series compensation capacitors is shown in fig. 5.14. The results obtained from DFIG test setup are gathered from the digital oscilloscope, as shown in fig. 5.15. The results are converted to data files, which are then used in MATLAB to plot the figures.

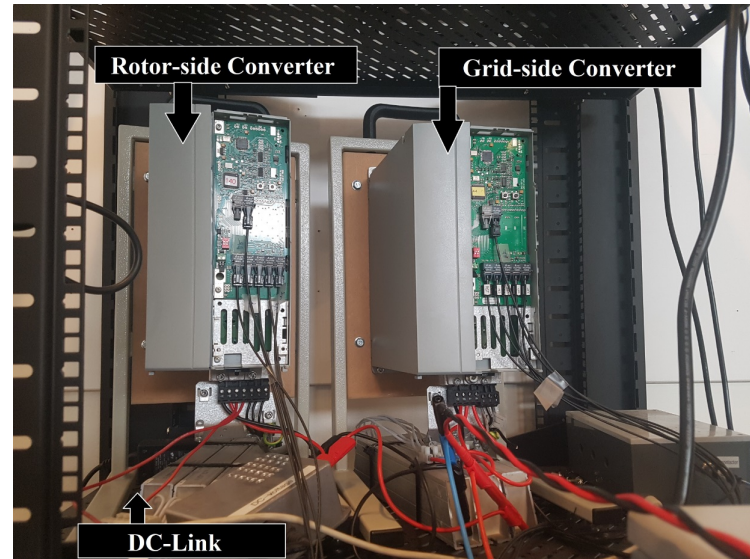


Figure 5.13: Power electronic converters and dc-link.

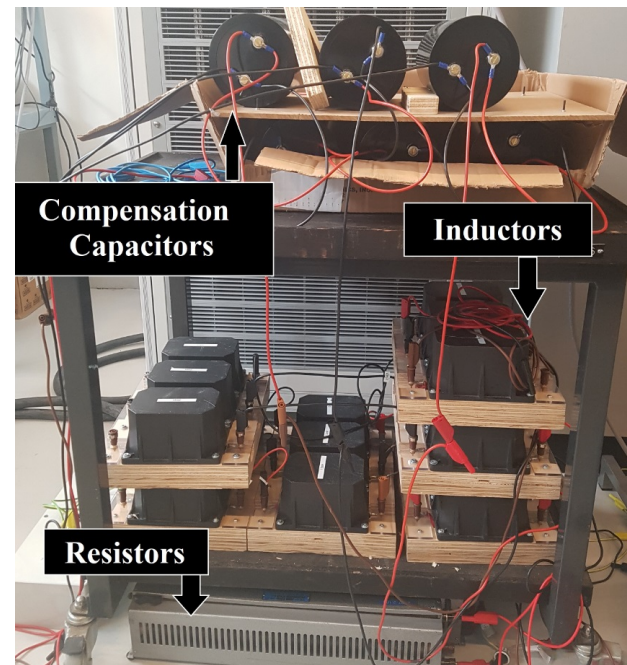


Figure 5.14: Resistors, inductors, and series compensation capacitors.

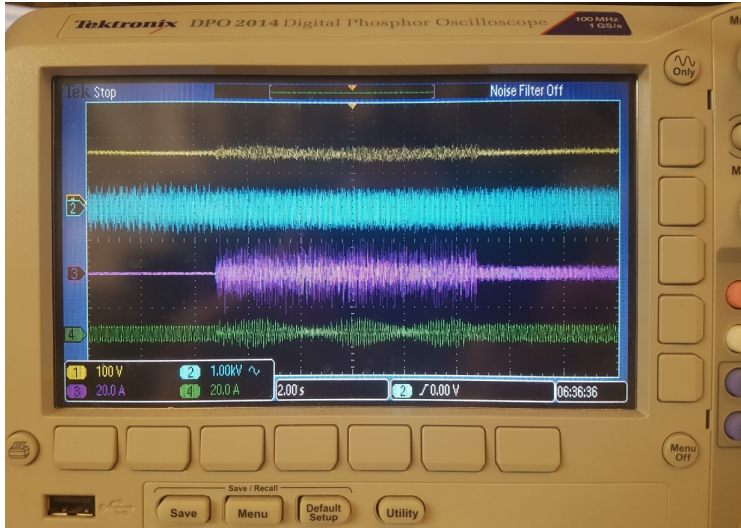


Figure 5.15: Experimental results displayed on oscilloscope.

Experimental Results

For the experimental validation of the theoretical findings, the DFIG system is operated at different values of the significant control parameters and for different series compensation levels. At first K_{p3} is kept to 0.1 p.u., and the DFIG is connected to main grid via 74.6% compensated line. The response of the system for dc-voltage V_{dc} , stator current I_{stator} , and rotor current I_{rotor} is obtained from the oscilloscope and is shown in fig. 5.16. It can be seen in the figure that as soon as the DFIG is connected to the series compensated line, there arise the oscillations in the system. This is because the value of K_{p3} is in the phase of the boomerang where the SUB mode is either negative or very close to zero damping ratio.

Now, the gain K_{p3} is further increased to 1 p.u.. It can be seen in fig. 5.17 that as soon as the DFIG is connected to the compensated line, the undamped oscillations appeared in the system. The oscillations with $K_{p3}=1$ p.u. have higher growth rate as compared to the oscillations with $K_{p3}=0.1$ p.u., because at 1 p.u. the SUB mode is at the phase of the boomerang where it has higher negative damping ratio. The oscillations in the system shown in fig. 5.17 keep on appearing in the system until the compensated line is disconnected from DFIG.

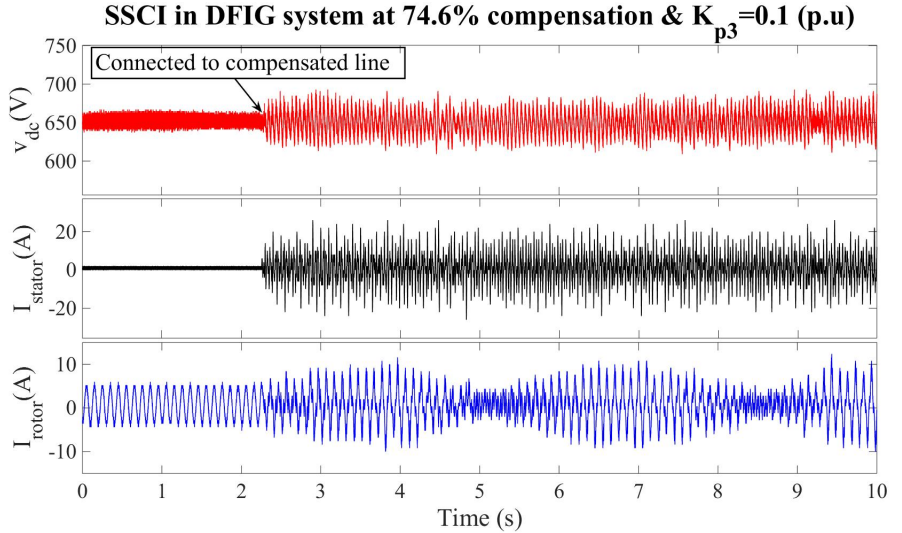


Figure 5.16: SSCI in experimental setup of DFIG.

Fig. 5.18 shows the zoomed in version of the oscillation in dc-voltage of DFIG from 5.17. It is clear from the figure that the frequency of the undamped oscillations in the system is approximately 27 Hz, which is in sub-synchronous range and is very much in accordance with the frequency of the SUB mode given in Table 4.1.

It is shown in Chapter 4 that the proportional parameters of outer loop power controller of RSC also have an impact on SUB mode of the system. It is shown in Section 5.1.2 that the K_{p3} should be kept as low as possible otherwise its higher value will push SUB mode towards instability. To validate its effect experimentally, the DFIG system is operated with $K_{p3}=0.1$ p.u. and then K_{p1} is increased from 0.1 p.u. to 0.5 p.u. at 74.6% compensation level, the result is shown in fig. 5.19.

It can be seen from the figure that at the start when the compensated line is connected to DFIG, there are some oscillations in the system similar to the one shown in fig. 5.16, because $K_{p3}=0.1$ p.u. However, when the value of K_{p1} is increased to 0.5 p.u., it adds up to already existing oscillations and the oscillations grow aggressively, such that the oscillations enable the protection system of DFIG, and disconnects it from the grid.

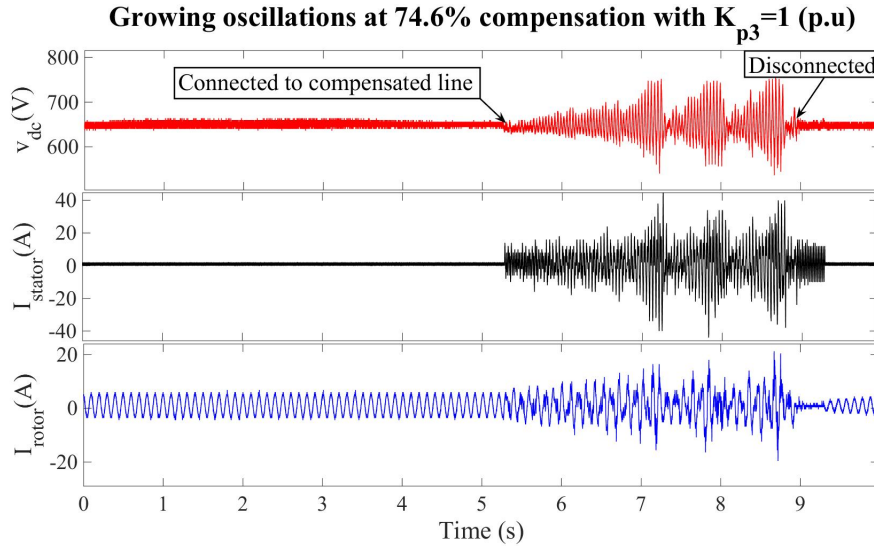


Figure 5.17: Undamped oscillations in experimental setup of DFIG.

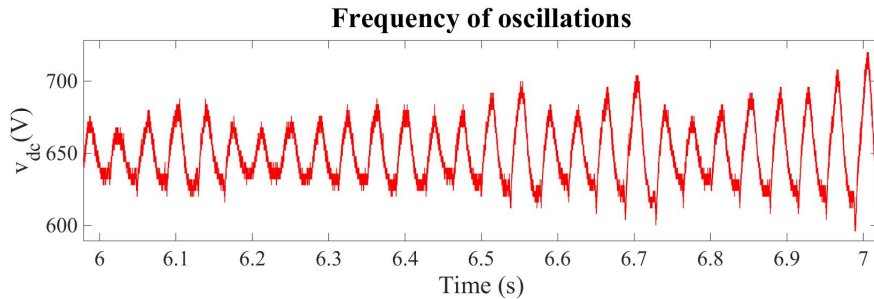


Figure 5.18: Frequency of the undamped oscillations in dc-link voltage.

To validate the mitigation of SSCI through proper selection of RSC proportional parameters, the DFIG is operated with $K_{p3}=1$ p.u. to observe the undamped oscillations in the system, as shown in fig. 5.20.

As soon as the DFIG is connected to the compensated line, the growing oscillations are observed in the system. It is shown theoretically in Section 5.1.2, that to mitigate SSCI from the system, K_{p3} should be increased beyond 2.5 p.u., same is done during the experiment. As soon as the value of K_{p3} is increased from 1 to 6 p.u., the oscillations from the system disappeared, the SSCI is mitigated, and the

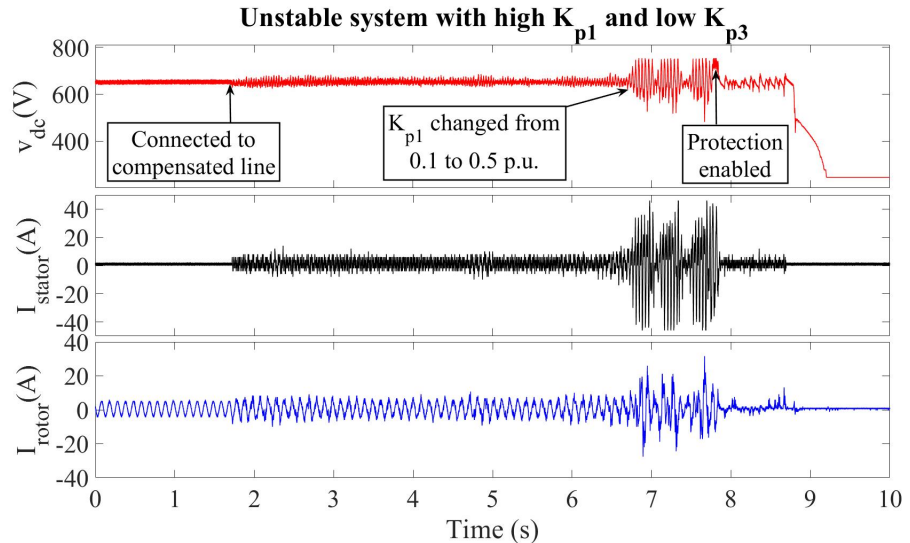


Figure 5.19: Aggravation of SSCI with wrong choice of RSC parameters.

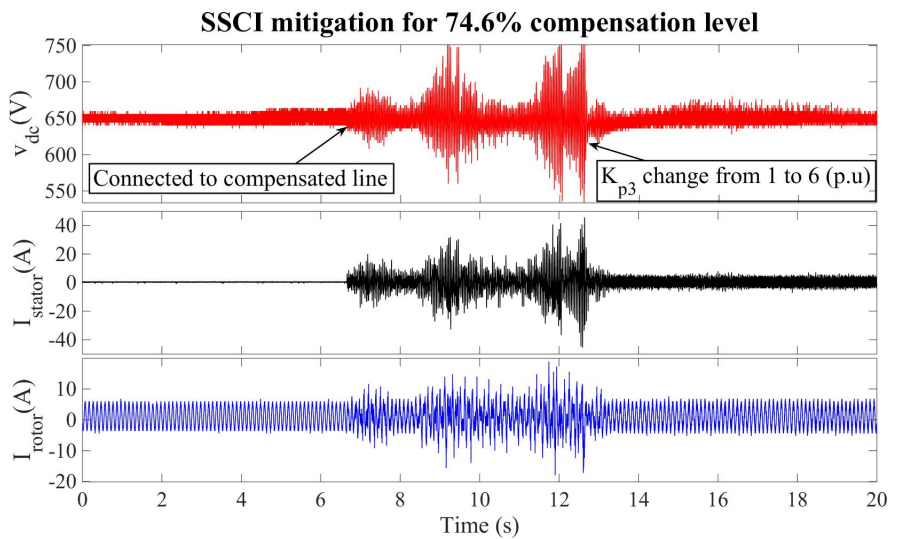


Figure 5.20: Mitigation of SSCI from DFIG system.

system is brought back to the normal operation. The response of the system shown in fig. 5.20, not only demonstrates that the proper gain of RSC control parameters mitigate SSCI, but it also shows that it adds considerable damping in the system.

By looking at the response of the system with the value of K_{p3} as 0.1, 1, and 6 p.u., it is clear that the boomerang effect of K_{p3} appears in the experimental setup as well. Although the recommended value of K_{p3} based on the parameters of experimental setup is 4 p.u., as discussed in Section 5.1.2, but a higher value of 6 p.u. is used to mitigate SSCI experimentally, hence showing that DFIG operates safely even at the value of K_{p3} higher than the recommended one.

The experiment on DFIG setup are conducted for the series compensation levels of 33.7%, 42.2%, 50.6%, 63.3%, 74.6%, 84.4%, and 92.1%. For all the compensation levels, the boomerang effect of K_{p3} is observed, and the SSCI is mitigated from the system as soon as the value of K_{p3} is increased beyond 2.8 p.u.

5.2 Mitigation through Supplementary Control Signal

This section deals with the design of a supplementary controller in order to mitigate SSCI. The design of power oscillation damper (POD) is discussed and explained here. A Residue based method is used to tune the parameters of the damper and its proper placement in the VSC controllers is determined. Moreover, different signal, that are used as the inputs to the POD, are taken into consideration and their effect on the modes of interest is analyzed in this section.

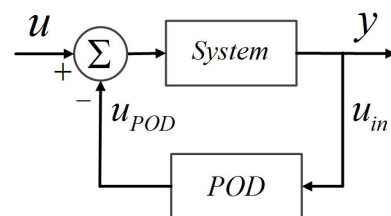


Figure 5.21: Addition of POD in a system.

5.2.1 Power Oscillation Damper (POD)

POD is basically a controller which takes in an input from the system and provides a supplementary control signal to the system as its output. A simple block diagram which illustrate the addition of POD in to a system is shown in fig. 5.21. In the figure it can be seen that the POD takes a signal from the system as its input, processes the signal, and the provides its output u_{POD} as a supplementary control signal to the system. In order to use POD for the mitigation of SSCI, the output signal of the POD is added to the controllers of VSCs of DFIG, as a supplementary control signal. The block diagram of the POD is shown in fig. 5.22. A POD is made up of 3 blocks which are,

1. Gain block:

The POD takes an input signal u_{in} from the system and then first passes it through the gain block. This blocks multiplies the input signal with selected gain. This selected gain determines the damping provided by the POD. The gain of the POD is required to be selected optimally, as the increasing gain of POD would possibly increase the damping of mode of interest, but it might has an adverse effect on the damping of other system modes. Ideally, the value of gain should be set such that it provides maximum damping to the system, however, it is often limited because of certain limitations of the system.

2. Washout block:

The signal u_{in} further gets processed through the washout block. A washout block is a high-pass filter which filters out the noises of low frequencies. This block eliminates the effects of any steady-state value of u_{in} . The time constant of washout filter T_w usually has the value between 1 to 20 s. For this research work, the value of T_w set equal to 5 for all considered cases.

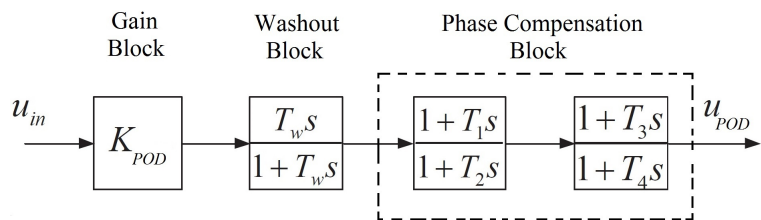


Figure 5.22: Block diagram of POD.

3. Phase compensation block:

The phase compensation block consists of a lead-lag filter and adds phase to the signal. The extent of phase added is dependent upon the selected values of filter parameters. The appropriate phase-lag or phase-lead characteristics, for providing high damping to the system, can be obtained by tuning the lead-lag filter properly. It can be seen in fig.5.22 that there are two filters in the phase compensation block. Normally only one filter is used when the required phase compensation is less than 60° , as because of practical reasons the argument of lead-lag filter is limited to 60° [65]. If the required phase compensation is greater than 60° then the second filter is used. For using the POD to mitigate SSCI, the phase compensation block is tuned using residue based method.

Residue

In simple control engineering term, residue can be defined as the product of the observability and the controllability of the system [76]. Mathematically, the residue can be determined as,

$$\bar{R}_i = CV_i^r V_i^l B \quad (5.2)$$

where V_i^r and V_i^l are the right and left eigenvectors, respectively, corresponding to i th eigenvalue. The residue of the i th eigenvalue consists of a magnitude and an angle, i.e., $\bar{R}_i = R_i \angle arg(R_i)$. The residue provides the information about the direction of movement of i th eigenvalue. The angle of the residue determines the direction of the movement, and the magnitude of the residue determines the pace with which the i th eigenvalue will move. The information of i th eigenvalue based on the residue can be used to move the eigenvalue from initial position to desired position.

The concept of residue can be further simplified by considering a closed loop single-input single-output system, as shown in fig. 5.23. In fig. 5.23, $G(s)$ and $H(s)$ are the open-loop transfer functions of the main system and the feedback gain, respectively, and u and y are the input and output of the system, respectively.

For this configuration the open-loop transfer function $G(s)$ of the system can be expressed as [76],

$$G(s) = \frac{Y(s)}{U(s)} = \sum_{i=1}^n \frac{\bar{R}_i}{s - \lambda_i} \quad (5.3)$$

where $U(s)$ and $Y(s)$ are the Laplace transforms of u and y .

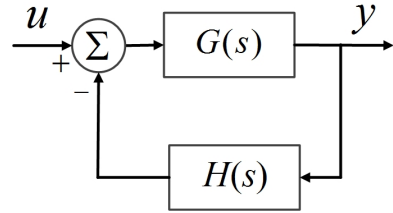


Figure 5.23: Closed-loop system.

Because of the feedback loop $H(s)$ there will be an effect on the eigenvalues of the system having transfer function $G(s)$, and because of this effect there will be movements by the eigenvalues. The mathematical relation between the change of the feedback transfer function $H(s)$ and the movement of the eigenvalues of $G(s)$ can be written as [77],

$$\Delta\lambda_i = \bar{R}_i H(\lambda_i, k) \quad (5.4)$$

where k is the gain of the feedback loop. It can be seen in (5.4) that the transfer function of the feedback loop has a direct relation with the movement of eigenvalues of the system. It would be pertinent to mention that according to (5.4), the position of eigenvalue can be changed from actual to desired position by manipulating the transfer function of feedback loop $H(s)$, through proper tuning of its parameters.

To mitigate the SSCI in DFIG-based system, the design of POD is done by calculating the residues of modes of interest and by using the information of residue to tune the parameters of POD.

Tuning of Phase Compensation Block

In this subsection the tuning of POD parameters using residue method is discussed. The POD is tuned separately for different input signals and for different placements of POD in the VSC controllers of DFIG. Consider that the POD is added in to the designed DFIG-based system such that $G(s)$ corresponds to the transfer function

of DFIG-based system and $H(s)$ corresponds to the transfer function of POD, respectively, in fig. 5.23. It means that the POD is connect to the system through a feedback loop. Similar to the concept of (5.4), the POD will be tuned such that it can move the eigenvalue corresponding to the mode of interest to the desired position to provide maximum damping to the system as illustrated in fig. 5.24.

The residue method is used to tune the parameters T_1, T_2, T_3 and T_4 of lead-lag filters of POD. As discussed earlier, the residue of an oscillatory mode provides the information about the movement of eigenvalue from its initial position as a result of a small change in system parameters. The information about the angle of departure of the mode of interest can be used to tune the lead-lag filter such that it can provide an appropriate phase compensation to move the eigenvalue to the desired position. The compensation of phase of the eigenvalue corresponding to mode of interest is visually depicted in fig. 5.24. It can be seen that in order to move the eigenvalue to the desired position, the phase compensation of ϕ degrees should be provided, and ϕ can be found as,

$$\phi = 180^\circ - \arg(R_i). \quad (5.5)$$

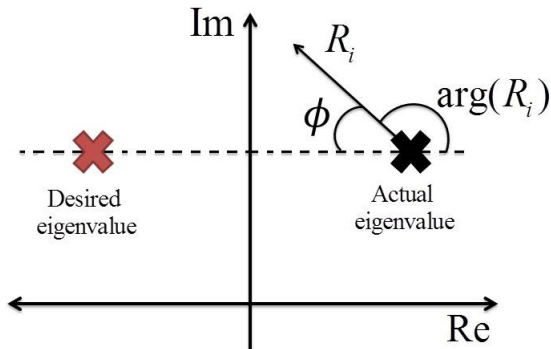


Figure 5.24: Graphical representation of residue.

The parameters of lead-lag filter dictate the phase lead or lag in the direction of movement of the eigenvalue. The number of filters to be used is dependent upon the phase compensation angle ϕ . If the required value of ϕ is less than 60° then only one lead-lag filter will be used and the parameters of second lead-lag filter will be equal, i.e., $T_3 = T_4$. If the required ϕ is between 60° and 120° then the second lead-lag filter will be used such that its parameters will be $T_3 = T_1$ and $T_4 = T_2$, and

if the required ϕ exceeds 120° then only one filter will be used but the gain of POD should be negative. As shown in fig. 5.22, the transfer function of the lead-lag filter is,

$$G_{lead-lag} = \frac{1 + saT}{1 + sT} \quad (5.6)$$

where $T_1 = aT$ and $T_2 = T$.

The value of a is kept greater than 1. In order to avoid the amplification of signal noise level and to minimize the gain of high frequency, the value of a should be kept as small as possible. The desired compensation angle ϕ of POD can be found as [78],

$$\frac{\phi}{n_f} = \sin^{-1} \left(\frac{a-1}{a+1} \right) \quad (5.7)$$

where n_f is the number filters used. The parameter a can be found by rearranging the above equation,

$$a = \frac{1 + \sin \left(\frac{\phi}{n_f} \right)}{1 - \sin \left(\frac{\phi}{n_f} \right)}. \quad (5.8)$$

From (5.6), the parameter a is now known. In order to calculate the other unknown parameter T consider the angular frequency ω_i of the mode of interest, at which the maximum phase lead or phase lag angle occurs. The relation between ω_i and T can be given as,

$$\omega_i = \frac{1}{T\sqrt{a}} \quad (5.9)$$

$$T = \frac{1}{\omega_i\sqrt{a}} \quad (5.10)$$

The parameters of lead-lag filters T_1 and T_2 can be found using (5.6) and (5.10). For the parameters of second filter, if only one filter is being used then $T_3 = T_4 = 1$, and if two filters are used then $T_3 = T_1$ and $T_4 = T_2$.

Selection of POD Gain

For every placement of POD in to the system and for every input signal to POD, the gain of POD is selected. The tuned lead-lag filter determines the direction of movement of eigenvalue, while the gain of the POD dictates the distance of movement from the initial position. As mentioned earlier, the tuned POD adds damping to the oscillatory mode of interest while affecting the other modes, and this may have an adverse effect on other modes. So the gain of the POD is selected such that it can provide maximum damping to the system without worsening the damping of modes, other than the mode of interest. Using root-locus plot, the gain of POD for every placement in the VSC controller and for every input signal is determined separately, by choosing the gain which provides the maximum damping to the system.

Root-locus plot shows the behaviour of system when supplementary signal is added in to it. Simulink provides an interactive root-locus plot of the closed loop system, which shows the movement of all the eigenvalues of the system with respect to the change in the gain of feedback loop. This interactive root-locus plot is used to select the value of gain which can provide an overall maximum damping to the system.

5.2.2 Analysis of POD

Only for the analysis of POD in Section 5.2, a DFIG system is used in which the controller of RSC is designed in stator flux oriented reference frame. The parameters of this system are given in Appendix in Table 6.3. Since the only major difference as compared to the main DFIG system model is the change of controller reference of RSC, therefore the conclusions drawn from this analysis of POD hold true for the main DFIG system as well.

After taking the input signal from the system, the POD processes it and give a supplementary signal u_{POD} to the summation junctions of the controllers of DFIG converters. The active power P_{DFIG} , the apparent power S_{DFIG} generated by the DFIG, and the current I through transmission line are used in the POD as u_{in} . the output signal of POD u_{POD} is individually placed at every summation junctions of converters controllers. The position of the junctions of each controller is classified by naming them as '1', '2', and '3'. The example of the classification of controller

Table 5.1: Eigenvalues of Modes of Interest at 65% Compensation Level

Mode	Eigenvalues	Frequency (Hz)	Damping Ratio
Sub-synchronous (SUB)	$2.67 \pm j 135.61$	21.58	-0.019
Super-Synchronous (SUP)	$-6.13 \pm j 453.8$	72.2	0.013
Control (CN-1)	$-26.97 \pm j 44.12$	7.02	0.521
Control (CN-2)	$-19.51 \pm j 24.69$	3.39	0.620

junctions is shown in fig. 5.25.

The controller of RSC that controls reactive power is displayed in the figure. There

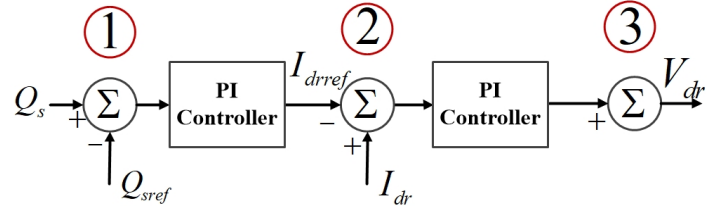


Figure 5.25: Different junctions of RSC controller.

are three junctions in this controller and these junctions are named as $Q_s - 1$, $Q_s - 2$, and $Q_s - 3$. After the POD is added in the converters, individually to different junctions, an observation is made through the root-locus method. The observation concludes that four of the modes of the system are considerably affected by the addition of u_{POD} . This observation is made for all the three input signal to the POD. The details of these modes of interest of the system considered for the analysis of POD are shown in Table 5.1. The residues of each mode of interest are calculated while keeping the compensation level to 65%. The placement of u_{POD} in each junction of RSC and GSC controllers is considered and for each u_{in} .

For the modes CN-1 and CN-2, the state variables corresponding to the controllers of RSC and GSC showed comparatively higher participation, that is why these modes are named as control modes (CN).

In the following sub-sections, the effect of POD on the DFIG-based system is analyzed for all the three input signals, one by one.

DFIG Active Power (P_{DFIG}) and Apparent Power (S_{DFIG}) as Input to POD

The generated active power P_{DFIG} and the magnitude of apparent power S_{DFIG} are used as the input signal to the POD, turn by turn. The POD is then added in to all the summation junctions of RSC and GSC controllers individually. With both these inputs the DFIG system shows similar response, therefore the response of only P_{DFIG} as an input is discussed here. For each placement of the POD in RSC and GSC, the residues of all the modes are calculated. Table 5.2 shows the respective residue magnitudes and angles of the modes corresponding to the junctions of interest when u_{POD} is added with $u_{in} = P_{DFIG}$.

Table 5.2: Residues of Modes of Interest at 65% Compensation Level

P_{DFIG} as Input to POD			
	SUB	SUP	CN-2
Eigenvalues	$2.67 \pm j135.61$	$-6.13 \pm j453.8$	$-19.51 \pm j24.69$
$Q_s\text{-1}$	$24.4\angle -165^\circ$	$36.4\angle 17.9^\circ$	$0.98\angle 176.3^\circ$
$V_{dc}\text{-1}$	$184.1\angle -75.1^\circ$	$130.1\angle 44.4^\circ$	$37.4\angle 143.4^\circ$
$V_{dc}\text{-2}$	$34.3\angle -54.8^\circ$	$25.8\angle 50.7^\circ$	$6.03\angle -127.3^\circ$
$V_{dc}\text{-3}$	$38.0\angle -0.42^\circ$	$47.6\angle 74.6^\circ$	$2.09\angle -6.7^\circ$
$Q_{gsc}\text{-1}$	$66.24\angle -145.5^\circ$	$103.2\angle 23.9^\circ$	$2.2\angle 163.5^\circ$
$Q_{gsc}\text{-2}$	$6.59\angle -141.3^\circ$	$10.32\angle 25.2^\circ$	$0.26\angle -179.2^\circ$
$Q_{gsc}\text{-3}$	$5.25\angle -105.1^\circ$	$10.1\angle 37.6^\circ$	$0.09\angle -68.0^\circ$

$Q_s - 1$ is the summation junction of the RSC controller and $Q_{gsc}\text{-1}$, $Q_{gsc}\text{-2}$, $Q_{gsc}\text{-3}$, $V_{dc} - 1$, $V_{dc} - 2$, and $V_{dc} - 3$ are the summation junctions of the GSC controller. Based on Table 5.2, the SUB mode has the least damping ratio in the system, therefore, the lead-lag filter of the POD is tuned to give the phase compensation to SUB mode. The POD is capable of moving the SUB mode towards the stability but the problem arises when other modes are deteriorated by the POD and expose the system to the risk of instability. The lead-lag filter tends to compensate the phase of the residue of the mode such that it moves towards left-half plane along real axis without allowing significant movement along imaginary axis. For this purpose the information about residue angle is crucial.

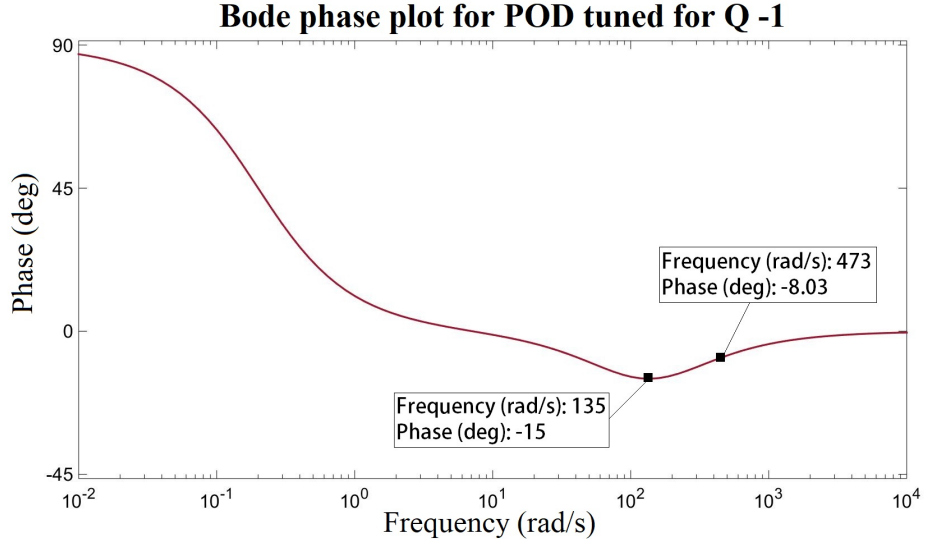


Figure 5.26: Bode phase plot of tuned POD added in junction $Q_s - 1$.

When POD is added to $Q_s - 1$ junction, the residue angle of SUB mode is calculated to be -165° , as shown in Table 5.2. Therefore, the lead-lag filter require to add a phase of around -15° to make SUB mode to move towards left-half plane. The Bode plot of tuned POD is shown in fig. 5.26. It can be seen that the tuned POD gives a phase shift of -15° to the mode of angular frequency 135 which is the SUB mode in this case. However, POD also affect the modes of other frequencies, for instance the POD gives phase shift of around -8° to the mode of super-synchronous frequency, as seen from the figure ($\omega=453.8$ rad/s).

This effect of POD on the movement of eigenvalues corresponding to sub and super-synchronous frequencies is well illustrated in fig. 5.27. When POD is added in the system at junction $Q_s - 1$, the direction of eigenvalue of SUB mode is adjusted by the phase shift of -15° by the POD, this shift allows the respective mode to move along real axis only. Along with this, the POD also introduces a phase shift of around -8° in the direction of SUP mode.

The magnitude of POD gain will determine how far the eigenvalues will move from their actual positions. The residue magnitude of SUP mode is greater than that of SUB mode, in the case when POD is added at $Q_s - 1$, which means that

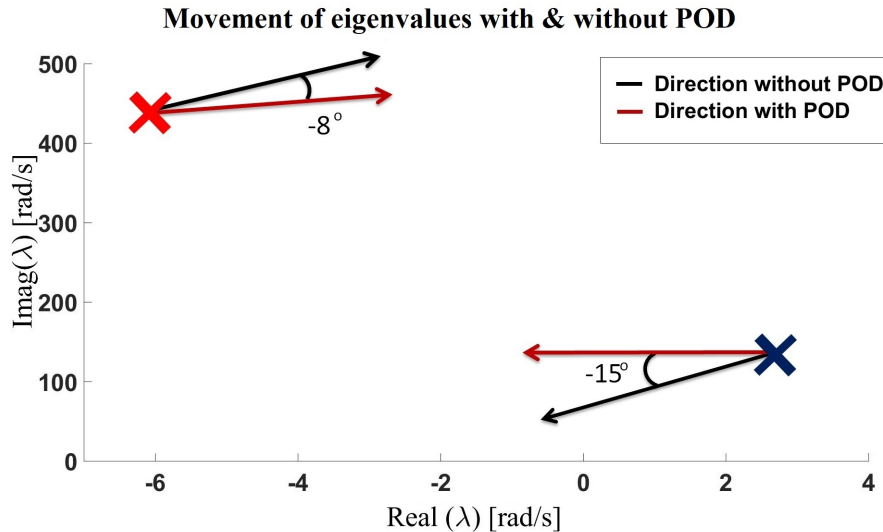


Figure 5.27: Movement of eigenvalues with and without POD at $Q_s = 1$.

for the same gain the SUP mode will move far from its actual position than SUB mode.

This explanation can be verified by the root-locus plot of the system, shown in fig. 5.28, when the POD with $u_{in} = P_{DFIG}$ is added at $Q_s - 1$ junction. The red crosses and squares show the open-loop and closed-loop poles, respectively, of system with POD. It can be seen in the figure that if the damping of SUB mode is increased by increasing the gain of POD, then the damping of SUP mode will decrease. The root-locus plot shows that the placement of POD in this junction will not be able to mitigate SSCI for higher series compensation levels.

By analyzing the root-locus plots, the residue characteristics of modes of interests, and the Bode plots for different placements of POD in RSC and GSC controllers, it is observed that when the input of POD is P_{DFIG} , the best results are achieved when POD is placed at $V_{dc} - 2$ and $V_{dc} - 3$ junctions in GSC controller. The root-locus plots for only $V_{dc} - 3$ junctions is shown in fig. 5.29, as the system exhibit similar behaviour for both the junctions.

The figure shows that higher damping can be introduced in the system by increasing the gain. CN-1 mode, however, seems to have an opposite direction. The residue of this mode, when POD is place at $V_{dc} - 3$ is calculated to be $9.7 \angle -141.13^\circ$. Although the CN-1 mode is moving toward right-half of the plane, with

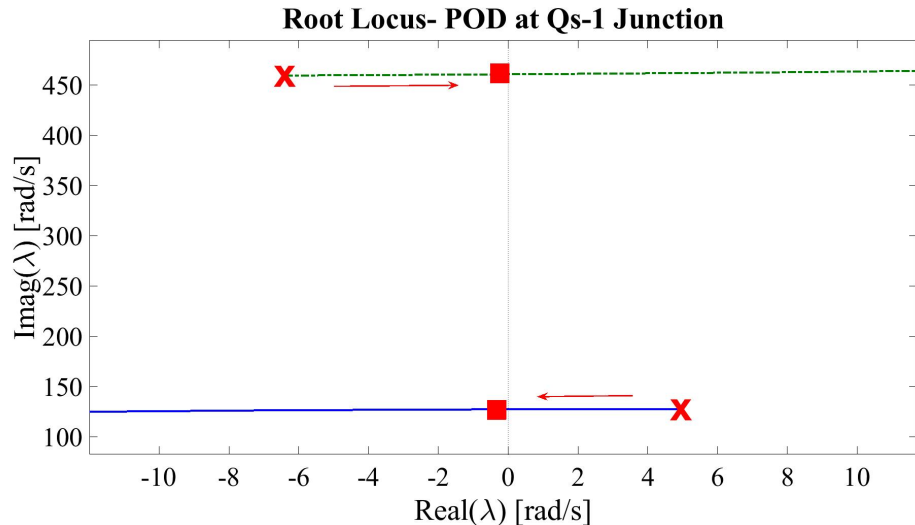
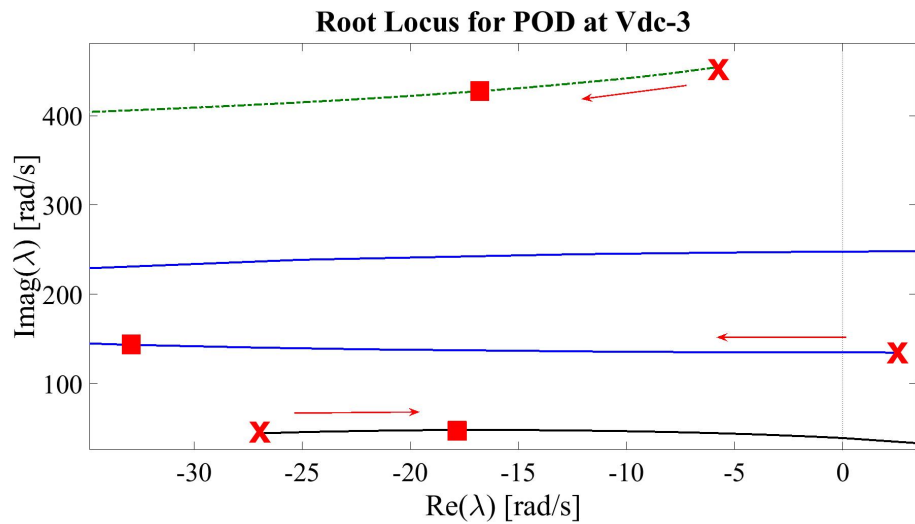
Figure 5.28: Root-Locus plot of system with POD at $Q_s - 1$ junction.Figure 5.29: Root-locus plot of system with POD at $V_{dc} - 3$ and $u_{in} = P_{DFIG}$.

Table 5.3: Residues of Modes of Interest at 65% Compensation Level

Line Current I as Input to POD			
	SUB	SUP	CN-1
Eigenvalues	$2.67 \pm j135.61$	$-6.13 \pm j453.8$	$-19.51 \pm j24.69$
$V_{dc}-1$	$162.5\angle-95.4^\circ$	$92.3\angle24.5^\circ$	$83.5\angle45^\circ$
$V_{dc}-2$	$30.3\angle-75.2^\circ$	$18.3\angle30.8^\circ$	$37.3\angle103.7^\circ$
$V_{dc}-3$	$33.6\angle-20.0^\circ$	$33.8\angle54.7^\circ$	$10.07\angle-149.4^\circ$
$Q_{gsc}-1$	$58.47\angle-165.9^\circ$	$73.3\angle4.0^\circ$	$2.55\angle-160.3^\circ$
$Q_{gsc}-2$	$5.82\angle-161.7^\circ$	$7.33\angle5.3^\circ$	$0.27\angle-149.9^\circ$
$Q_{gsc}-3$	$4.63\angle-125.5^\circ$	$7.17\angle17.8^\circ$	$0.169\angle-60^\circ$

the increase in the gain of POD, the comparative speed of the movement of CN-1 mode is very slow as compared to the other two SUB and SUP modes. This is because the residue magnitude of CN-1 mode is much lesser than that of other two modes. It allows the POD to add significant damping in the system.

Transmission Line Current (I) as Input to POD

The magnitude of the line current is also used as an input to POD, $u_{in} = I$, and its response is studied by individually adding the POD in all the junctions of the RSC and GSC controllers.

After studying the root-locus plots and the residue of mode of interests, it is observed that for the cases when the POD is added in all the junctions except for the junction of V_{dc} controller, any attempt to increase the stability of SUB mode results in the deterioration of SUP mode. However, this time for the addition of POD at junctions $V_{dc} - 1$, $V_{dc} - 2$ the CN-1 mode moves towards instability, when the gain of the POD is increased to stabilize the SUB mode. Table 5.3 shows the residue profiles of SUB, SUP, and CN-1 modes for the addition of POD in the junctions of interest.

It is important to notice that when the POD, with P_{DFIG} and S_{DFIG} as inputs, was placed at $V_{dc} - 2$, it was adding significant damping to the system, but in the case of $u_{in} = I$, the POD is unable to considerably improve the damping of the system. It can be seen in the table that the residue magnitude of CN-1 is higher than both SUB and SUP modes, that is why an attempt to increase the damping

of SUB mode will decrease the damping of CN-1 mode. This allows only a small improvement in the system's stability.

When the POD is placed at the $V_{dc} - 3$ junction, the damping of both the SUB and SUP modes increase with the increase in the gain of the POD, as shown in fig. 5.30. The CN-1 mode, however, has the opposite direction of movement but because of having a comparatively lower residue magnitude, the increase in the POD's gain does not affect this mode as much as it affects SUB and SUP modes, and that is why the gain of the POD can be increased to an extent where a significant damping in the DFIG system can be achieved.

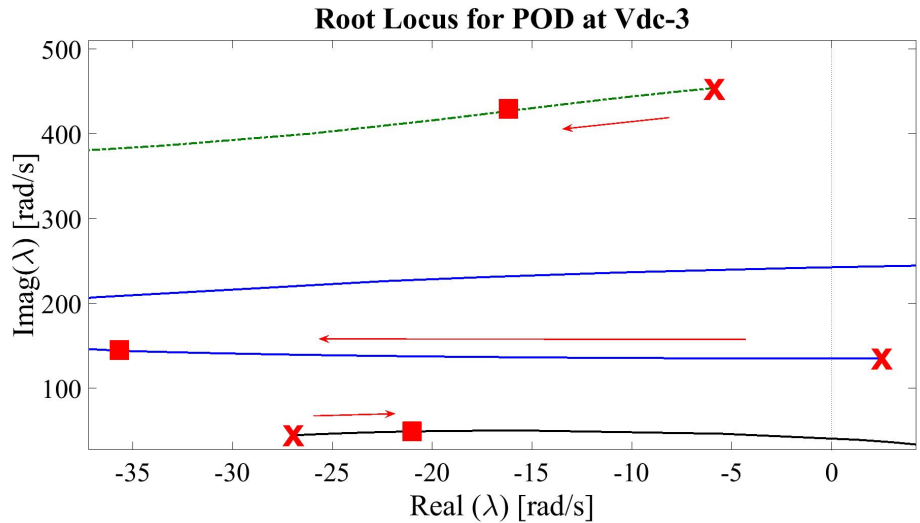


Figure 5.30: Root-locus plot of system with POD at $V_{dc} - 3$ and $u_{in} = I$.

5.2.3 Simulation Results

After analyzing all the input signals and after selecting the optimal placement of POD in the DFIG converters controllers, the simulation are performed for different series compensation levels to observe the occurrence of SSCI and its mitigation.

Results of Linearized System

As the designed system is linearized around one set of operating points, the residue of system modes will be different for different operating conditions. Because of

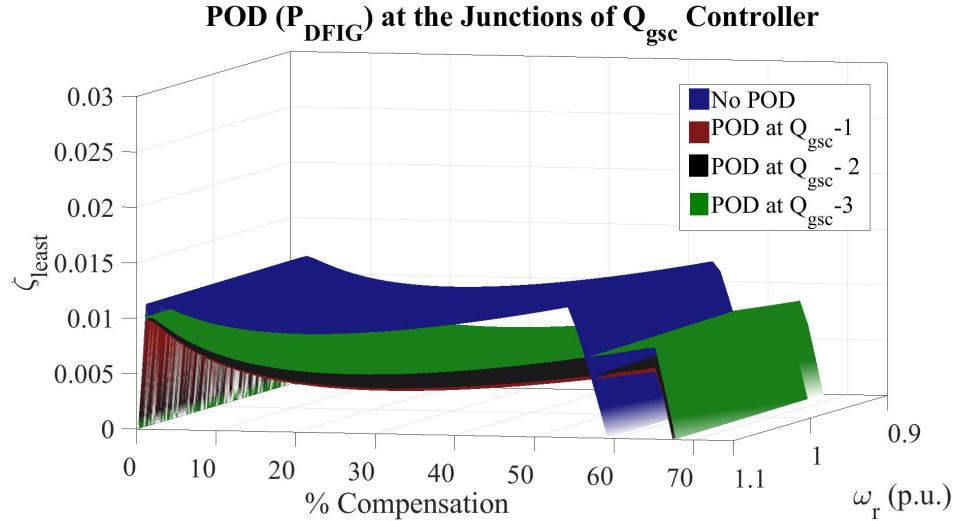


Figure 5.31: 3D plots for a system with and without POD at Q_{gsc} controller.

different residues of the modes of interest, the optimal parameters of POD will also be different. The objective here is to observe the performance of the POD for the fixed values of its parameters and gain for different operating conditions.

The simulations are performed to see the effect of the POD on the DFIG system, for different levels of series compensation and for different values of rotor speed. For the results shown in this section, the POD is placed in the GSC controllers. In fig. 5.31 and fig. 5.32, the 3D surfaces are plotted with the percentage compensation level along the x -axis, the rotor speed ω_r in p.u. along the y -axis, and the damping ratio of system's least damped mode ζ_{least} along the z -axis. In both the figures the input of the POD is active power generated by DFIG, i.e., $u_{in} = P_{DFIG}$.

From fig. 5.31 and fig. 5.32, it can be observed that when POD, with P_{DFIG} as an input, is added to $Q_{gsc} - 1$, $Q_{gsc} - 2$, $Q_{gsc} - 3$, and $V_{dc} - 1$, the POD might help in keeping the system stable for comparatively higher level of series compensation, but it lowers the damping of systems as compared to the system without the POD. As explained in previous section, this low damping is the result of deterioration of other system modes along with the improvement of sub-synchronous mode.

The results obtained from the cases when, POD with P_{DFIG} as an input, is added to $V_{dc} - 2$ and $V_{dc} - 3$ junctions show that the least damping ratio of the system increases with the increase in series compensation level. The addition of

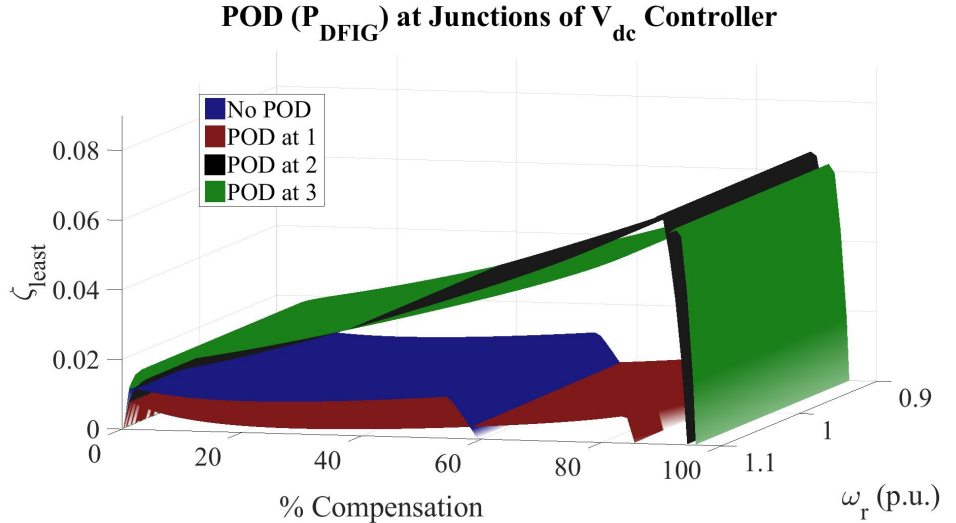


Figure 5.32: 3D plots for a system with and without POD at V_{dc} controller.

the POD at these two junctions allows the system to maintain its stability for any realistic level of series compensation, hence making the system immune to SSCI. The results shown in fig. 5.31 and fig. 5.32 are well in accordance with the outcomes concluded through residue profiles and root-locus plots in previous section. When POD is added to summation junctions of RSC controllers the system shows no significant improvement in its damping, as described in Section 5.2.2.

The movement of eigenvalues of SUB and SUP modes of the system is plotted in fig. 5.33. The movement is plotted while increasing the series compensation level from 10% to 95%. The damping ratio of the SUB mode of system without the POD, shown with blue markers, becomes negative as the level of compensation is increased beyond 60%. On the other hand the damping ratio of SUB mode, in the system with the POD, increases as the compensation level is increased. In this case the POD is added at junction $V_{dc} - 3$ with $u_{in} = P_{DFIG}$. It is can be seen from the figure that POD keeps the SUB and SUP modes stable even at the highest level of compensation, i.e., 95%, which shows that the designed control techniques makes the DFIG system immune to the SSCI for any realistic level of the series compensation of the transmission lines, and adds more damping to the system when the compensation level is higher.

It was observed in Section 5.2.2 that $V_{dc} - 2$ and $V_{dc} - 3$ are the best junctions

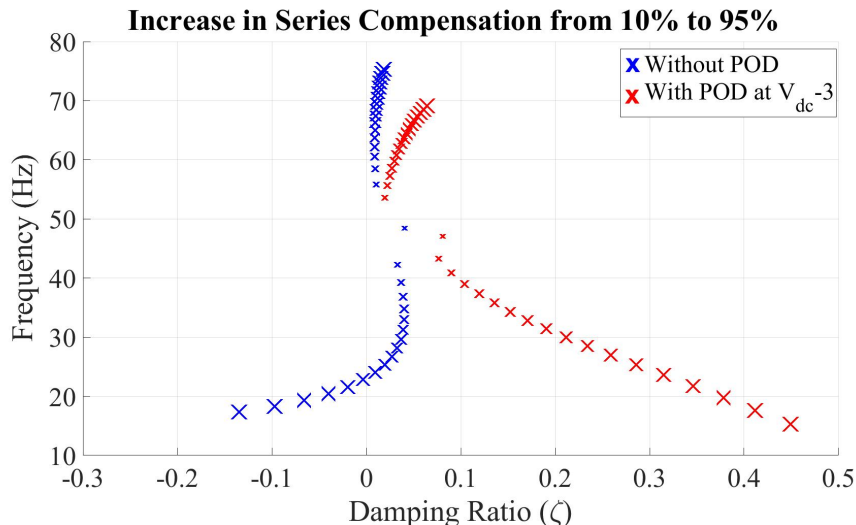


Figure 5.33: Effect of POD at $V_{dc} - 3$ junction with $u_{in} = P_{DFIG}$.

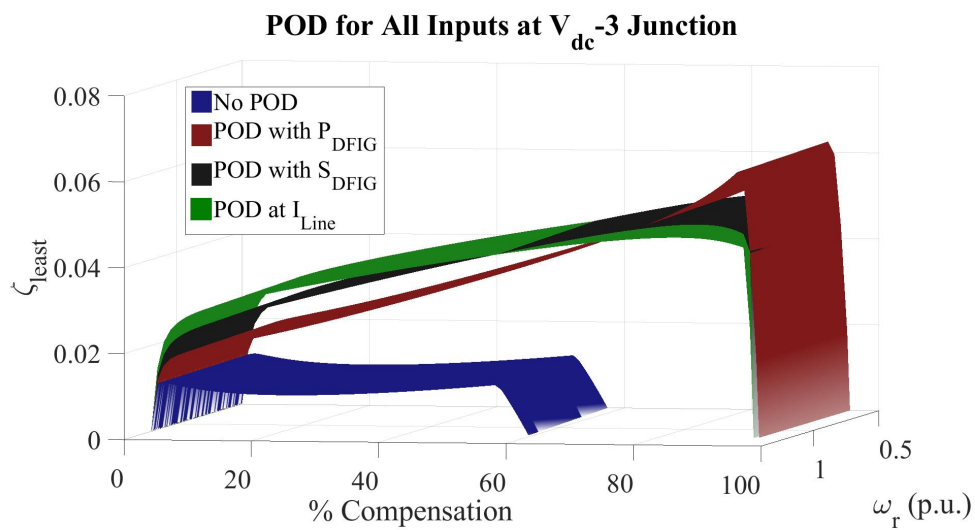


Figure 5.34: Comparison of POD with different inputs at $V_{dc} - 3$.

to add the POD with S_{DFIG} as the input. However, for $u_{in} = I$, the system shows substantial result for POD placement only at $V_{dc} - 3$ junction. The fig. 5.34 shows a comparison between the effects on the DFIG system by the POD for all the input signals at $V_{dc} - 3$ junction. With respect to the system without POD, all three input signals played the roles in making the system stable for high compensation level while making it highly damped. For the lower compensation levels, the POD with I as input shows the highest damping while for the compensation level greater than 80% the POD with $u_{in} = P_{DFIG}$ is the best of all.

Simulation of DFIG System

The non-linear system is simulated under different circumstances in order to validate the results obtained from the eigenvalue analysis of the linearized system. Here again, the POD is placed in all the junctions of GSC controller to see its effect on the DFIG system. For each particular placement, the POD is tuned to give the best damping at 65% series compensation level, and the parameters of POD, for each POD placement, are same as parameters used for its respective placement in linearized system.

At first the tuned POD, with P_{DFIG} as an input, is placed at all the junctions of Q_{gsc} controller while keeping the series compensation level to 50%. It can be seen in fig. 5.35 that as soon as compensation level is increased to 70% at 0.1 s, the SSCI is inflicted in the system.

In the system when no POD is added in Q_{gsc} controller, the oscillation grow very fast and collapse around 0.7 s. The systems with POD, however, go eventually towards instability but with slower speed. It shows that the tuned PODs added at all the three junctions of Q_{gsc} controller could add damping to the system at higher compensation level. This damping could only reduced the rate of growth of oscillation, as compared to system with out POD, but could not mitigate the occurrence of SSCI. These results from the non-linear system are well in accordance with the results obtained through the linearized system as shown in fig. 5.31.

In order to validate the result obtained in fig. 5.32, the non-linear system is simulated by adding the tuned POD individually in V_{dc} controller of GSC. The simulations are performed when the PODs are placed at all the junctions of V_{dc} controller, turn by turn, as shown in fig. 5.36. It can be observed in the figure that PODs at junction $V_{dc} - 2$ and $V_{dc} - 3$ successfully mitigate the SSCI and add significant damping to the system. PODs at junction $V_{dc} - 1$, however, damps the oscillations in the system but this process is comparatively slower as compared to

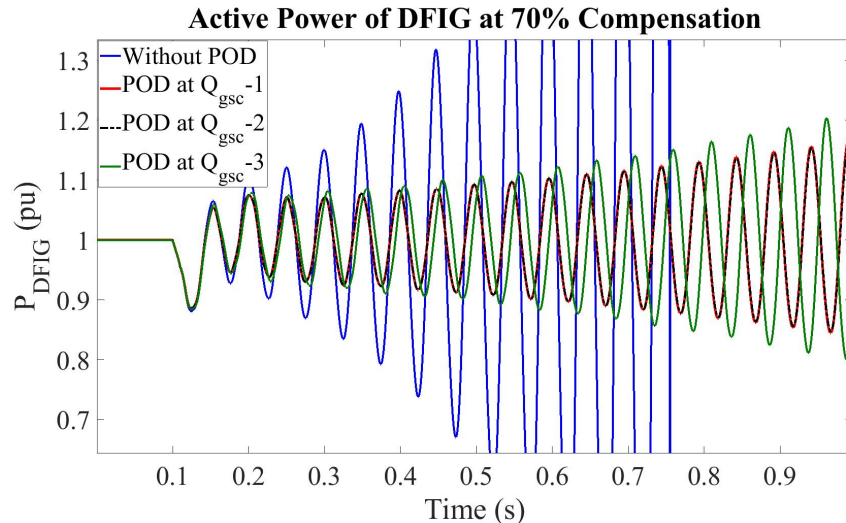


Figure 5.35: Simulation of a P_{DFIG} at 70% compensation with POD in Q_{gsc} controller.

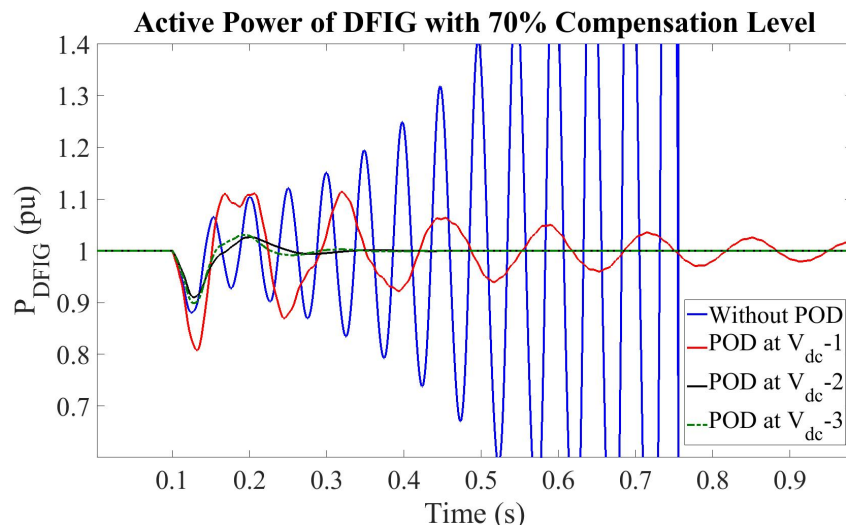


Figure 5.36: Simulation of a P_{DFIG} at 70% compensation with $u_{in} = P_{DFIG}$ in Q_{gsc} controller.

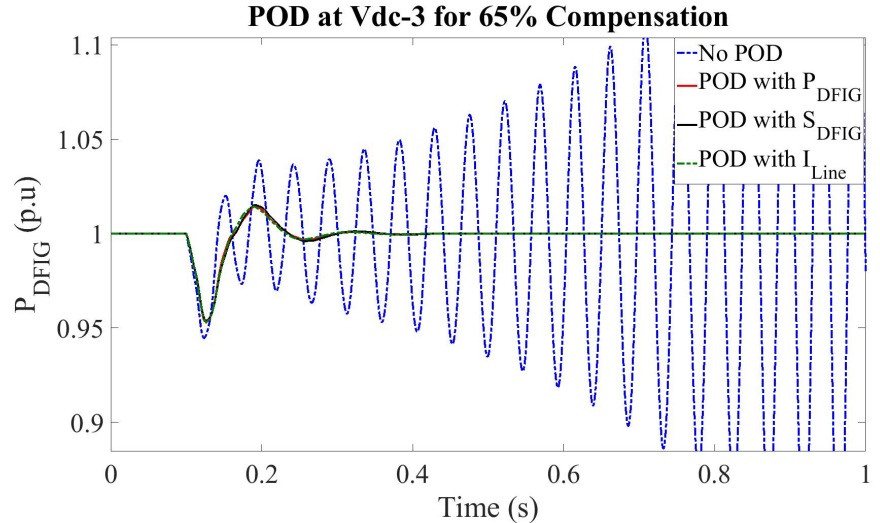


Figure 5.37: Simulation of a DFIG system at 65% series compensation.

other two cases. This response of the system is same as the one discussed while studying the residue profiles of modes of interest in Section 5.2.2.

Simulations are also performed to see the effect of POD, with other input signals, on the DFIG system for different levels of series compensation. The POD, for all the inputs, is individually added at $V_{dc} - 3$ junction. The fig. 5.37 shows the simulation of system for the POD with different inputs. It is evident from the figure that all the PODs successfully mitigate the infliction of SSCI in the system and adds high damping to it, while the system without POD proceeds towards instability.

In all the previous simulations, the system is disturbed from its equilibrium points to observe its behaviour after making a small disturbance. However, there still is a need to see the response of the system for larger disturbance. Fig. 5.38 shows the simulation of the system when larger disturbances are generated in the system by changing the series compensation levels. At first the system is stable at 40% compensation level. The compensation is increased to 50% at 0.1 s, and as a result, the oscillations are formed in the system. Although damped, these oscillation persist for much more time in the system with out POD. When the second disturbance is generated in the system by increasing the compensation level to 75%, the system without POD goes unstable. While, the system with PODs not only overcome the large disturbance, but also mitigated the oscillations. Therefore, it can be concluded that the tuned POD is capable to keep the system stable and

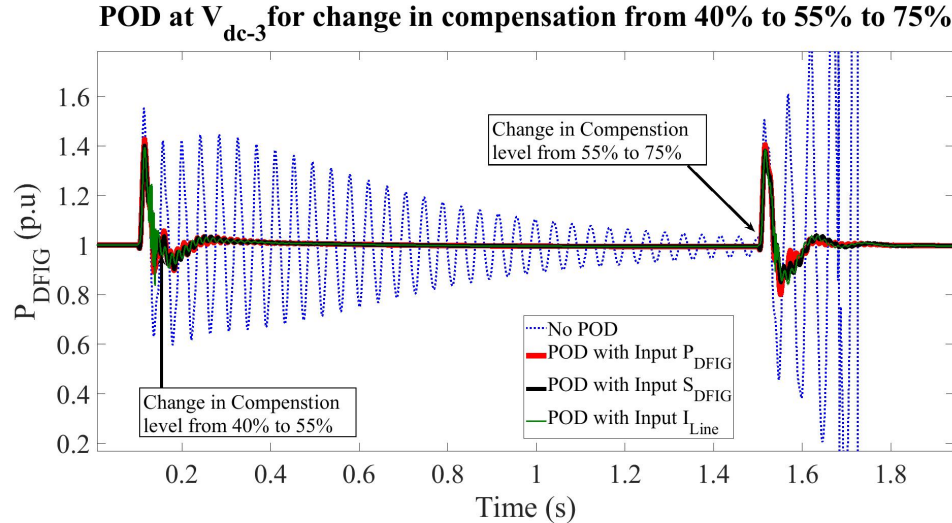


Figure 5.38: Simulation of a DFIG system at different compensation levels.

immune to SSCI even after larger disturbances in the system.

5.3 Case Studies for the Mitigation Techniques

In this section the performance of both the mitigation techniques, i.e., POD and properly tuned parameters, is demonstrated and compared for different scenarios of the designed DFIG system.

At first, a non-linear simulation is performed by changing the series compensation level in steps, as shown in fig. 5.39. It can be seen in the figure that both the mitigation techniques, when implemented individually, add significant damping in the system when the compensation level is increased to 45%, while lower damping can be seen in the normal system. Moreover, both the techniques perform well in keeping the system immune to SSCI even after the higher change in compensation level, while the system without any technique experienced the instability. The simulation result shows that both the techniques have almost same impact on the stability of the DFIG system.

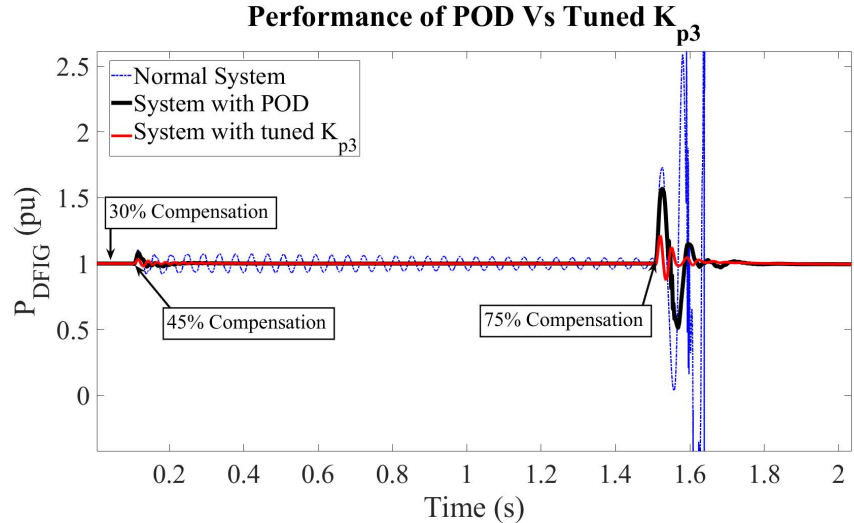


Figure 5.39: Comparison of the performance of POD with tuned K_{p3} .

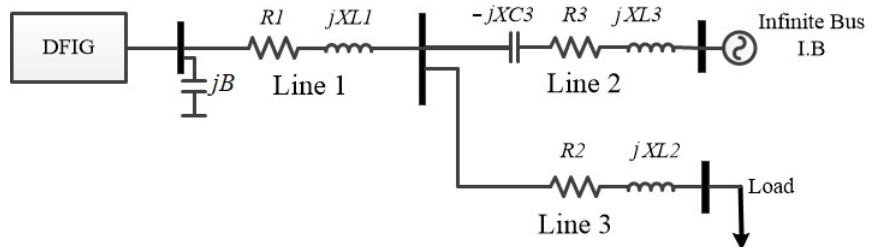


Figure 5.40: System similar to the system in ERCOT's incident.

5.3.1 Simulation of the ERCOT incident

The actual incident in ERCOT happened such that a fault in the system occurred and a transmission line was removed. The removal of the transmission line connected the wind farm radially with series compensated transmission line. Similar scenario is created by modelling the system as shown in fig.5.40. The system is simulated such that the a fault is generated on Line 3, and then the line is disconnected from the system.

Fig. 5.41 shows the response of the active power of DFIG after the fault and the disconnection of Line 3. It can be seen that when there is no mitigation technique in

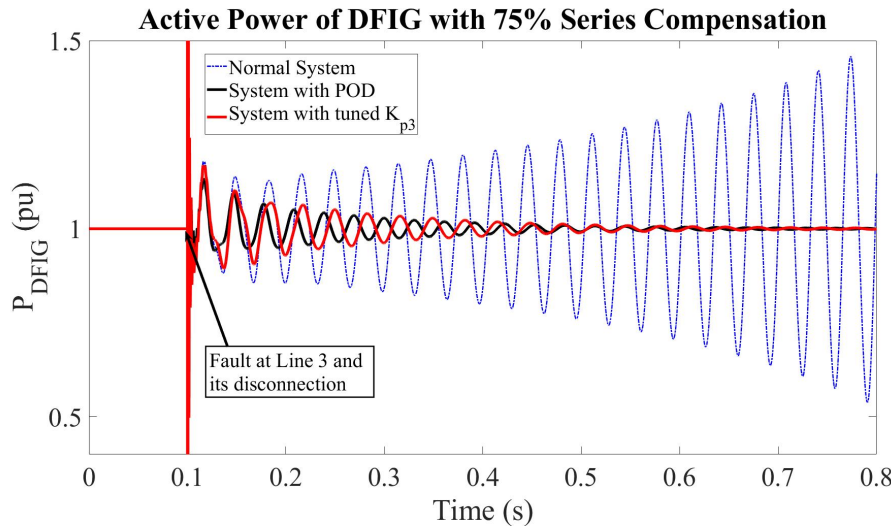


Figure 5.41: Response of the DFIG with and without mitigation techniques.

the system, the system experienced SSCI, similar to the actual incident at ERCOT. However, when the mitigation techniques are implemented in the system, SSCI is mitigated and the system stays stable.

5.3.2 Analysis of SSCI in two-area system

As another case study, a two-area system is designed, with one synchronous generator in each area, to observe the SSCI phenomenon. This system is named as System-2. The single-line diagram of the system is shown in fig. 5.42.

In this system, a 5th order model is used to design the synchronous generator, and is represented with ODE [7]. Here also, the generator is modelled in dq reference frame with q -axis leading the d -axis by 90° . The generator is designed along with a governor and automatic voltage regulator (AVR). The stator reactive power is controlled to get the reference voltage for AVR. The excitation system of the designed generator is shown in fig. 5.43. The block PSS in the figure represents the power system stabilizer (PSS). PSS will also be added in the excitation system to observe its effect on the modes of interest of the system.

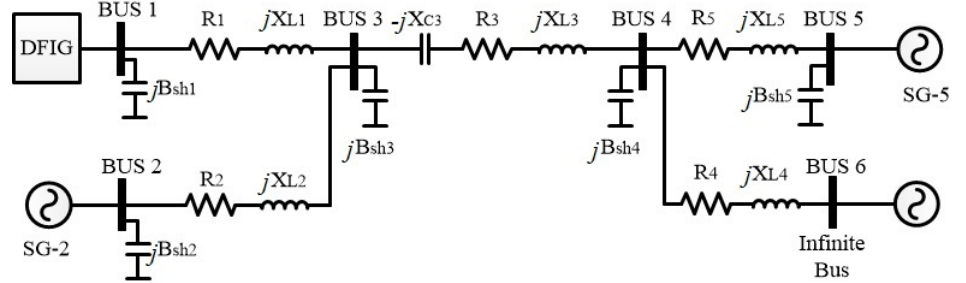


Figure 5.42: Single-line diagram of two-area system.

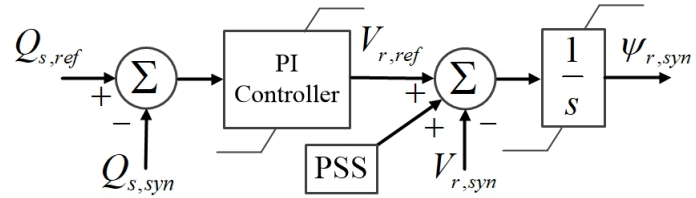


Figure 5.43: Excitation system of synchronous generator.

Eigenvalues of System-2

The two-area system is linearized and the eigenvalues of the system are computed, as done in Section 4.1. The parameters of the system are tuned such that the system remains stable below 55% series compensation level. The eigenvalues are computed while keeping the compensation level to 55%, and are given in Table 5.4.

Based on the eigenvalues of the system shown in Table 5.4, there are many modes of sub-synchronous and super-synchronous frequencies, out of which the SUB₂-2 mode has the least and negative damping ratio. It shows that SUB₂-2 mode is responsible for exposing the system to the risk of SSCI. Its frequency is 18.3 Hz which falls in the range of SSCI frequencies. There are other modes of sub-synchronous frequencies in the system, but these modes have high damping ratio and do not seem to be a threat for the stability of the system. On the other hand, out of two modes of super-synchronous frequencies, the SUP₂-2 is the one with the second least damping ratio in the system, but it is still stable at 55% compensation. It can be seen from the table that there is no mode in the system with a frequency lower than 1 Hz and having a low damping ratio, which shows that there is no risk

Table 5.4: Eigenvalues of Modes of Interest of System-2

Modes of System-2 with 55% Compensation			
Mode	Eigenvalues	Frequency (Hz)	Damping Ratio ($\zeta_{least-1}$)
SUP ₂ -1	-71.0±j409.6	65.2	0.17
SUP ₂ -2	-39.9±j336.6	53.5	0.11
SUB ₂ -1	-188±j230.4	36.6	0.63
SUB₂-2	7.54±j114.9	18.3	-0.06
SUB ₂ -3	-94.5±j37.0	5.9	0.93
SUB ₂ -4	-17.5±j29.3	4.67	0.51

Table 5.5: Participation Factors of System-2

Participation Factors of Modes of Interest of System-2	
State Variables	SUB₂-2
<i>q</i> -axis DFIG stator flux	0.15
<i>d</i> -axis DFIG rotor flux	0.17
<i>d</i> -axis sync gen 2 stator flux	0.23
Sync gen 2 rotor flux	0.24
<i>d</i> -axis transmission line current	0.17
<i>d</i> -axis series capacitor voltage	0.11
<i>q</i> -axis series capacitor voltage	0.32

for instability in the system because of inter-area oscillations. In System-2 the risk of instability is only caused by the mode of frequency 18.3 Hz, which is a typical frequency for the occurrence of SSCI.

Participation Factors of System-2

The participation factors for the least damped mode of the system, i.e., SUB₂-2, are calculated and are listed in Table 5.5 .

Based on the participation factors, it is clear that similar to the SMIB DFIG system, the DFIG stator flux, rotor flux, current through transmission line, and the voltage across series capacitor show high participation in making the SUB₂-2

mode unstable among all other state variables. However, this time the stator and rotor flux of synchronous generator also exhibit high participation towards the SSCI phenomenon. It means that the exchange of energy is not only happening between the DFIG and series capacitor, but the synchronous generator (SG-2) also takes part in this exchange. It is interesting to see such a high participation of synchronous generator in inflicting the SSCI condition, although there is no power electronic converter in its circuit. However, the state variables related to SG-5 do not show any significant participation. It shows that the synchronous generator that is connected to DFIG at the point of common coupling can add up to SSCI, while the generator in another part of the system do not participate in the phenomenon.

The high participation of synchronous generator can be explained by its effect on the equivalent impedance of the generators, as seen from the point of common coupling, Bus 3. The Thevenin impedances of both the DFIG and SG-2 branches get in parallel after short circuiting the respective equivalent voltage sources of the generators. In this case, the parallel combination of internal impedances of DFIG and SG-2, as seen from Bus 3, increases the negative effective resistance and exposes the system to the higher risk of SSCI.

Eigenvalues Analysis of System-2

The eigenvalue sensitivity analysis is performed on the linearized model of System-2 to see the effect of the most significant component of the system ,i.e. compensation level, and the effect of the most sensitive control parameter, i.e. K_{p3} , on the modes of interest. It is to observe that whether the conclusion drawn about these factors for SMIB hold true for multi-machine system or not. The influence of SG-2 on the SSCI is also studied through eigenvalue analysis.

Effect of Series Compensation Level

The effect of series compensation level on the modes of interest is observed by increasing it from 0% to 90%. The result of eigenvalue sensitivity analysis is presented in fig. 5.44. It is evident from the figure that with the increase in compensation level the SUB_2-2 mode shows significant movement towards the negative damping ratio, hence making the system unstable for higher compensation levels. The conclusion made about the effect of series compensation level for DFIG-based SMIB system also holds true for the two-area system. On the other hand, the super-synchronous modes have a very low damping ratio, but still are stable for all the

compensation levels.

Effect of K_{p3}

The proportional parameter of inner loop current controller K_{p3} of RSC is found to be the most sensitive control parameter for SSCI phenomenon. The effect of K_{p3} on the modes of interest of System-2 is studied by changing its value from 0 to 3 p.u., as shown in fig. 5.45.

The sensitivity analysis shows that, here again, K_{p3} has a significant effect on the movement of SUB_2 -2 mode, which inflicts SSCI in the system. Also, the change in K_{p3} exhibits boomerang effect in this system, and it is clear from the analysis that the value of K_{p3} should be kept high. However, here SUP_2 -1 seems to move towards the negative damping ratio, but still it remains stable until K_{p3} is 3 p.u. Therefore it is important to select the value of K_{p3} such that maximum damping can be achieved for both the least damped modes of System-2.

Effect of RSC

In Section 4.2.2 of this thesis, it is shown that the state variables corresponding to RSC do not show any significant participation towards modes of interest. However, the SSCI condition only occurs in the system when RSC is present in the DFIG circuit. In System-2, again the states variables of RSC controller do not show high participation in making the SUB_2 -2 mode unstable, as given in Table 5.5. But, in this case the synchronous generator play important role in making the system prone to SSCI. To find out whether this phenomenon is SSCI in actual or it is another type of instability caused by the presence of synchronous generator, System-2 is simulated with and with out RSC to observe its influence on modes of interest. The result of eigenvalue analysis is shown in fig. 5.46.

The compensation level of System-2 is increased and the sensitivity analysis is performed with and without RSC. It can be seen in fig. 5.46, that even without any high participation factor, the RSC is enabling the SSCI condition in the system. For the system without RSC, the SUB_2 -2 mode stays in the positive damping region for all the levels of series compensation. It can be depicted that no matter how intensely the synchronous generator is participating in making the SUB mode

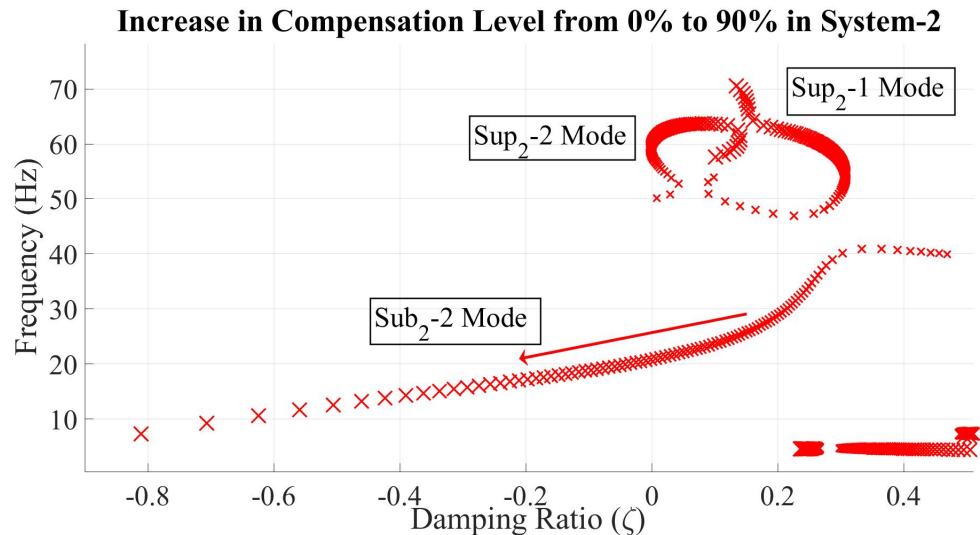
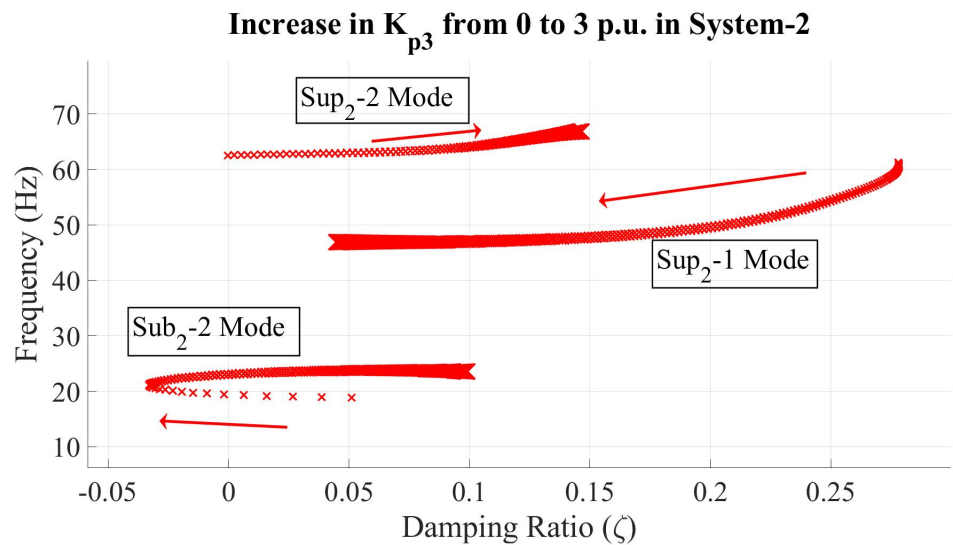


Figure 5.44: Effect of compensation level on modes of System-2.

Figure 5.45: Effect of increase in K_{p3} on modes of System-2.

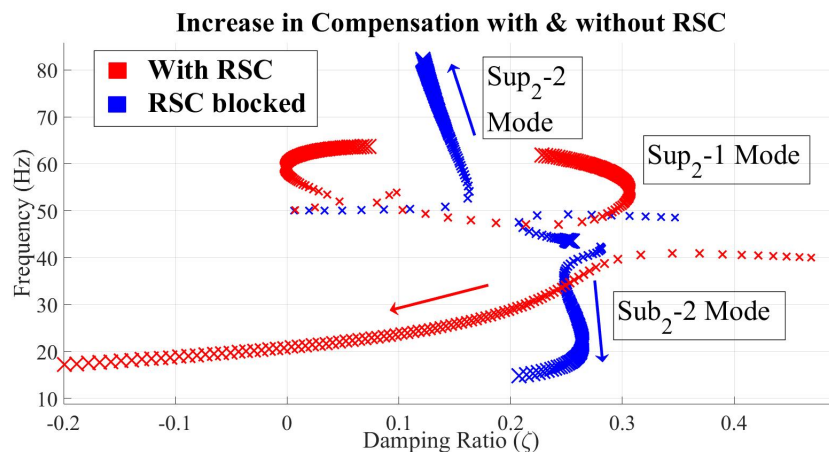


Figure 5.46: Effect of RSC and its blockage on modes of System-2.

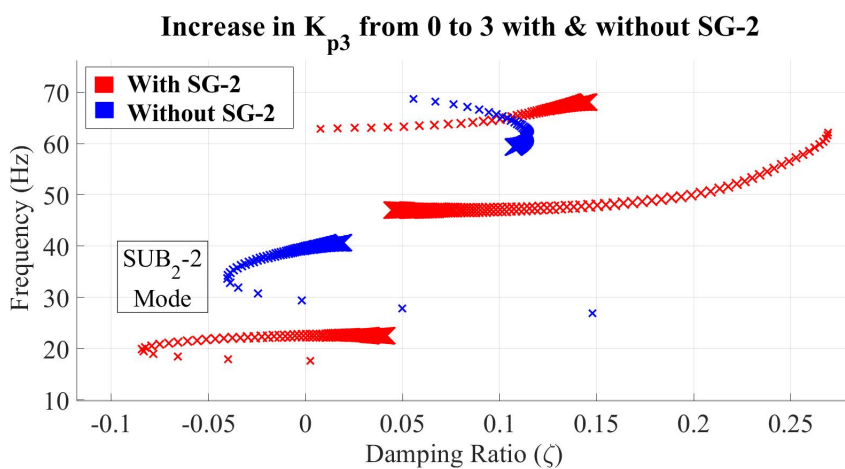


Figure 5.47: Influence of SG-2 on modes of System-2.

unstable, the presence of RSC is still mandatory for the infliction of SSCI.

Influence of SG-2

The participation factors show high influence of SG-2 stator and rotor fluxes towards SSCI. It is also discussed earlier that the presence of SG-2, in the same area as DFIG, increases the effective negative resistance of the generators as seen from the point of common coupling. To verify the negative influence of SG-2 towards SSCI, the eigenvalue analysis is performed for the system with and without SG-2, by increasing K_{p3} . The result of the analysis is shown in fig. 5.47. Although the equilibrium points of both the systems are very different, but it can be noticed that for the same compensation level, the SUB₂-2 for the system with SG-2 is pushed further towards the negative damping as compared to the system with SG-2. It means that the system with SG-2 will becomes unstable at lower compensation levels as compared to the system with out SG-2.

5.3.3 Mitigation of SSCI in System-2

To mitigate SSCI in System-2 both of the mitigation techniques, that are presented in Section 5.1 and Section 5.2, are implemented. Since there are synchronous generators in System-2, PSS is also added in their excitation systems as a third mitigation technique. Because SG-5 does not show considerable participation in the SSCI phenomenon, therefore the addition of PSS in SG-5 does not play any essential role in making the system stable. PSS is also tuned based on the residue method, similar to the tuning of POD. All the three mitigation techniques are implemented individually and their influence is observed by increasing the compensation level from 0% to 90%. It can be seen in fig. 5.48 that all the mitigation techniques remain successful in keeping the system stable to a certain level of series compensation level, higher than that of the system without any mitigation technique.

Figure 5.49 shows the eigenvalue movement of the modes of System-2 when all the mitigation techniques are implemented simultaneously. At first the sensitive parameters are tuned properly, followed by the addition of accordingly tuned POD and PSS. It can be seen from the figure that by combining all the techniques together, i.e., POD, PSS, and parameter tuning, the SSCI can be totally eliminated from System-2 for any series compensation level. The damping ration of SUB₂-2 mode in the figure remains positive for all the realistic levels of series compensa-

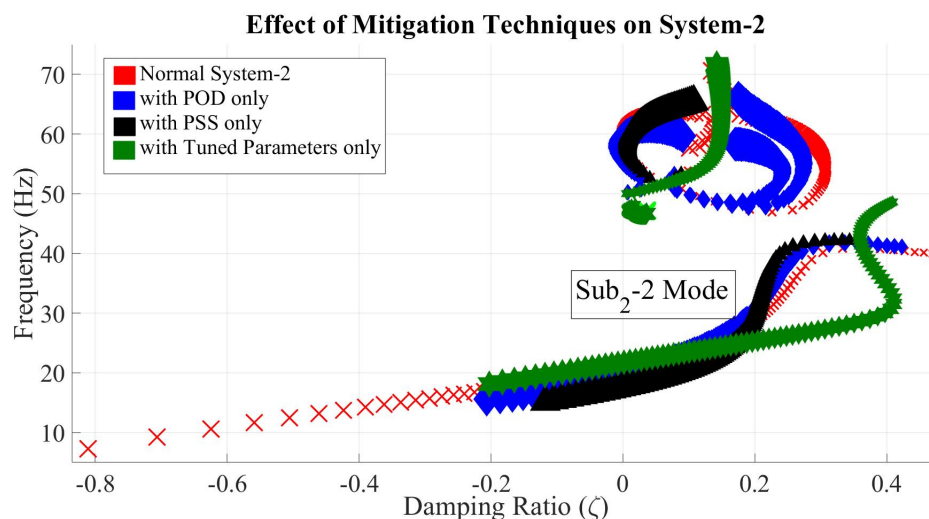


Figure 5.48: Effect of mitigation techniques on System-2.

tion.

The non-linear simulation is performed for System-2 with and without the mitigation techniques, the results of simulation for active power of DFIG is shown in fig. 5.50. It can be observed that by combining the mitigation techniques, the system not only gets immune to SSCI, but also it is very well damped. The systems with POD and PSS remain stable when the compensation level is changed to 65%, but the system with tuned parameter remains stable even when the level is increased to 85%, however the damping of system with tuned parameters is lower as compared to the system with all the mitigation techniques.

The effect of the presence of SG-2 on System-2 is also observed by simulating its disconnection from the system. The simulation result is shown in fig. 5.51. At first the compensation level of System-2, with SG-2 connected, is increased from 35% to 55%. It can be seen that with no mitigation technique, the System-2 observed the occurrence of SSCI. However, when SG-2 is disconnected from the system, the system gets back to stability and the oscillations get damped. This effect is the same as described earlier, that SG-2 is affecting the equivalent resistance of generators as seen from Bus 3, and is exposing the system to SSCI for

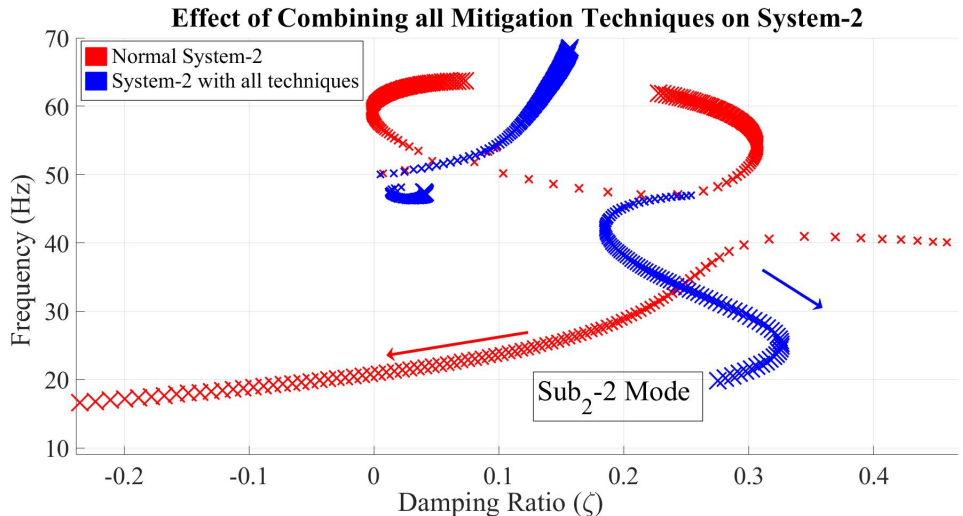


Figure 5.49: Simultaneous implementation of mitigation techniques in System-2.

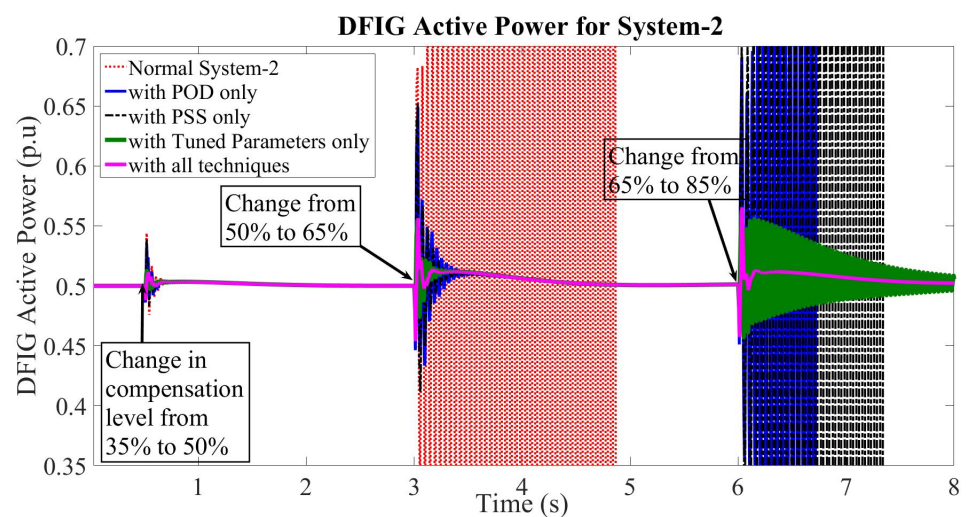


Figure 5.50: Mitigation of SSCI in DFIG active power of System-2.

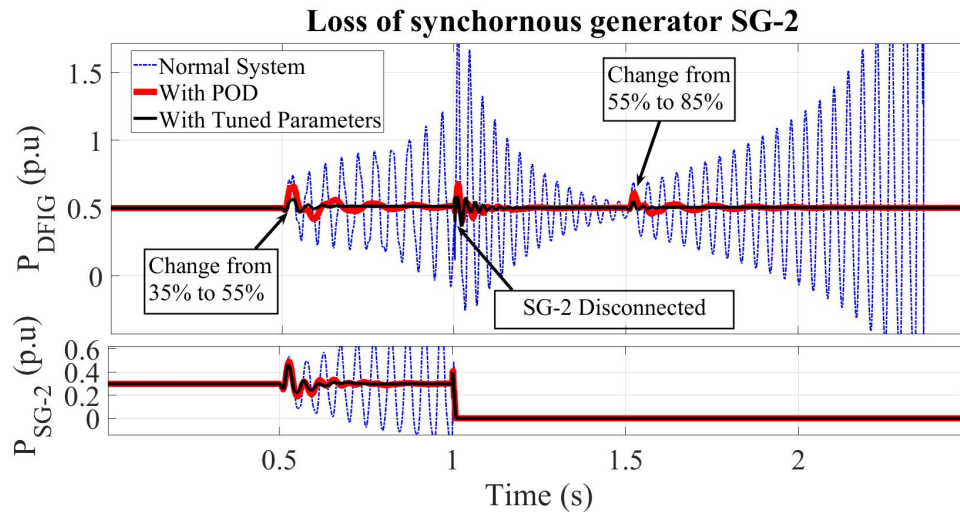


Figure 5.51: Loss of SG-2 and infliction of SSCI.

comparatively lower compensation levels. So, for System-2 without SG-2, it can remain stable even at 55% compensation level. The system experiences undamped oscillations later when the compensation level is further increased to 85%. On the other hand, when mitigation techniques are applied in System-2, individually, the system remained stable for all the simulated scenarios, ensuring its stability with and without SG-2.

Chapter 6

Conclusion and Future Work

6.1 Conclusion

The development of the modern power system is moving towards the achievement of the goals, which have been set to make the power system green and environmental friendly. The integration of renewable energy sources is increasing rapidly to limit, and eventually eliminate, the carbon emissions from the generation side of the power system. Wind power, being one of the viral sources of renewable energy, is under the limelight for this concern. The wind power is cleaner and sustainable source of energy, but along with the benefits, there are a number of challenges that are accompanied with its integration. One of the challenges faced by today's wind power system is the phenomenon of sub-synchronous control interaction (SSCI). SSCI occurs when the DFIG-based wind farms come in radial connection with the series compensated line. Both DFIG and series compensated lines are the essential parts of today's electrical grid. Therefore, there is a essential need to address this problem and to eliminate it for making the wind power reliable.

In this thesis the phenomenon of SSCI in DFIG-based power system is investigated, discussed, and mitigated. In Chapter 2, the theoretical background of different types of SSRs is discussed and it is described that SSCI is the most recent type of SSR. All the four types of wind turbines are discussed and it is desctried that only the DFIG is susceptible to SSCI. The literature review of the previous research is also given. In Chapter 3 of this thesis, a mathematical model of DFIG-based system is designed with the aim to perform the eigenvalue analysis. The ODEs are used for the modelling, and all the main component blocks of DFIG are modelled.

During the simulation of the designed system, undamped oscillations are observed in the system which show that the designed system is capable of catching the dynamics of SSCI and, hence, can be used for this study.

The derived model is then linearized in Chapter 4, and the eigenvalues corresponding to each state variable is computed. It is found that there exists a mode (SUB) in the system with the frequency in sub-synchronous range, which gets unstable for high compensation level. It shows that the instability caused in the system by high compensation level is because of SSCI. The eigenvalue sensitivity analysis is performed on the system for different factors and parameters of the system. The increase in compensation level of the transmission line is found to greatly affect the damping of SUB mode in an adverse way. For the control parameters, it is shown that the proportional parameters of the inner loop current controller of RSC (K_{p3}) affects the SUB mode the most, with the change in its value.

To understand the behaviour of the modes of interest, their participation factors are calculated and it is found that the fluxes of the generator, the current through the transmission lines, and the voltage across series capacitor play major role in generating the undamped oscillation in the system. Although the SUB mode is very sensitive to the controller parameters but the states corresponding to the VSC controllers do not show any essential participation. To explain this analytically, an impedance model of induction generator is also designed in Chapter 4. The equations for the induction generator with and without RSC inner loop controller are derived. It is shown that the presence of RSC controller makes the equivalent resistance of generator more negative, as seen from the stator terminal. It is also shown that the rotor resistance depends highly on K_{p3} when the RSC is included in the generator. Based on the influence of RSC controller and its parameters on generator's effective resistance, and based on the results obtained from the participation factors, the infliction of SSCI is explained in depth at the end of Chapter 4.

The mitigation of SSCI is discussed in Chapter 5. It is shown in Section 5.1 that the SSCI is mitigated from the system using the boomerang effect of K_{p3} . This effect of K_{p3} is further analyzed via eigenvalue analysis, and it is shown through the analysis and non-linear simulation that high value of K_{p3} can make the system immune to SSCI even of very high compensation levels. The high value of K_{p3} is also justified based on the recommendations of the previous research works. The optimum K_{p3} not only ensures the small-signal stability but it also is capable of keeping the system stable for large disturbances. The experimental validation of

SSCI phenomenon is also shown. An actual down-scaled model of 7.5 kW DFIG is used to observe the SSCI experimentally. The experimental results show that the boomerang effect of K_{p3} holds true in the actual DFIG and the optimum value of K_{p3} can mitigate SSCI experimentally.

On the other hand, in Section 5.2, it is shown that SSCI can be mitigated from DFIG-based system without any additional FACTS device. A POD is designed and added in the DFIG converter controller as a supplementary control. The parameters of the lead-lag filters of POD are tuned through residue based method, and three different local input signals are selected as the input to POD. It is shown that the POD performs the best when it is added in summation junction $V_{dc} - 3$ of GSC controller, as the connection of GSC controller to the grid and its structure is similar to that of a STATCOM. The proper tuning of POD can completely eliminate SSCI from the system, for all the compensation levels. Since all the selected inputs are local inputs, the hassle of estimating the remote signal for POD is eliminated. Different case studies are shown in Section 5.3. It is shown that the conclusions drawn from DFIG-based SMIB, in terms of analysis and mitigation, hold true even for other topologies, including the two-area system with synchronous generators. It is shown that the synchronous generator, having a same point of common coupling with DFIG, also participates in the occurrence of SSCI. And, the PSS added to the synchronous generator can also keep the system away from the risk of SSCI to a certain compensation level.

The research carried out in this thesis explains the true nature of SSCI along with the causes of its infliction. The results obtained by eigenvalue sensitivity analysis are also confirmed by the experiments on actual DFIG system. The mitigation of SSCI through control parameters tuning is proven mathematically, analytically, and experimentally. It is shown that by applying the techniques presented in this thesis, the SSCI can not only be mitigated from a simple SMIB system but can also be eliminated for larger systems with any realistic level of series compensation.

6.2 Future Work

The analysis and mitigation of SSCI in DFIG-based power system is presented and discussed in this thesis. Although many of the issues related to this topic are already addressed here, following are some of the topics which can be studied deeper to have an essential contribution towards understanding and eliminating this

problem from the DFIG system.

1. The analysis in this thesis is done on SMIB and on the system with maximum 6 buses. Therefore, it would be interesting to study the occurrence of SSCI in the system with more buses and more generators.
2. It is shown in the description of POD that the gain of POD was also affecting the residue angles of modes other than SUB mode. So, more study can be carried out for the design of filter such that only a specific mode of interest can have phase lead or lag and the other modes of system remain untouched.
3. In Section 5.1 , the main objective was to find the optimum value of K_{p3} only. The optimum values of all other parameters can be found by implementing more advance and complex optimization techniques, like particle swarm optimization or generic algorithm, to improve the performance and damping of the system along with proper mitigation of SSCI.
4. It would be interesting to form an algorithm which could take the inputs from the system, compute the optimum control parameters based on situations, and change the control parameters accordingly to improve the performance and stability of the system for different circumstances.
5. The SSCI detection algorithm presented in Section 5.1.3 can be improved and made robust to automate the gain scheduling of K_{p3} , precisely for the oscillation inflicted by SSCI.
6. The investigation of boomerang effect of K_{p3} is done using eigenvalue analysis. More study could be carried out to understand this effect by using analytical methods in frequency domain.
7. Due to certain constraints only the parameter tuning mitigation technique is validated experimentally. It would be an interesting extension to this research if the mitigation technique based on POD could be validated experimentally based on local input signals.

Appendix

Table 6.1: Parameters of DFIG system

Parameters	Values
DFIG rated power P_n [kW]	7.5
Phase peak voltage U_{sn} [V]	311
Stator resistance R_s [mΩ]	440
Rotor resistance R_r [m Ω]	640
Magnetizing inductance L_m [mH]	79.3
Stator leakage inductance L_{sl} [mH]	5.43
Rotor leakage inductance L_{rl} [mH]	6.51
Power converters rated power [kW]	5
DC-link voltage v_{dc} [V]	650
Line resistance R_L [Ω]	1
Line inductance L_L [mH]	5.5 – 13.5
Series compensation capacitance [μ F]	2000

Table 6.2: Parameters of the Controllers in p.u.

K_{p1}	0.1		K_{p4}	50
K_{i1}	20		K_{i4}	200
K_{p2}	0.01		K_{p5}	10
K_{i2}	50		K_{i5}	100
K_{p3}	4		K_{p6}	0.5
K_{i3}	30		K_{i6}	90

Table 6.3: Parameters of DFIG System Used in POD Analysis

Parameters	Values
Stator resistance R_s [p.u]	0.05
Rotor resistance R_r [p.u]	0.02
Magnetizing inductance L_m [p.u]	5
Leakage inductances L_{sl}, L_{rl} [p.u]	0.1
Inertia constant H [s]	4.5
DC link capacitor C_{dc} [p.u]	0.1
Transformer reactance X_{tgsc} [p.u]	0.06
Shunt susceptance B_{sh} [p.u]	0.1
Line resistance R_L [p.u]	0.02
Line reactance X_L [p.u]	0.5

Table 6.4: Parameters of the Controllers Used in POD Analysis in p.u.

K_{p1}	0.5		K_{p4}	5
K_{i1}	15		K_{i4}	250
K_{p2}	8		K_{p5}	10
K_{i2}	20		K_{i5}	100
K_{p3}	2		K_{p6}	0.5
K_{i3}	8		K_{i6}	100
K_{p31}	0.025		K_{p61}	1
K_{i31}	1		K_{i61}	100

Bibliography

- [1] A. D. Sahin, "Progress and recent trends in wind energy," *Int. J. Progress in Energy Combustion Sci.*, vol. 30, no. 5, pp. 501–543, 2004
- [2] GWEC. (Feb. 2017). *Global Wind Statistics 2016*. [Online]. Available: www.gwec.net
- [3] F. Blaabjerg, and K. Ma, 'Wind Energy Systems', *Proceedings of the IEEE*, vol. 105, no. 11, Nov. 2017
- [4] T. Agarwal, S. Verma and A. Gaurh, "Issues and challenges of wind energy," *2016 International Conference on Electrical, Electronics, and Optimization Techniques (ICEEOT)*, Chennai, 2016, pp. 67–72.
- [5] H. T. Nguyen, G. Yang, A. H. Nielsen and P. H. Jensen, "Frequency stability enhancement for low inertia systems using synthetic inertia of wind power," *2017 IEEE Power & Energy Society General Meeting*, Chicago, IL, 2017, pp. 1–5.
- [6] O. Ojo, "Optimal series capacitor compensation of high voltage transmission lines," *The Twenty-Third Southeastern Symposium on System Theory*, Columbia, SC, USA, 1991, pp. 550–554.
- [7] P. M. Anderson, B. L. Agrawal, and J. E. Van Ness. *Subsynchronous resonance in power systems*. vol. 9. John Wiley and Sons, 1999.
- [8] G. D. Irwin, A. K. Jindal and A. L. Isaacs, "Sub-synchronous control interactions between type 3 wind turbines and series compensated AC transmission systems," *2011 IEEE Power and Energy Society General Meeting*, San Diego, CA, 2011, pp. 1–6.

- [9] H. T. Ma, P. B. Brogan, K. H. Jensen and R. J. Nelson, "Sub-Synchronous Control Interaction studies between full-converter wind turbines and series-compensated AC transmission lines," *2012 IEEE Power and Energy Society General Meeting*, San Diego, CA, 2012, pp. 1–5.
- [10] J. Adams, C. Carter and, S. Huang, "ERCOT experience with subsynchronous control interaction and proposed remediation," *PES T & D 2012*, Orlando, FL, 2012, pp. 1–5.
- [11] X. Xie, X. Zhang, H. Liu, H. Liu, Y. Li, and C. Zhang, "Characteristic analysis of subsynchronous resonance in practical wind farms connected to series-compensated transmissions," *IEEE Transactions on Energy Conversion*, vol. 32, no. 3, pp. 1117–1126, Sep. 2017.
- [12] R. Nath and C. Grande-Moran, "Study of Sub-Synchronous Control Interaction due to the interconnection of wind farms to a series compensated transmission system," *PES T& D 2012*, Orlando, FL, 2012, pp. 1–6.
- [13] New.abb.com. (2017). Fixed series compensation | ABB. [online] Available at: <http://new.abb.com/facts/fixed-series-compensation>
- [14] "Terms, Definitions and Symbols for Subsynchronous Oscillations," *IEEE Transactions on Power Apparatus and Systems*, vol. PAS-104, no. 6, pp. 1326–1334, June 1985.
- [15] IEEE SSR Working Group. "Proposed terms and definitions for subsynchronous resonance." *IEEE symposium on countermeasures for subsynchronous resonance*, IEEE Pub. 81TH0086-9-PWR. 1981.
- [16] "Reader's guide to subsynchronous resonance," *IEEE Transactions on Power Systems*, vol. 7, no. 1, pp. 150–157, Feb 1992.
- [17] M. C. Hall and D. A. Hodges, "Experience with 500-kV Subsynchronous Resonance and Resulting Turbine Generator Shaft Damage at Mohave Generating Station," *IEEE PES Special Publication, Analysis and Control of Subsynchronous Resonance*, IEEE Publication, vol. 76, pp.22–29, 1976.
- [18] G. Andersson, R. Atmuri, R. Rosenqvist and S. Torseng, "Influence of Hydro Units' Generator-to-Turbine Inertia Ratio on Damping of Subsynchronous Oscillations," *IEEE Transactions on Power Apparatus and Systems*, vol. PAS-103, no. 8, pp. 2352-2361, Aug. 1984.

- [19] L. Harnefors, M. Bongiorno and S. Lundberg, "Input-Admittance Calculation and Shaping for Controlled Voltage-Source Converters," *IEEE Transactions on Industrial Electronics*, vol. 54, no. 6, pp. 3323–3334, Dec. 2007.
- [20] P. Anderson and R. Farmer, *Series Compensation of Power System*. United States of America: PBLSH, 1991.
- [21] K. Narendra et al., "New microprocessor based relay to monitor and protect power systems against sub-harmonics," *2011 IEEE Electrical Power and Energy Conference*, Winnipeg, MB, 2011, pp. 438–443.
- [22] L. Wang, X. Xie, Q. Jiang, H. Liu, Y. Li and H. Liu, "Investigation of SSR in Practical DFIG-Based Wind Farms Connected to a Series-Compensated Power System," *IEEE Transactions on Power Systems*, vol. 30, no. 5, pp. 2772–2779, Sept. 2015.
- [23] F. Bizzarri, A. Brambilla and F. Milano, "Simplified Model to Study the Induction Generator Effect of the Subsynchronous Resonance Phenomenon," in *IEEE Transactions on Energy Conversion*, vol. 33, no. 2, pp. 889–892, June 2018.
- [24] L. Fan, R. Kavasseri, Z. L. Miao and C. Zhu, "Modeling of DFIG-Based Wind Farms for SSR Analysis," in *IEEE Transactions on Power Delivery*, vol. 25, no. 4, pp. 2073–2082, Oct. 2010.
- [25] X. Zhu and Z. Pan, "Study on the influencing factors and mechanism of SSR due to DFIG-based wind turbines to a series compensated transmission system," *2017 IEEE 26th International Symposium on Industrial Electronics (ISIE)*, Edinburgh, 2017, pp. 1029–1034.
- [26] T. Ackermann, *Wind Power in Power Systems*, Wiley, 2005.
- [27] A. Tabesh and R. Iravani, "Small-Signal Dynamic Model and Analysis of a Fixed-Speed Wind Farm - A Frequency Response Approach," *IEEE Trans. On Power Deliver*, vol. 21, no. 2, Apr. 2006, pp. 778–787.
- [28] M. S. El-Moursi, B. Bak-Jensen, M. H. Abdel-Rahman, "Novel STATCOM Controller for Mitigating SSR and Damping Power System Oscillations in a Series Compensated Wind Park," *IEEE Transactions on Power Electronics*, vol. 25, no. 2, pp. 429–441, Feb. 2010.

- [29] J. Zhang, X. Xiao, P. Zhang, J. Lu, and T. Orekan, "Sub-synchronous Control Interaction Analysis and Trigger-based Damping Control for Doubly Fed Induction Generator-based Wind Turbines," *Electric Power Components and Systems*, vol. 44, no. 7, pp. 713–725, Apr. 2016.
- [30] T. Burton, D. Sharpe, N. Jenkins, and E. Bossanyi, *Wind Energy Handbook*, Chichester: John Wiley & Sons, 2001.
- [31] Gao Feng, He Qifei, Hao Zhiguo and Zhang Baohui, "The research of sub synchronous oscillation in PMSG wind farm," *2016 IEEE PES Asia-Pacific Power and Energy Engineering Conference (APPEEC)*, Xi'an, 2016, pp. 1883–1887.
- [32] Y. Liu, L. Wang, H. Sun and B. Huang, "Characteristics of sub-synchronous interaction among D-PMSG-based wind turbines," in *The Journal of Engineering*, vol. 3, no. 16, pp. 1434–1438, 2019.
- [33] Z. Xiaoyu, L. Chao and W. Zhibing, "Analysis and control on Sub-synchronous oscillation(SSO) of HVDC transmission for large-scale permanent magnet synchronous generators(PMSG)-based wind farm integration," in *The Journal of Engineering*, vol. 3, no. 16, pp. 2440–2444, 2019.
- [34] B. Badrzadeh, M. Sahni, Y. Zhou, D. Muthumuni, and A. Gole, "General methodology for analysis of sub-synchronous interaction in wind power plants." *IEEE Transactions on Power Systems* 28, no. 2 (2013): 1858–1869.
- [35] M. Bongiorno, A. Petersson, and E. Agneholm. "The impact of wind farms on subsynchronous resonance in power systems." *Elforsk Report* 11 (2011): 29.
- [36] D. H. Suriyaarachchi, U. Annakkage, C. Karawita and D. Jacobson, "A procedure to study sub-synchronous interactions in wind integrated power systems," *2013 IEEE Power & Energy Society General Meeting*, Vancouver, BC, 2013, pp. 1–1.
- [37] L. Fan, R. Kavasseri, Z. L. Miao, and C. Zhu, "Modeling of DFIG based wind farms for SSR analysis," *IEEE Trans. Power Del.*, vol. 25, no. 4, pp. 2073–2082, Oct. 2010.
- [38] L. Fan, C. Zhu, Z. Miao, and M. Hu, "Modal analysis of DFIG-based wind farm interfaced with a series compensated network," *IEEE Trans. Energy Convers.* , vol. 26, no. 4, pp. 1010–1020, Dec. 2011.

- [39] H. A. Mohammadpour and E. Santi, "Sub-synchronous resonance analysis in DFIG-based wind farms: Definitions and problem identification - Part I," *2014 IEEE Energy Conversion Congress and Exposition (ECCE)*, Pittsburgh, PA, 2014, pp. 812–819.
- [40] F. Mei and B. C. Pal, "Modelling and small-signal analysis of a grid connected doubly-fed induction generator," *IEEE Power Engineering Society General Meeting, 2005*, 2005, pp. 2101–2108 Vol. 3.
- [41] H.A. Mohammadpour and E. Santi, "SSR damping controller design and optimal placement in rotor-side and grid-side converters of series-compensated DFIG-based wind farm," *IEEE Transactions on Sustainable Energy*, vol. 6, no. 2, pp. 388–399, Apr. 2015.
- [42] M. Ghafouri, U. Karaagac, H. Karimi, S. Jensen, J. Mahseredjian and S. O. Faried, "An LQR Controller for Damping of Subsynchronous Interaction in DFIG-Based Wind Farms," in *IEEE Transactions on Power Systems*, vol. 32, no. 6, pp. 4934-4942, Nov. 2017.
- [43] P. Huang, M. S. El Moursi, W. Xiao and J. L. Kirtley, "Subsynchronous Resonance Mitigation for Series-Compensated DFIG-Based Wind Farm by Using Two-Degree-of-Freedom Control Strategy," in *IEEE Transactions on Power Systems*, vol. 30, no. 3, pp. 1442–1454, May 2015.
- [44] J. Taherahmadi, M. Jafarian and M. Asefi, "Using adaptive control in DFIG-based wind turbines to improve the subsynchronous oscillations of nearby synchronous generators," in *IET Renewable Power Generation*, vol. 11, no. 2, pp. 362–369, 8 2 2017.
- [45] A. E. Leon, "Integration of DFIG-Based Wind Farms Into Series-Compensated Transmission Systems," in *IEEE Transactions on Sustainable Energy*, vol. 7, no. 2, pp. 451–460, April 2016.
- [46] L. Wang, X. Xie, Q. Jiang and X. Liu, "Centralised solution for sub-synchronous control interaction of doubly fed induction generators using voltage-sourced converter," in *IET Generation, Transmission & Distribution*, vol. 9, no. 16, pp. 2751–2759, 3 12 2015.
- [47] H. A. Mohammadpour and E. Santi, "Analysis of subsynchronous control interactions in DFIG-based wind farms: ERCOT case study," *2015 IEEE En-*

- ergy Conversion Congress and Exposition (ECCE)*, Montreal, QC, 2015, pp. 500–505.
- [48] H. A. Mohammadpour and E. Santi, "Optimal adaptive sub-synchronous resonance damping controller for a series-compensated doubly-fed induction generator-based wind farm," in *IET Renewable Power Generation*, vol. 9, no. 6, pp. 669–681, 8 2015.
 - [49] X. Wu, Y. Guan and W. Ning, "Reactive power control strategy of DFIG-based wind farm to mitigate SSO," in *The Journal of Engineering*, vol. 2017, no. 13, pp. 1290–1294, 2017.
 - [50] L. Fan and Z. Miao, "Nyquist-Stability-Criterion-Based SSR Explanation for Type-3 Wind Generators," in *IEEE Transactions on Energy Conversion*, vol. 27, no. 3, pp. 807–809, Sept. 2012.
 - [51] H. Liu, X. Xie, Y. Li, H. Liu and Y. Hu, "A small-signal impedance method for analyzing the SSR of series-compensated DFIG-based wind farms," *2015 IEEE Power & Energy Society General Meeting*, Denver, CO, 2015, pp. 1–5.
 - [52] Z. Miao, "Impedance-Model-Based SSR Analysis for Type 3 Wind Generator and Series-Compensated Network," in *IEEE Transactions on Energy Conversion*, vol. 27, no. 4, pp. 984–991, Dec. 2012.
 - [53] J. Daniel, W. Wong, G. Ingeström and J. Sjöberg, "Subsynchronous phenomena and wind turbine generators," *PES T & D 2012*, Orlando, FL, 2012, pp. 1–6.
 - [54] S. Chernet and M. Bongiorno, "Input impedance based nyquist stability criterion for subsynchronous resonance analysis in DFIG based wind farms," *2015 IEEE Energy Conversion Congress and Exposition (ECCE)*, Montreal, QC, 2015, pp. 6285–6292.
 - [55] A. E. Leon and J. A. Solsona, "Sub-Synchronous Interaction Damping Control for DFIG Wind Turbines," *IEEE Transactions on Power Systems*, vol. 30, no. 1, pp. 419–428, Jan. 2015.
 - [56] Y. Song and F. Blaabjerg, "Overview of DFIG-Based Wind Power System Resonances Under Weak Networks," *IEEE Transactions on Power Electronics*, vol. 32, no. 6, pp. 4370–4394, Jun. 2017.

- [57] H. Liu, X. Xie, C. Zhang, Y. Li, H. Liu and Y. Hu, "Quantitative SSR Analysis of Series-Compensated DFIG-Based Wind Farms Using Aggregated RLC Circuit Model," *IEEE Transactions on Power Systems*, vol. 32, no. 1, pp. 474–483, Jan. 2017.
- [58] M. Rahimi and M. Parniani, "Transient Performance Improvement of Wind Turbines With Doubly Fed Induction Generators Using Nonlinear Control Strategy," *IEEE Transactions on Energy Conversion*, vol. 25, no. 2, pp. 514–525, June 2010.
- [59] A. Ostadi, A. Yazdani and R. K. Varma, "Modeling and Stability Analysis of a DFIG-Based Wind-Power Generator Interfaced With a Series-Compensated Line," *IEEE Transactions on Power Delivery*, vol. 24, no. 3, pp. 1504–1514, July 2009.
- [60] M.S. El-Moursi, "Mitigating subsynchronous resonance and damping power system oscillation in a series compensated wind park using a novel static synchronous series compensator control algorithm," *Wind Energy*, vol. 15, no. 3, pp. 363–377, Apr. 2012
- [61] L. Fan and Z. Miao, "Mitigating SSR using DFIG-based wind generation," *IEEE Transactions on Sustainable Energy*, vol. 3, no. 3, pp. 349–358, Jul. 2012.
- [62] U. Karaagac, S. O. Faried, J. Mahseredjian and A. Edris, "Coordinated Control of Wind Energy Conversion Systems for Mitigating Subsynchronous Interaction in DFIG-Based Wind Farms," in *IEEE Transactions on Smart Grid*, vol. 5, no. 5, pp. 2440–2449, Sept. 2014.
- [63] H. A. Mohammadpour, A. Ghaderi, H. Mohammadpour, and E. Santi, "SSR damping in wind farms using observed-state feedback control of DFIG converters," *Elect. Power Syst. Res.*, vol. 123, pp. 57–66, 2015
- [64] S. Shao, E. Abdi, F. Barati and R. McMahon, "Stator-Flux-Oriented Vector Control for Brushless Doubly Fed Induction Generator," in *IEEE Transactions on Industrial Electronics*, vol. 56, no. 10, pp. 4220-4228, Oct. 2009.
- [65] P. C. Kundur, N. J. Balu, and M. G. Lauby. *Power System Stability and Control*. McGraw-Hill Professional, 1994.

- [66] R. Pena, J. C. Clare, and G. M. Asher, "Doubly fed induction generator using back-to-back PWM converters and its application to variable speed wind-energy generation", *IEE Proc.-Electr. Power Appl.*, vol. 143, no. 3, pp. 231–241, May 1996.
- [67] R. Datta and V. T. Ranganathan, "Decoupled control of active and reactive power for a grid-connected doubly-fed wound rotor induction machine without position sensors," *Conference Record of the 1999 IEEE Industry Applications Conference. Thirty-Forth IAS Annual Meeting* (Cat. No.99CH36370), Phoenix, AZ, USA, 1999, pp. 2623-2630 vol.4.
- [68] L. Fan and Z. Miao, Modeling and Analysis of Doubly Fed Induction generator Wind Energy Systems. Orlando, FL, USA: Academic, Apr. 2015.
- [69] Manitoba HVDC Research centre, *PSCAD X4 Online Help*, May 2011.
- [70] G. C. Verghese, I. J. Perez-arriaga and F. C. Schweppe, "Selective Modal Analysis With Applications to Electric Power Systems, Part II: The Dynamic Stability Problem," in *IEEE Transactions on Power Apparatus and Systems*, vol. PAS-101, no. 9, pp. 3126-3134, Sept. 1982.
- [71] IEEE Committee Rep., "Reader's guide to sub-synchronous resonance," *IEEE Transaction on Power Systems*, Vol. 7, No. 1, pp. 150–157, Feb.1992.
- [72] Selam Chernet, "Subsynchronous resonance in Doubly-fed induction generator based wind farms", Licentiate thesis, 2016.
- [73] G. R. Semon, "Modelling of induction machines for electric drives," in *IEEE Transactions on Industry Applications*, vol. 25, no. 6, pp. 1126-1131, Nov.-Dec. 1989.
- [74] A. Petersson, "Analysis, Modeling and Control of Doubly-Fed Induction Generators for Wind Turbines," Chalmers University of Technology, Gothenburg, Sweden, Licentiate Thesis, 2003.
- [75] L. Harnefors, and H. P. Nee, "Model-based Current Control of AC Machines using Internal Model Control Method," *IEEE Transaction on Industrial Application*, vol. 34, no. 1, pp. 133–141, 1998.
- [76] G. Rogers, *Power System Oscillations*. Norwell, MA: Kluwer, Dec. 1999.

- [77] F. L. Pagola, I. J. Perez-Arriaga and G. C. Verghese, "On sensitivities, residues and participations: applications to oscillatory stability analysis and control," *IEEE Transactions on Power Systems*, vol. 4, no. 1, pp. 278-285, Feb 1989.
- [78] N. Martins, L. T. G. Lima, "Eigenvalue and Frequency Domain Analysis of Small Signal Electromechanical Stability Problems," *Eigenvalue analysis and Frequency Domain Methods for System Dynamic Performance*, IEEE, New York, 1989.
- [79] C. Zhu, M. Hu and Z. Wu, "Parameters impact on the performance of a double-fed induction generator-based wind turbine for subsynchronous resonance control," in *IET Renewable Power Generation*, vol. 6, no. 2, pp. 92–98, March 2012.
- [80] Selam Chernet, "Subsynchronous resonance in Doubly-fed induction generator based wind farms", Doctoral thesis, 2018.
- [81] L. Harnefors, M. Hinkkanen, and O. Wallmark, "Control of Voltage-Source Converters and Variable-Speed Drives", Compendium.